The PMC Turbo Experiment: Design, Development, and Results

Carl Björn Kjellstrand

Submitted in partial fulfillment of the
requirements for the degree of
Doctor of Philosophy
under the Executive Committee
of the Graduate School of Arts and Sciences

COLUMBIA UNIVERSITY

2021

Abstract

The PMC Turbo Experiment: Design, Development, and Results

Carl Björn Kjellstrand

In the middle and upper atmosphere, dynamics of scales from tens of meters to thousands of kilometers primary arise due to the influence of gravity waves propagating from lower altitudes. In order to understand the structure and variability of these regions of our planet's atmosphere, we must understand the propagation, influences, and dissipation of gravity waves. However, gravity waves and their influences are difficult to measure. Their largest and most observable effects occur in the remote mesosphere and lower thermosphere and the relevant spatial scales extend across many orders of magnitude.

The EBEX group discovered a novel method to observe polar mesospheric clouds, which are a sensitive tracer of gravity waves and their associated dynamics. This discovery motivated the Polar Mesospheric Cloud Turbulence (PMC Turbo) experiment. Polar mesospheric clouds form an extremely thin but bright layer at roughly 80 kilometer altitude in which we can observe brightness fluctuations created by gravity wave dynamics and the resulting instabilities. PMC Turbo included seven pressure vessels, each of which contained an optical camera, hard drives, and computers that controlled the image capture, flight control, and communication with ground stations. The cameras captured spatial scales from gravity waves with wavelengths of roughly 10-100 kilometers, instability dynamics at scales from about 1-10 kilometers, and the fine structure at the inner scale of turbulence down to 20 meters. PMC Turbo flew at 38 kilometer altitude and remained afloat for nearly six days. During this time, it travelled from Esrange Space

Center in Sweden to the Northwest Passage in Canada. Complementary data from other instruments provides additional atmospheric context to the PMC Turbo measurements.

During flight, the PMC Turbo cameras captured images of polar mesospheric clouds tracing Kelvin-Helmholtz instabilities with a high signal-to-noise ratio. Kelvin-Helmholtz instabilities play major roles in energy dissipation and structure of geophysical fluids, and they have a close relationship with gravity waves. The PMC Turbo images include complicated interactions and secondary instabilities leading to turbulence. These dynamics provide insight into the atmospheric conditions and rate of energy dissipation in the mesosphere and lower thermosphere.

Table of Contents

Chapter 1: Background

1.1 Gravity Wave Overview

Waves within a fluid in which gravity provides a restoring force are called gravity waves (GWs). GWs arising from diverse sources are prevalent throughout geophysical fluids and they play important roles in the structure of our atmosphere and oceans. The research described in this thesis examines one aspect of the roles of GWs in the dynamics and structure of the upper atmosphere, particularly the Mesosphere and Lower Thermosphere (MLT). Several categories of GW influence the MLT. Orographic GWs are generated by winds encountering terrain. Nonorographic GWs are generated through weather events. These include convective GWs generated by convective heating and frontal GWs generated by strong wind fields and temperature gradients. Jet streams and secondary GW generation are also major sources.

In the MLT, atmospheric GWs can be described approximately by linear theory as adiabatically displaced parcels of air in a stably stratified background, with a restoring force described by buoyancy. Appendix A.1 shows a derivation of this idealized wave motion. In reality, the terrain and weather that generate GWs result in a wide spectrum of frequencies, wavelengths, and propagation directions. Generally, wavelengths spam around 10 km to 2000 km. This chapter will cover the basics of gravity wave dynamics especially relevant to the research described in this thesis. For a detailed overview of GW dynamics, generation, characteristics, and atmospheric influences, refer to Fritts and Alexander's 2003 article [22].

Planetary atmospheres host a wide variety of dynamics from planetary to sub-meter scales. Instabilities and turbulence also play fundamental roles in the circulation, structure, and variability of the atmosphere from the surface into the MLT because they account for the deposition of energy and momentum transported by GWs from lower atmospheric sources. GWs in particular play key roles in defining the Earth's weather and climate. While this thesis touches on the role of GWs in the atmosphere, GWs also play an important role in many geophysical fluids such as bodies of water [82] [90] [92]. Figure 1.1 shows GWs in polar stratospheric clouds in panel a and one example of instabilities strongly associated with GWs in panel b.

The planetary boundary layer is the lowest layer of our atmosphere where the surface of our planet directly influences atmospheric dynamics. Above the boundary layer, atmospheric dynamics on scales between tens of meters to a few thousand kilometers largely arise in response to GWs, while tides and planetary waves dictate larger-scale features. GWs contribute the major vertical and horizontal transports of energy and momentum from tropospheric sources to higher altitudes and account for their deposition via GWs dissipation, breaking, and overturning [22]. This is due to the increase in GW amplitudes with decreasing density. With increasing GW amplitudes comes an increasing tendency for instabilities leading to dissipation and deposition of momentum and energy. In order to understand the macroscopic energy and momentum budgets of the middle atmosphere, we need to understand GW transport, and in order to understand GW transport we need to understand the mechanisms of this transport i.e. instabilities since the large scale dynamics of GW breaking and GW momentum and energy transport depend on the small scale dynamics.

1.2 The role of gravity waves in general circulation models

The atmospheric physics and chemistry communities employ comprehensive models of the Earth's atmosphere called general circulation models (GCMs) or global climate models to understand and predict the behavior of Earth's atmosphere. As these models have improved to better represent our atmosphere, they have also become more complex due to coupling between the atmosphere across the globe and between vertical layers. While GCMs continue to reveal the importance of GWs to the macroscopic behavior of the atmosphere, they cannot resolve small-scale GWs, nor their smaller-scale dissipation dynamics. Instead, such models account for momentum transport via parameterization. While parameterization is a valuable tool to reduce the computational expense of running models, we can improve the parameterization through better understand-

(a) Gravity waves in polar stratospheric clouds (1-20 km)

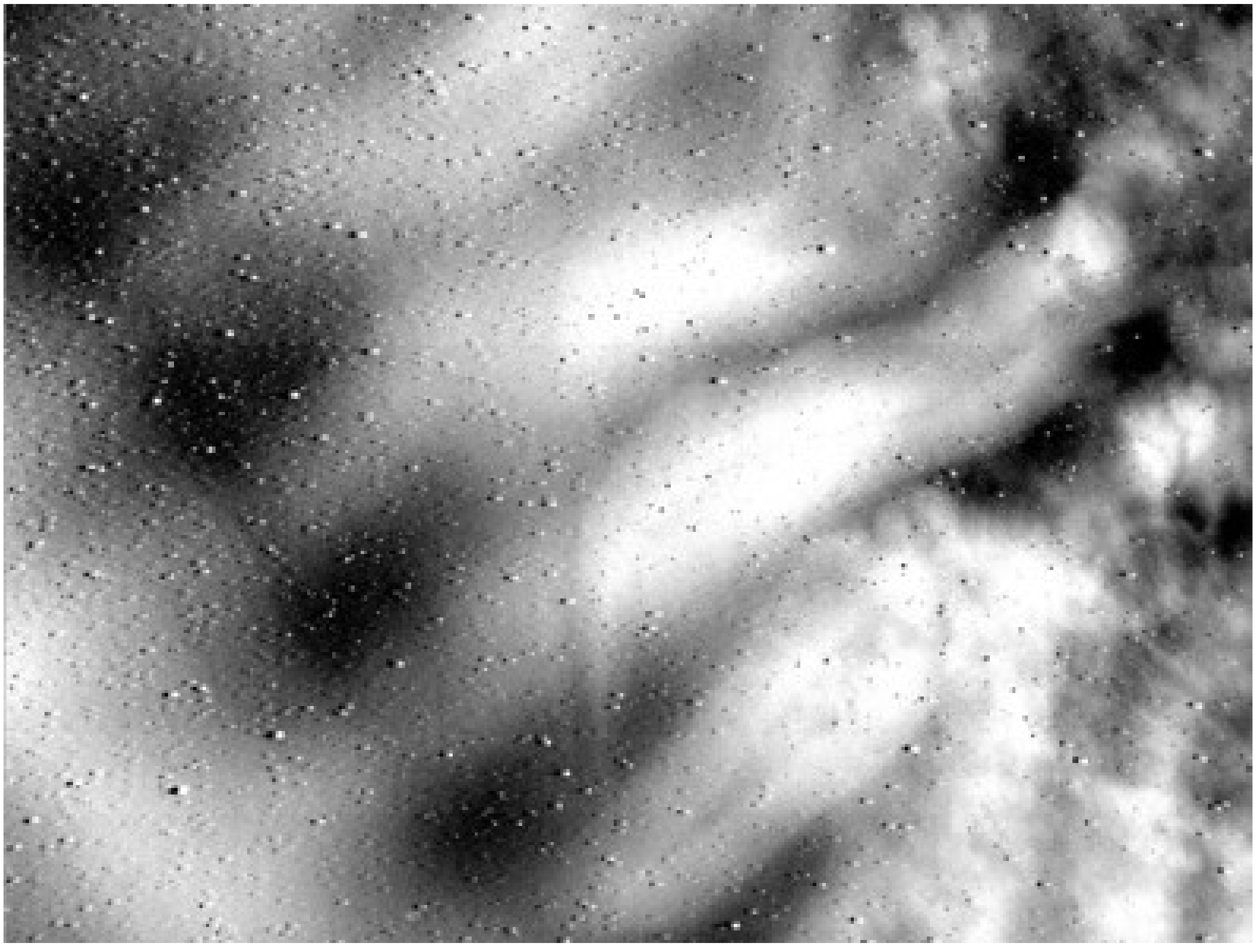

(b) Multiscale Kelvin-Helmholtz instabilities in mesospheric airglow (200 m – 10 km) (J. Hecht)

Figure 1.1: Examples of geophysical turbulence dynamics

ing of the small scale instabilities and intermittency driving GW forcing. One of the broadest goals of my research is improving the parameterization these models use in order to improve the model's description of our atmosphere. I aim to achieve this goal by refining our understanding of the energy and momentum deposition by GWs via instabilities using observations, analysis thereof, and comparison with simulations. Eventually this more accurate description of GW dynamics can be integrated into GCMs.

The Whole Atmosphere Community Climate Model (WACCM) provides one example of GW parameterization, described in depth by Gettelman et al. [33]. The best current resolution of WACCM is about 25 km, so it cannot resolve small-scale GWs, much less the instabilities they generate. Like other GCMs, WACCM uses parameterizations to describe the influence of orographic, convective, and frontal GWs. These parameterizations remain imprecise. For example, several modellers recently found that they could improve an underestimation in the Brewer-Dobson circulation by increasing the parameterization of Southern-hemisphere orographic GWs "somewhat arbitrarily" by a factor of 2. Moving from observations to implementing more accurate parameterization is an incremental process, but a necessary one for understanding and predicting the Earth's atmosphere.

1.3 Previous observations and modeling of GW dynamics

Scientists use ground, airborne, sounding rocket, and satellite-based instruments to image the character, spatial and temporal scales, and environmental context of GW and turbulence dynamics within the MLT. Dynamics within the MLT have been observed in the airglow layers and within polar mesospheric clouds acting as tracers [9] [17] [18] [29] [54] [73] [88] [93]). Meteor, MF, VHF, and UHF radar and Rayleigh and resonance lidar profiling have also been used to measure densities, temperatures, and radial winds [21] [50] [60]. Several facilities, including ALOMAR in Norway, Esrange in Sweden, and Poker Flat in Alaska, include a suite of instruments, and the aforementioned bases include rocket ranges, from which sounding rockets have been launched to study dynamics in situ [7]. However, none of the observational techniques available to us covers the full spatial and temporal range of resolutions we need to characterize GWs and their dynamics. Instead, we need to piece together as comprehensive a picture as possible of GWs and their dynamics from observations that cover a limited volume with as many correlative measurements as possible. I will discuss the observations and analysis of the PMC Turbo experiment in this thesis. Before describing our work, I want to outline other observational platforms available to the scientific community to show how we fit into the broader picture.

1.3.1 Instruments

The most straightforward method one could imagine to measure GWs would be to image them. Unfortunately, the atmosphere rarely cooperates. An imager cannot see dynamics where the atmosphere is transparent and low-lying clouds can block observations toward higher regions of the atmosphere. To image GW perturbations, scientists must take advantage of observables, such as clouds or thin layers revealed by radar or lidar profiling. Such observations must be opportunistic, since clouds move, dissipate, and are not guaranteed to be in the right place at the right time. The airglow of the MLT provides a more reliable and widespread tracer for GW studies. Scientists can observe GW disturbances in the OH bands from 85-90 km, O2 bands from 91-95 km, Na bands at 90 km, and the O I band from 95-100 km [37]. Scientists have also observed GW dynamics traced by Polar Mesospheric Clouds reflecting visible light between 80-85 km. Our own experiment used Polar Mesospheric Clouds as tracers and I describe them in detail in section 1.4. Imagers can cover a variety of fields of view at a variety of resolutions, depending on the engineering of the instrument. However, cannot directly measure the vertical structure of dynamics. While we have tried to implement tomographic measurements, such experiments multiply the logistical hurdles in setting up ground stations or remote platforms.

Scientists have used both Doppler radars and frequency-modulated continuous wave radars to study GWs at a range of altitudes. Other radars can measure backscatter from refractive inhomogeneities of temperature and humidity and can measure wind speeds through Doppler shifts. However, radars cannot resolve turbulence scales and their sensitivity decreases with altitude.

Lidars transmit a laser beam and measure the backscatter over time. Lidars have many uses and potential applications depending on the laser used. They measure densities (and thereby temperatures) by integrating backscattered light from clean air molecules and binning by return time, wind speeds via doppler shift, and they can track metallic species deposited by meteors entering the atmosphere (such as Na, K, and Fe) by matching the resonant frequency of the metal. While more difficult to build and maintain, lidars provide higher resolution than radars at similar distances. Some scientists have developed lidars that scan a region of the sky, but lidars do not achieve a horizontal field of view or small horizontal resolution comparable to imagers.

Each of these observation methods can observe only in a small altitude or horizontal range, while GWs propagate from the surface into space and travel thousands of kilometers. Lidars and radars have limited range resolution and airglow instrumentation captures data with large (5-10 km) vertical averaging. Lidars capture a vertical slice of dynamics while imagers capture a horizontal slice. Turbulence from GWs must be understood at the scale of inner turbulence to the scale of the GW wavelength. In the MLT, this covers a range from tens of meters to hundreds of kilometers.

1.3.2 Observation Platforms

The surface of the Earth is the oldest observation platform, and still the most commonly used for atmospheric physics. Scientists have developed sites in areas located near interesting, strong, and regular GW phenomena, such as the Arctic and Antarctic regions and in the lee of mountain ranges where steady winds lead to orographic GW generation. However, GWs travel horizontally on global scales and vertically to high altitudes. As a result, scientists have developed other platforms with benefits and drawbacks.

Small instruments carried by balloons, called radiosondes, have captured temperature and horizontal wind profiles up to 20-30 km altitudes. However, radiosonde launch frequency limits the time resolution they can observe (two per day is typically the maximum). Furthermore, many important dynamics occur above 25 km.

Scientists have mounted instruments in aircraft. This enables the experiment to move to a location of interesting dynamics and survey a selected region of the sky. This has allowed for measurements of GW horizonal wavelength spectrum and momentum fluxes. However, the duration of the flight limits measurements of GW climatology.

Rocket soundings capture in situ measurements in a vertical slice of the atmosphere at two horizontal points (during the ascent and descent). Ionization gauges measure the density at meter scale resolutions up to 110km to infer turbulence and temperature profiles during the ascent and descent. Some rockets drop falling spheres between 80-100 km that can be tracked with radars to measure drag and horizontal motion. From these data products, density, temperature, and horizontal winds can be measured from 90 km altitude down to 30-40 km. Other rockets introduce tracers into the atmosphere that can be triangulated by ground cameras to infer the horizontal wind profile during ascent and descent. However, an individual rocket launch lasts for a short time compared to the lifetime of GWs and do not capture a large horizontal field of view.

Satellite platforms allow for observation of GWs at global scales. Infrared and visible light imagers have flown aboard satellites, as well as instruments measuring temperature profiles. However, while satellite imaging platforms can observe global trends, the community has yet to find a way to achieve spatial or temporal resolution sufficient to observe relevant small scale structures. For example, the CIPS instrument aboard the AIM satellite images with a resolution on the scale of 1 km, but the inner scale of turbulence at the imaged altitude is about 20 meters [14]. Due to the nature of turbulence, understanding small-scale dynamics is critical in understanding instabilities, and achieving sufficiently fine resolution poses an additional observational challenge, especially to satellite-based instruments orbiting the Earth.

1.3.3 Modelling

While my dissertation research has not focused on modelling, I have collaborated with modelling teams during data analysis. Simulations provide important insight into the results and analysis I will describe. We analyze instability dynamics in order to quantify instability evolutions, time scales, and energetics. We collaborate with modelers to cross-reference observations (often from multiple instruments) with results from direct numerical simulations (DNS). We need observations to define boundary conditions for simulations and distinguish between models, while models can help us distinguish between the effects of atmospheric conditions that we are unable to measure. Models estimate metrics we cannot directly measure such as the turbulent energy dissipation and the turbulent kinematic viscosity. For example, DNS provide simulations that match our measurements of large-amplitude monochromatic GWs dissipating through transitional instabilities to turbulence. For certain initial conditions, they predict morphology of counter rotating vortices and the evolution into "horse-shoe" vortices that matches observations in nature [5] [25] [23]. When we observe features with morphology and scales that match these vortices, we can infer similar conditions as the models. Other DNS revealed the evolution from vortex rings to isotropic turbulence. The predictions from the DNS closely matched the form, evolution, and time scales of several observations of the MLT [29] [39] [54]).

1.4 Polar Mesospheric Clouds

Polar mesospheric clouds (PMCs), also known as noctilucent clouds (NLCs), provide a sensitive tracer of GW dynamics [88] [9] [74]. Polar mesospheric clouds are found between 80 and 90 km altitude. They have been used to study the upper mesosphere in a variety of ways, including the effects of anthropogenic emissions [76] [94] [75], comparing the northern and southern polar mesosphere [42] and large-scale GWs [14]. The focus of the research presented in this thesis will be the use of PMCs as a sensitive tracer of small scale instabilities in the MLT. PMCs are a few tens of meters to a few hundred meters thick and they reflect visible light strongly compared to the background sky brightness. The integrated backscatter changes as the PMC layer is perturbed by various dynamics. Not only can we observe large scale dynamics changing the backscatter of the PMC layer, but the thinness of the layer allows for resolution of dynamics approaching the inner scale of turbulence at the PMC altitude. These qualities make them sensitive tracers of dynamics including significant local advection and tracer gradients. We measure the backscatter from PMCs both passively using optical cameras and actively using lidar. With these instruments, we can image the dynamics leading to turbulence at a huge range of scales: extending from GW energy inputs at horizontal wavelengths of 20-100 km, through a wide range of scales of instabilities, to the inner scale of turbulence as small as 10-20 m.

PMCs form due to a local minimum temperature region of the atmosphere, which is cooled by the same dynamics we hope to trace with PMCs. The summer mesopause temperature minimum occurs due to adiabatic cooling by a rising and equatorward residual mean circulation in polar summer. This region of the atmosphere reaches extremely cold temperatures during the polar summer, with temperatures as low as 130 K, further modulated +/- 15 K by GWs driving adiabatic cooling. While the water vapour at these high altitudes occurs at extremely low densities, the low temperature cause ice particles to nucleate [55] [61]. The mechanism by which this nucleation occurs is poorly understood. Homogeneous nucleation seems unlikely due to the known presence of pre-existing aerosol particles. Scientists have identified several likely candidates for heterogeneous nucleation including sulfur dioxide, sodium bicarbonate, sodium hydroxide, and meteoric smoke particles [55] [62]. Scientists debate whether PMC properties can be affected by anthropogenic emissions of carbon dioxide (which cools the upper mesosphere) and methane (a source of mesospheric water vapour) ([76] [94] [75]. Scientists have also found that space traffic deposits sufficient water vapour in the mesosphere and could be a significant source of PMCs [71] [72]. While PMCs were first observed one year after the 1883 Krakatoa eruption, the connection between volcanic activity and PMC occurrence frequency is inconclusive [62].

While PMCs can be easily seen with the naked eye from the ground, ground observations introduce experimental challenges. Figure 1.2 shows PMCs over Northern Alberta that I photographed during early field testing of our instrument. From the ground, as we see in my photo, PMCs appear brighter than the sky due to the angle of reflected light. PMCs reside over the poles, and the ground observer sees light from the sun reflected off of high altitude PMCs toward their region where night has fallen (and the Earth blocks the sun). As a result, PMCs are typically observed at 60°-70° N and S latitudes. At these latitudes, the observer is close enough to the pole to see the high altitude PMCs, but not so close that the daytime sky brightness obscures the reflected light

Figure 1.2: Polar mesospheric clouds I photographed in High Level, Alberta (58 degrees North). The faint white features in the center of the image are PMCs, while the dark clouds are tropospheric clouds we see everyday. The PMCs reside at much higher altitudes at more polar latitudes. As a result, they are exposed to the Sun and reflect its light to more equatorial altitudes. During the day, PMCs are not visible due to bright daylight conditions, so we see them at dusk and night. During the summer (when PMCs form), the sky at the polar latitudes never gets dark, so we can only PMCs from the ground at an oblique angle from more equatorial latitudes.

from the PMCs. Unfortunately for scientific observers, these latitudes experience long summer days during the peak of the PMC season and daylight introduces a background signal that prevents observation of the PMCs. Since observers see the PMCs from a great distance towards the Northern horizon, spatial resolution is limited by the large off-zenith angle and distance to the PMCs. Finally, tropospheric clouds can obscure the field of view towards the PMCs, reducing the hours of observation during the PMC season.

Space-based platforms also observe PMCs. The CIPS instrument aboard the AIM satellite captures a wide strip over the poles every 90 minutes with a resolution of about 1km per pixel. While CIPS reveals important planetary scale dynamics and responses of the PMC layer, its spatial and temporal resolution is not sufficient to observe small-scale dynamics.

Recently, the E and B Experiment (EBEX) collaboration discovered that we can observe PMCs at a high spatial and temporal resolution with an angle that minimizes sky brightness noise throughout the PMC season by using balloon-borne platforms [54] [29]. I joined these research efforts at the beginning of my graduate studies, and have been integrally involved in the creation of a new balloon-borne platform designed specifically to observe PMCs. The subject of this dissertation is that experiment, PMC Turbo.

1.5 Serendipitous discovery of PMC images and the motivation for PMC Turbo

When I started graduate school, I planned to work on the EBEX analysis with my advisor, Professor Amber Miller, and the Columbia University Experimental Cosmology Group. Before graduate school, I had worked with the group to develop software that ran several pieces of hardware, including a millimeter-wave generator and a monitor for a cryostat.

EBEX was a balloon-borne experiment designed to make sensitive measurements of the cosmic microwave background. The EBEX team launched the experiment on 29 December 2012 and the flight terminated 9 January 2013. The results of the EBEX experiment have been extensively discussed in several papers [3] [1] [2] [15] [63]. The EBEX star cameras serendipitously captured high resolution images of PMCs, and this discovery prompted us to develop PMC Turbo, a balloon-borne instrument dedicated to imaging PMCs.

The star cameras consisted of optical cameras aligned along the boresight of the EBEX telescope. A cylindrical pressure vessel housed each star camera and also housed a computer and image storage. The computer associated with an individual star camera ran software which located stars in the images and compared them to a catalogue of stars in order to find the pointing of the primary EBEX telescope at a rate of with a precision of 1” in azimuth and elevation and 57” in roll with a rate of up to 0.5 Hz [2] [15].

The presence of clouds in star camera images surprised us, since the EBEX payload floated above 35 km altitude, much higher than most clouds. After review with several geophysicists, we discovered that the clouds were PMCs. The EBEX PMC images had a high signal-to-noise ratio and captured interesting MSD events. Furthermore, the altitude of the gondola allowed for a high signal-to-noise ratio despite the continuous polar summer sunlight. Ultimately, the discovery of the utility of balloon-borne payloads in capturing high resolution and high signal-to-noise ratio images of PMCs throughout the peak PMC season motivated us to build the Polar Mesospheric Cloud Turbulence (PMC Turbo) experiment. This thesis will describe the design, performance, and data collected by PMC Turbo.

The EBEX images had demonstrated the value of a balloon-borne imaging platform. I discuss an overview of the EBEX PMC image analysis in chapter 2. We designed PMC Turbo to capture images with similar resolution, but much larger field of view. The primary science payload of PMC Turbo consisted of optical cameras mounted aboard a balloon-borne platform that flew for about 6 days drifting with the mean flow at 38 km altitude. During this time, it captured images of thin tracers of GW dynamics in the MLT. Our field of view extended about 150 x 50 km, which approached the largest GW wavelengths, although we could not view the dynamics on global scales. We had resolution as small as 3 meters per pixel, while the inner scale of turbulence at this altitude is 20 meters. Our payload also included a Rayleigh lidar to capture the mostly vertical profile at one point. Our goal was to observe dynamics as they progressed to turbulence, so our observations required both the high resolution and large field of view.

The balloon-borne platform allowed us to view PMCs with time and space resolution only matched by the most sensitive ground imagers. However, the angle and location allowed by our balloon platform enabled us to capture images with this resolution during the peak PMC season for several continuous days, while ground based platforms can only capture images for a few hours a day due to long polar days in the summer. While our data quality matched ground based observations, our platform allowed us to collect the amount of data that a ground observation would collect over years. We recorded continuous measurements from a single season as well as coincident lidar measurements, which are much harder to get from the ground since the lidars and imagers cannot be co-located on the ground during most of the PMC season.

Chapter 2: EBEX PMC images

2.1 EBEX Overview

The discovery of PMCs in the star camera images from the E and B Experiment (EBEX) provided the motivation for the proposal of PMC Turbo. We discovered a valuable observational platform, we gained understanding of the sky conditions at both the balloon and PMC altitude, and we gained scientific understanding of the dynamics most interesting to probe. We designed our primary science payload using the EBEX star cameras as a blueprint.

EBEX included two star camera systems. A pressurized cylinder housed each camera and an associated computer. The cameras captured a field of view (FOV) of 4.1 degrees by 2.7 degrees with a 1536 x 1024 pixel resolution. They viewed at zenith angles around 36 degrees and the payload flew at 35 km altitude [54][1]. The EBEX star cameras captured 40,000 images during flight, roughly half of which contain PMCs. The EBEX group examining PMC images, including myself, worked with scientists at GATS to analyze these images and obtain scientific insight into the dynamics traced by the PMCs. Figure 2.1 shows several angles of an EBEX star camera interior from Figure 4.6 of Daniel Chapman's thesis [15].

2.2 EBEX cloud image analysis

The raw EBEX images included scattered light from the gondola, artifacts from the CCD, and darker circles from dust within the camera. Figure 2.2 shows a comparison of a cloudy EBEX image before and after this correction. While most artifacts could be removed with a combination of flat-fielding and gradient removal, my earliest work with images of PMCs involved the removal of dust spots, which we found scaled in relative brightness with the mean image brightness. Since the dust spots were stationary, I found that I could track this trend and scale the brightness of all

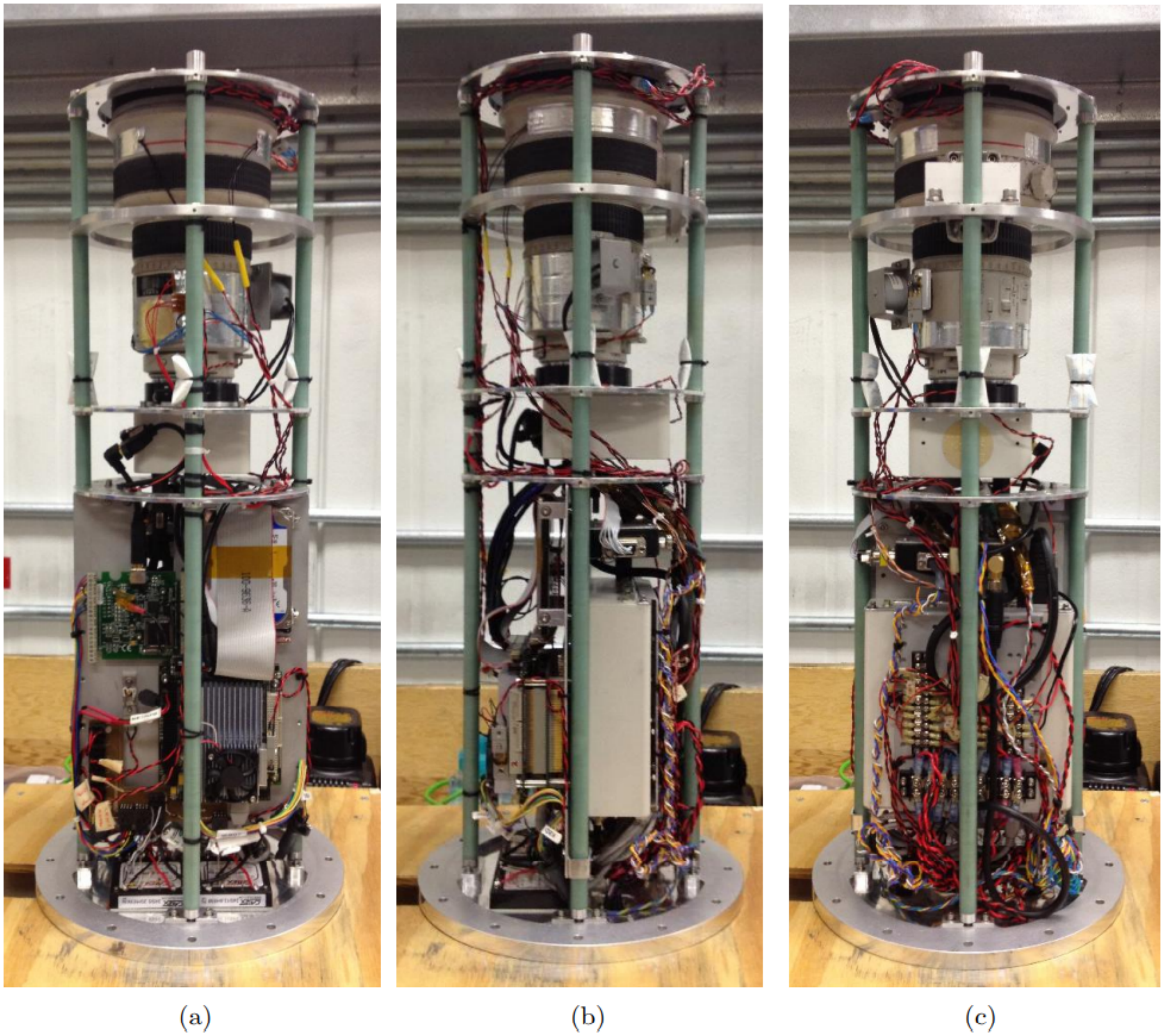
(a) (b) (c)

Figure 2.1: EBEX star cameras

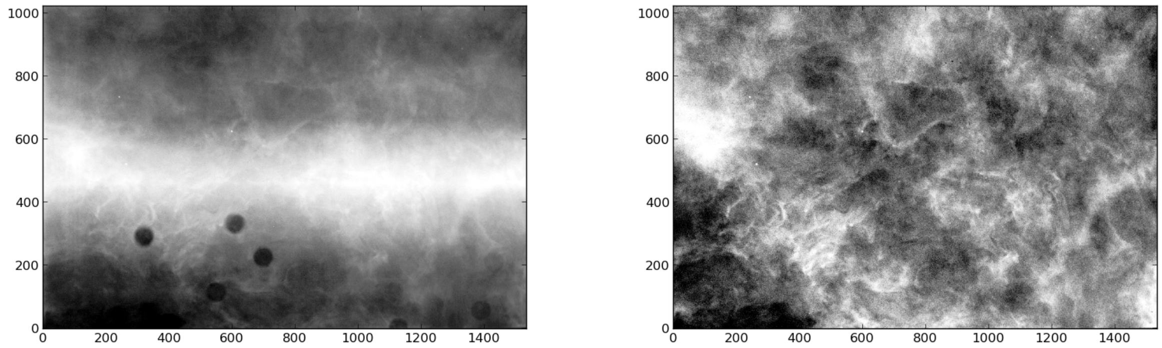

(a) Raw image from EBEX star camera

(b) Corrected image from EBEX star camera

Figure 2.2: Comparison of EBEX star camera raw and corrected images

pixels in the dust spot according to a first and second-order correction.

We also found a reasonably good way to filter images with no PMCs. Images with clouds had a larger contrast than images without. We quantified this difference using the median absolute deviation. However, EBEX also included images in which a section of the image included overexposed features, typically reflections from other hardware. These images had a larger contrast than cloudy images, so the images that were good candidates of cloudy features were found to have a range of MAD.

We also used the measured sky brightness and cloud signal from EBEX to predict the signal-to-noise ratio of PMCs we would measure during our flight. We used these predictions to select camera and lens hardware as we built the PMC Turbo camera systems. Section 4.5 describes these measurements, predictions, and design decisions.

2.3 Comparison between EBEX images and Models

The EBEX star cameras captured dynamics traced by PMCs with scales ranging from several kilometers to tens of meters. The resolution of these images at the PMC layer was less than 3 meters per pixel, while previous ground experiments had only achieved 10 meters per pixel resolution. These spatial scales provide sensitivity to the inner scale of turbulence. As a result,

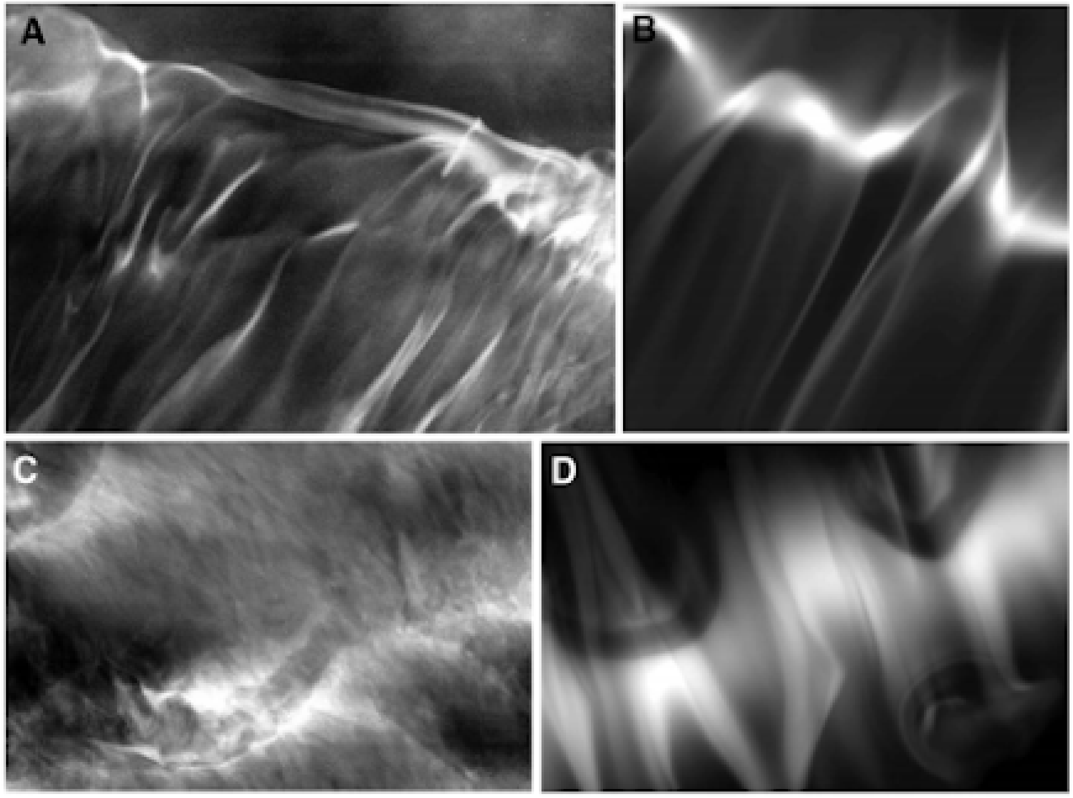

Figure 2.3: EBEX images and simulations of GW breaking fronts with trailing vortices

images from EBEX provided useful case studies to compare with numerical simulations of GW breaking and multiscale dynamics (MSD). While the details of the modelling are out of the scope of this dissertation, I will summarize these results, published in a 2015 [54] and 2017 [29] paper, to better inform the reader of the motivation and goals of PMC Turbo. As the EBEX group analyzed the data from the EBEX star cameras along with the science team at GATS, we recognized the unique opportunities that data from balloon-borne payloads offered, and we proposed PMC Turbo to build on the strengths of the EBEX data and shore up the weaknesses.

The 2015 paper published five sets of star camera images and accompanying model results highlighting similarities in the morphology of the image and model results. We found PMC images that show evidence of a GW breaking front with trailing vortices and associated vortex rings. Figure 2.3 from the paper (published as Fig. 1 in our 2015 paper [54]) shows both the EBEX images and snapshots from the model for this event. Panel A shows an EBEX image containing a GW breaking front while panel B shows the same dynamic in a simulation. Panel C shows semicircular features that could be laminar vortex rings, which panel D shows a simulation of vortex rings associated with GW breaking in a laminar flow. The vortex rings have diameters of about 2 km. Modelling results that match these dynamics suggests a vertical wavelength (λ_z) of 5 - 10 km. Such a vertical wavelength is typically associated with a GW with significant momentum deposition.

We also observed PMC images showing turbulent fronts that match multiscale simulations. Figure 2.4 panel A shows a single intrusion event, while panels C, D, and E show images from one camera's field of view as an intrusion event moves through it with a 30 s cadence. Panel B and F show simulated intrusion events similar in morphology to panel A and C-E respectively. This figure was published as Fig. 2 in Miller et al., 2015 [54]. Features can be identified to 20 meter scale, which matches simulations with an energy dissipation rate $\epsilon \sim 0.05 m^2 s^{-3}$. This energy dissipation rate is at the higher end of those measured by in situ instruments.

We observed turbulent wake and cusp-like features that match the morphology of various stages of GW breaking. The small scale (again around 20 m) suggest a higher Reynolds number (Re) (see Appendix A.3), in turn implying a larger GW scale. This infers similar energy dissipation rates to the previous event ($\epsilon \sim 0.05 m^2 s^{-3}$), but a Re an order of magnitude larger and $\lambda_z \sim 10 - 20$ km.

We also identified features that did not correspond to modelling results as well. We observed laminar features that match the morphology of extended and intertwined vortices, which can accompany KHI at small scales ($\lambda_h \sim 30 - 500$ km - compare to 4 - 5 km KHI presented in chapter 8). The small scale of the KHI implies weak background turbulence. We observed strongly turbulent flows with extended coherent features at a range of scales. We found turbulent features showing evidence of multiple PMC layers and modulation by KHI or GWs with horizontal scales of 1-3 km.

In the 2017 paper, we used the EBEX images in conjunction with modelling for a more quantitative analysis. We used our observations to refine boundary conditions for DNS to estimate the energy dissipation rates ϵ of the observed events. In particular, we use PDFs from DNS to estimate $< \epsilon >$ (domain average) and ϵ_{high} (the top 1%), which predicts the strongest turbulence. The

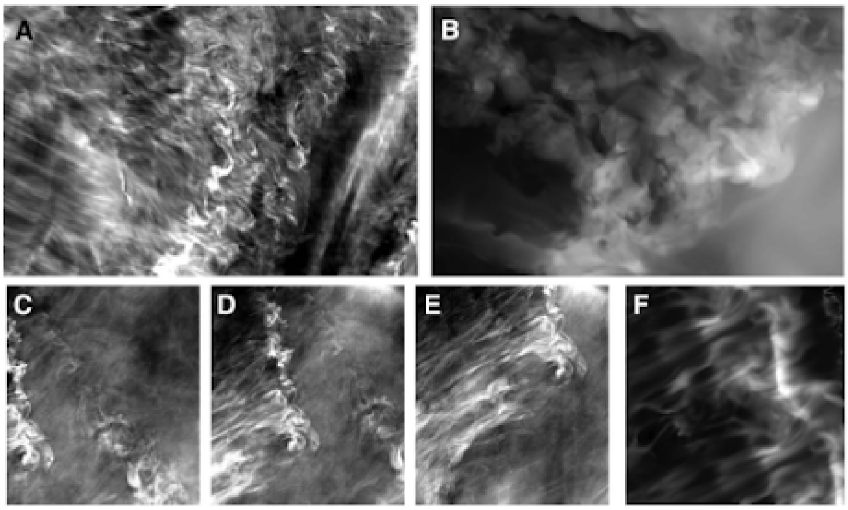

Figure 2.4: PMC images with turbulent fronts and corresponding multiscale simulations

nondimensional DNS is scaled by a scaling factor:

$$S = \frac{\lambda_z^2}{T_b^3} \tag{2.1}$$

where λ_z^2 is the vertical wavelength and T_b is the buoyancy period (see Appendix A.1).

While we can infer λ_z on a case by case basis, the buoyancy period T_b is

$$T_b = \frac{2\pi}{N} \tag{2.2}$$

where N is the Brunt-Väisälä frequency: the frequency at which a vertically displaced parcel of air will oscillate in a stratified atmosphere. I derive the Brunt-Väisälä frequency in Appendix A.1, and the result is given in equation A.22:

$$N = \sqrt{\frac{g}{\theta}\frac{d\theta}{dz}} \tag{2.3}$$

where g is acceleration due to gravity on the Earth, θ is potential temperature (also derived in Appendix A.1), and z is the vertical distance. θ varies on scales of 100s to 1000s of km due to tidal waves, planetary waves, and large scale GWs. We could not measure on these scales with the EBEX star cameras, which had fields of view of tens of kilometers. They can be measured by in

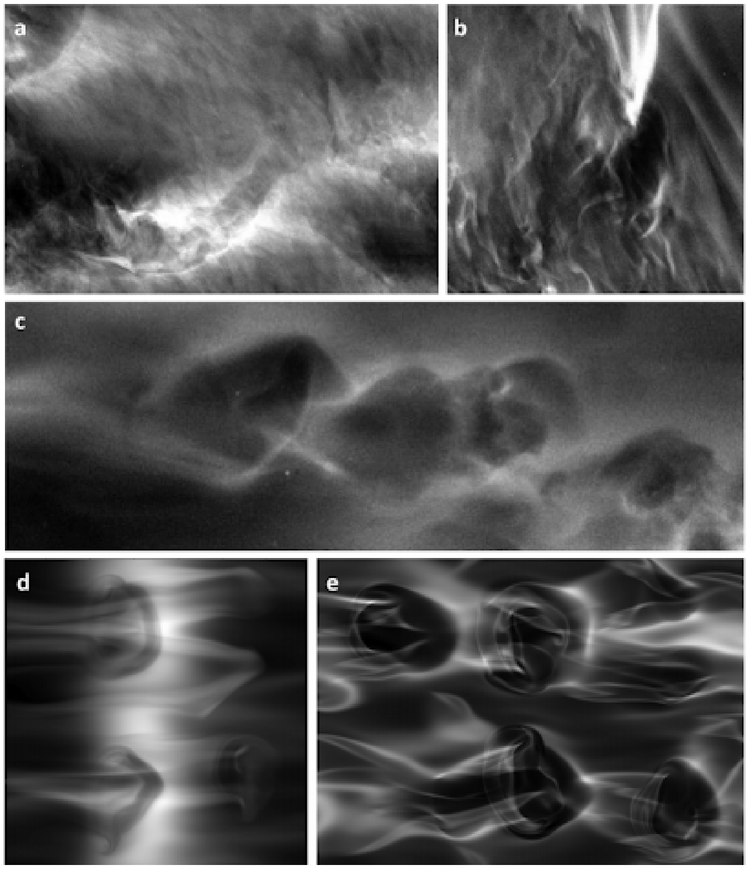

Figure 2.5: EBEX images and model results with vortex rings. Fig. 11 in the 2017 paper [29]

situ or ground-based instruments. For the 2017 paper, we used the measured PMC environment above ALOMAR [61] ($T \sim 150K$ and $N \sim 0.023s^{-1}$, which results in $T_b \sim 270s$). With our assumptions about T_b, we can find S for each case.

In Figure 2.3, we observe GW overturning front and diagonal pattern resembling model results. This suggests larger scale MLT dynamics are "characterized locally by approximately monochromatic GW breaking rather than less energetic MSD" [29]. Comparing the spacing of vortex features with simulations suggests a $\lambda_z \sim 2-4$km. The diagonal patterns suggest $\lambda_h > 5km$, but we cannot deduce the intrinsic frequency ω_i (the frequency of the wave relative to the flow or an observer moving with it). These measurements yield $S \sim 3-5Wkg^{-1}$, $<\epsilon>\sim 0.06-0.25Wkg^{-1}$, and $\epsilon_{high} \sim 0.7-2.6Wkg^{-1}$. The wide range of values is not just a function of the uncertainty in S, but also uncertainty in the correct model selection. These prediction match measurements taken at the PMC altitude of $<\epsilon>\sim 0.1-0.3Wkg^{-1}$.

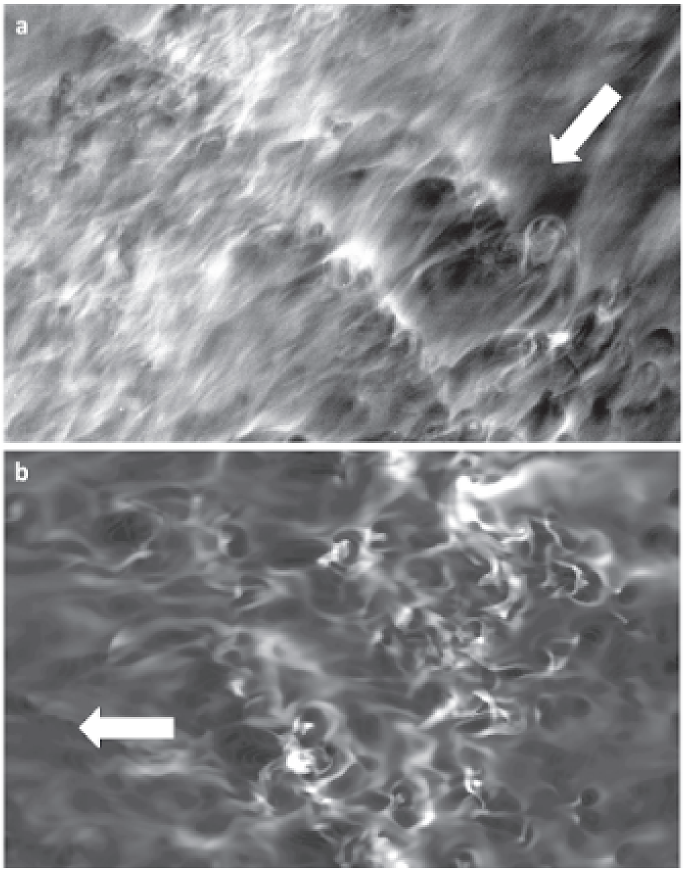

Figure 2.6: EBEX image and simulation of local GW breaking in region of MSD. Fig. 12 in the 2017 paper [29]

In Figure 2.5, we observe a vortex ring diameter of about 4 km. Panels a-c show EBEX images with vortex rings traced in the PMC layer. Panels d and e show simulations of vortex rings associated with GW breaking. This diameter corresponds to models with $\lambda_z \sim 8 - 10$km and the spacing between the rings suggests intrisic frequency $\omega_i \geq N/3$. Fig 2.5b shows a single vortex ring with a diameter about 1.5 - 2 km that is undergoing breakdown. There are no vortex rings nearby, suggesting $\omega_i \sim N/2 - N/1.4$. Panel c shows trailing vortices with diameter of about 1 km, suggests GW $\lambda_z \sim$ 2km and the spacing between the rings suggests $\omega_i \geq N/3$. The scaling between the model and these measurements yields $< \epsilon > \sim 0.004 - 0.01 Wkg^{-1}$, and $\epsilon_{high} \sim\sim 0.04 - 0.1 Wkg^{-1}$. This matches our expectations of smaller turbulence for GW breaking at smaller scales implied by the smaller observed features.

Figure 2.6 shows an EBEX image (panel a) compared with a DNS simulation of local GW breaking in an environment hosting MSD (panel b). The arrows show the direction of shearing in both images. In the EBEX images we observe cusp-like structures with longitudinal scales of 1 km and lateral scales of 100-300 m. This matched the simulated image captured at the edge of a region of local GW breaking with large ϵ. A comparison of the cusp scales between the image and simulation indicate a MSD depth of about 6 km, and 1 km sheet and layer structures. This event more closely matches simulations, resulting in a more precise estimation. $S \sim 2Wkg^{-1}$, $< \epsilon > \sim 0.016Wkg^{-1}$, and $\epsilon_{high} \sim 0.25kg^{-1}$.

Other PMC images matched MSD simulations with a GW and an oscillatory mean shear with a vertical wavelength 20% of the GW scale. These initial conditions interact to form a superposition of GWs with evolving amplitudes and phase structures. Associated instabilities include KHI, localized GW breaking, and fluid intrusions.

Our estimates of ϵ tend to be higher than several experimental measurements $\sim 0.001 - 0.3Wkg^{-1}$ [52] [53] [70] [20]. However, we found this reasonable since we could best match models to turbulence, so we had a biased sample of atmospheric conditions.

The data analysis highlighted the need for better measurement of the environmental N, influences of the background turbulence and turbulent viscosity (Re_{turb} and ν_{turb}), and re-evaluation of models to take into account the effect of turbulent viscosity.

2.4 Goals for PMC Turbo

While the images captured by the EBEX star cameras had high S/N and resolution, and our science team published novel scientific insights, we wanted to increase the field of view (FOV) and image cadence. The small FOV and low image cadence of EBEX was designed for precise pointing measurements, but it did not allow us to track events over several minutes, since the background winds would advect dynamics out of the field of view. As a result, we used the EBEX star cameras as a basis for the development of PMC Turbo, but we planned to increase cadence and FOV by using different cameras and lenses, as well as using more cameras to provide a large FOV.

Chapter 3: PMC Turbo Experiment Overview

3.1 Science Goals

We proposed PMC Turbo with the following science goals:

1. Identify the dominant GW, instability, and turbulence dynamics, scales and intensities that define the character and scales of GW dissipation events at PMC altitudes.
2. Assess the magnitudes and scales of GW momentum fluxes and momentum deposition, their statistics, and their implications for MLT forcing and secondary GW radiation.

We planned to meet these goals by capturing PMC images with sufficient resolution to resolve the inner scale of turbulence, as well as sufficient field of view to track turbulence dynamics through several buoyancy periods. We needed image cadence sufficient to capture the evolution of these dynamics.

3.2 Mission Overview

We designed PMC Turbo to operate at an altitude of ∼38 km beneath a helium balloon. At this altitude, within the stratosphere, the instruments float above most clouds and air. Our instruments image polar mesospheric clouds (also known as noctilucent clouds) residing at around 80 km altitude. Figure 3.2 shows a cartoon published by UCAR demonstrating the structure of the atmosphere with altitude, including temperature, human devices, and various atmospheric phenomena for reference. As shown in more detail within Figure 3.2, our cameras and lidar view upwards towards the PMCs (portrayed as a grey wiggly line) that form just below the local minimum temperature of the atmosphere. We must point our instruments at an angle from zenith to avoid the

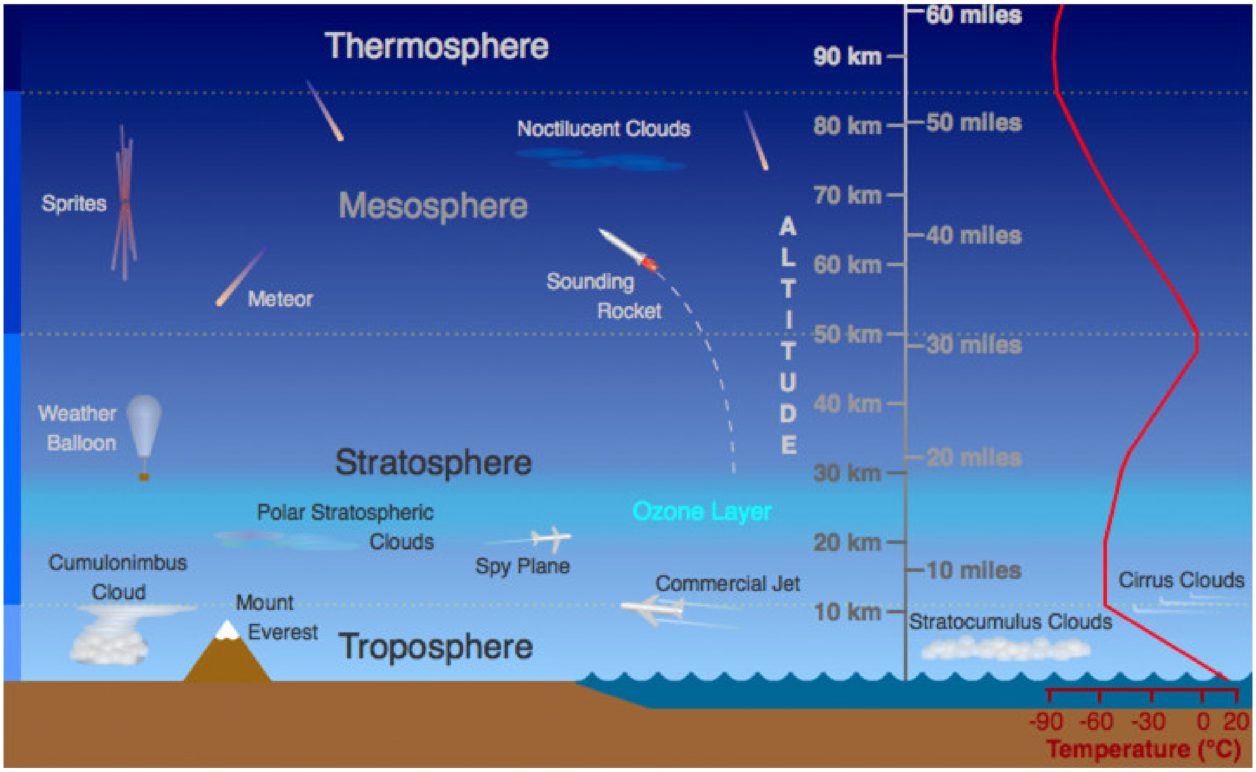

Figure 3.1: Structure of the atmosphere published by UCAR [66]

balloon directly above the platform. NASA's Columbia Scientific Balloon Facility (CSBF) supported the experiment and provided the balloon platform and support. CSBF launches balloon missions from McMurdo Station in Antarctica and Esrange Space Center in Northern Sweden that travel with the high-altitude polar vortex winds around the pole. Both sites allow balloon launches during the summer. Flights over Antarctica can stay aloft longer because retrieval of the balloon is easier over Antarctica. Arctic flights must be terminated if they appear to be headed North since balloons cannot be retrieved from sea ice. Furthermore, terrain in the Arctic limits balloon landing sites, and political boundaries introduce additional limitations in balloon landing sites. However, we launched from Esrange because there was a much shorter launch queue likely allowing for a flight to occur several years earlier. The altitude reached by the balloon allows for continuous viewing of PMCs with spatial resolution sufficient to observe the inner scale of turbulence and image cadence fast enough to track the evolution of turbulence dynamics. Floating at around 38 km altitude also elevates the observing platform above most clouds and other obscuring features

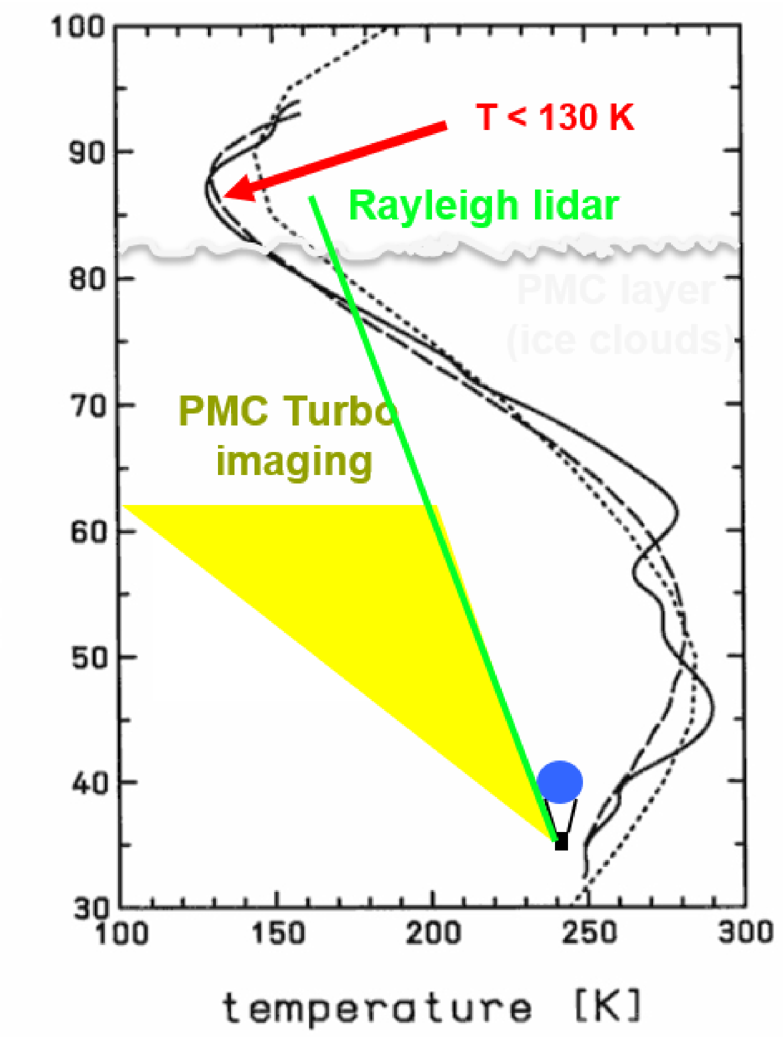

Figure 3.2: Atmosphere temperature and viewing configuration of PMC Turbo. The yellow swath represents the field of view of the optical cameras, while the green line represents the lidar beam. The black lines show the approximate atmospheric temperature with altitude.

Figure 3.3: The PMC Turbo flight

lower in the altitude.

We launched PMC Turbo on July 8th, 2017. Figure 3.3 shows a map of the nearly six-day flight of PMC Turbo, with each midnight (UTC) marked.

3.3 Instrument Overview

The PMC Turbo gondola consists of an aluminum frame supporting seven camera pressure vessels, one Rayleigh lidar pressure vessel and telescope, a telemetry system, and a power system. Figure 3.4 shows the CAD model of the PMC Turbo payload. Our primary science instruments consists of three narrow field cameras in pressure vessels (colored purple) and four wide field cameras in pressure vessels (colored blue). We use the NASA Support Instrumentation Package (SIP) for telemetry (colored orange). A Rayleigh lidar supports our primary science payload. The lidar box, associated telescope, and radiator are colored red. Figure 3.5 contains a photo of our integrated gondola hanging from the launch vehicle shortly before launch. Table 3.1 describes each of the major subsystems we flew on the gondola.

Our platform also hosts two small instrument packages designed to measure low frequency pressure variations (infrasound) in situ. These instruments do not form part of our primary science package, but we have spare weight and power budgets to host other group's experiments. We call this kind of configuration a "piggyback", and we later benefited from a similar arrangement,

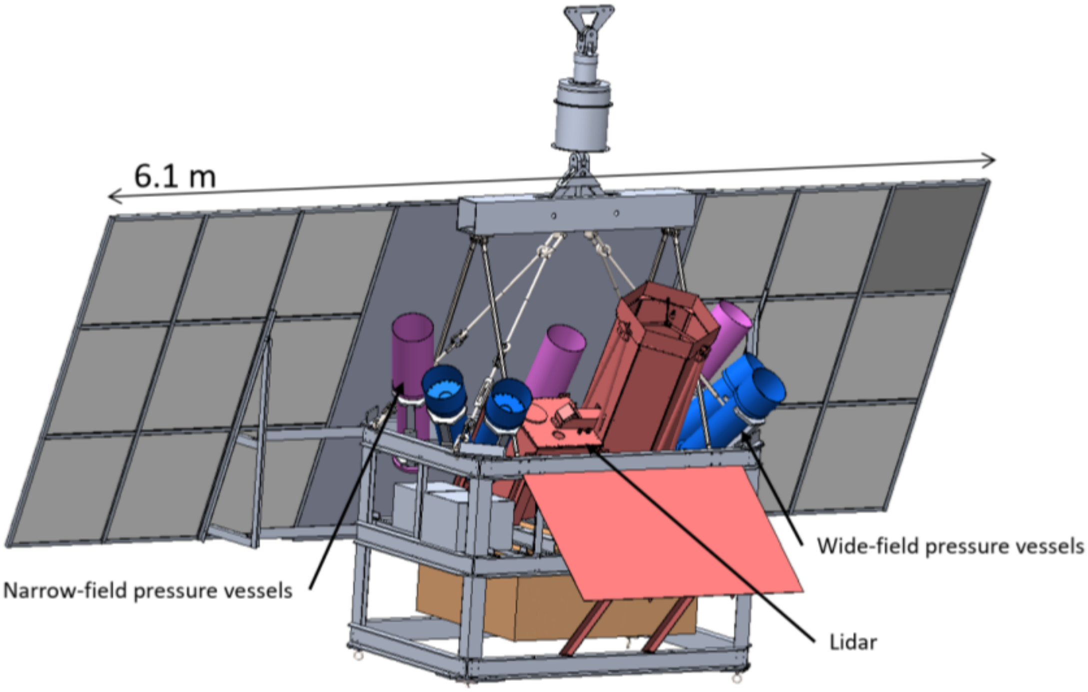

Figure 3.4: CAD model of the PMC Turbo gondola

described in Chapter 9.

Each of the seven pressure vessels on our gondola contains a lens, a camera, four spinning hard disks, and a computer performing data acquisition and flight control. Four of the pressure vessels have cameras with wide-field lenses mounted. These cameras cover a field of view (FOV) of 100 degrees x 40 degrees. The other three cameras have narrow field lenses mounted. Each of the narrow FOVs covers 10 degrees x 15 degrees pointed at the overlap of two wide FOVs. The lidar is the first high-powered lidar to be successfully flown aboard a balloon-borne platform. Figure 3.5 shows a photo of the integrated gondola.

3.4 Pressure Vessels

The pressure at 38 km altitude is much lower than surface pressure - so much so that balloon platforms are used as a testing ground for instruments designed to operate in space. Furthermore, we encounter large temperature swings between day and night due to the direct sunlight and the low heat capacity of the thin atmosphere. We use pressurized vessels to control air pressure and

Figure 3.5: Photo of the integrated PMC Turbo gondola shortly before launch.

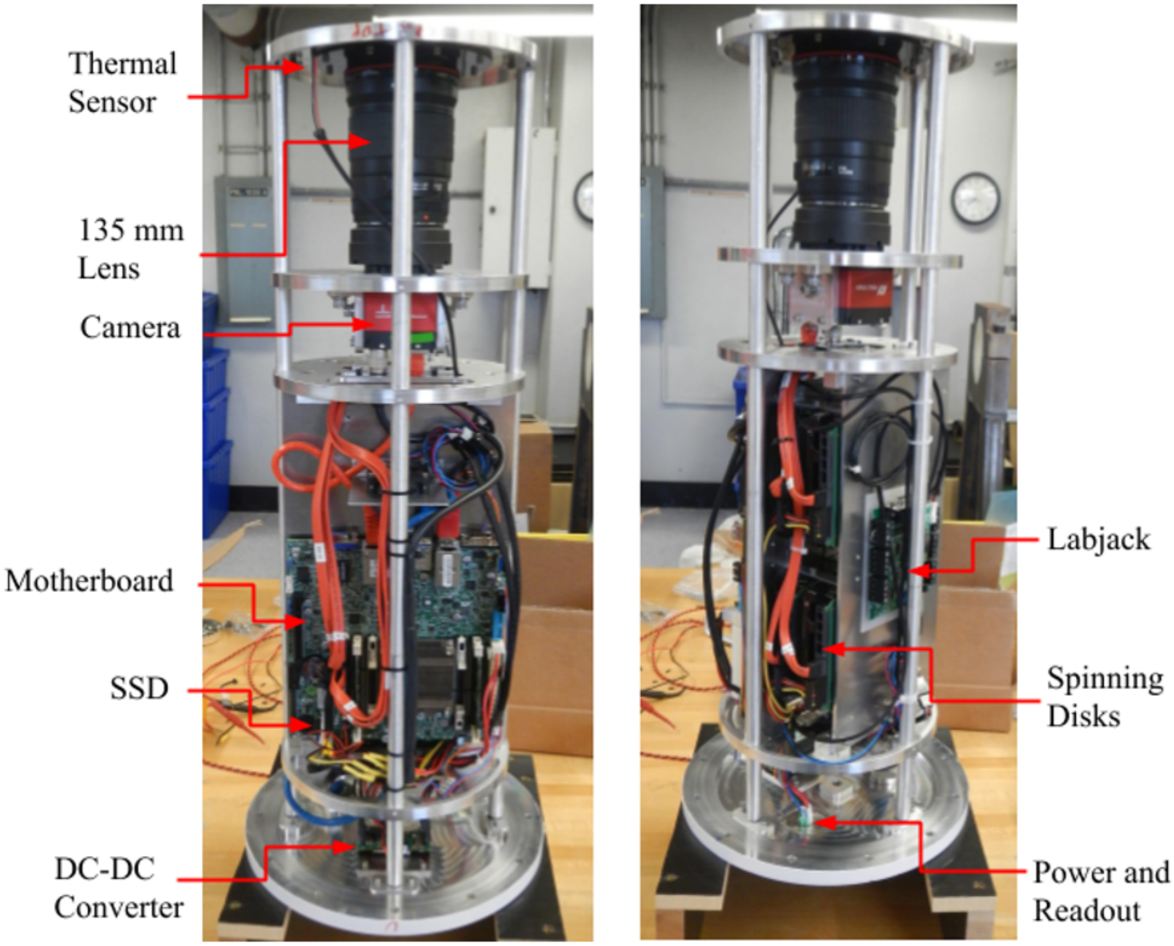

Figure 3.6: Pressure vessel contents

temperature of the lenses, cameras, hard drives, and computers that are not verified to operate in a vacuum.

Since the cameras capture data for our primary science objective, our design ultimately centers around them. I describe the design and development of our cameras in detail in Chapter 4. I describe the other internal hardware, and the pressure vessels themselves here. Figure 3.6 shows two views of the contents of a pressure vessel, including the camera, computer, disks, and sensor system.

3.4.1 Computers

Each pressure vessel contains a computer running the image capture process. Each computer also runs flight control and telemetry software. Chapter 5 covers the software in-depth.

We use Supermicro mini ITX A1SAI-2750F-O server motherboards. These motherboards are designed for industrial server use. We selected this motherboard because it provided a small form factor, ample processing power, low power consumption, ECC memory, support for enough hard disks and ethernet ports, all at a small fraction of the cost of an industrial or ruggedized computer more typically used for balloon applications. However, the motherboards are significantly cheaper and more capable than UAV style motherboards. The motherboards include an industry standard Intelligent Platform Management Interface (IPMI), which we used to set-up the system and diagnose issues over the ethernet interface without needing to re-open the sealed pressure vessels - we have no need for ports for dedicated monitor, keyboard, mouse, etc. The motherboards also have sufficient SATA and ethernet ports that no additional adapters are needed. No other motherboard has the necessary I/O connections built in. We have no need for redundancy in the motherboard due to redundant pressure vessels. Figure 3.7 shows a closeup of one of our computers integrated within the pressure vessel frame.

A LabJack U3-HV USB data acquisition unit records the temperature from several Analog Devices AD590 sensors and NXP MPX4250A board mount sensor measures the internal pressure. We downlinked these statuses to monitor conditions inside the pressure vessels during flight. We mounted the labjack beneath the drives in our pressure vessel and one is labelled in Figure 3.6.

3.4.2 Drives

In each pressure vessel, four Western Digital Red 8 TB (WD80EFAX) spinning disks store the experiment data. While we ultimately flew in the Arctic, we originally designed the instrument for a longer duration Antarctic flight, so we included 224 TB of total storage on our instrument to provide sufficient storage for a two-week Antarctic flight.

The computer writes images to the four disks in a roughly alternating manner so that a disk

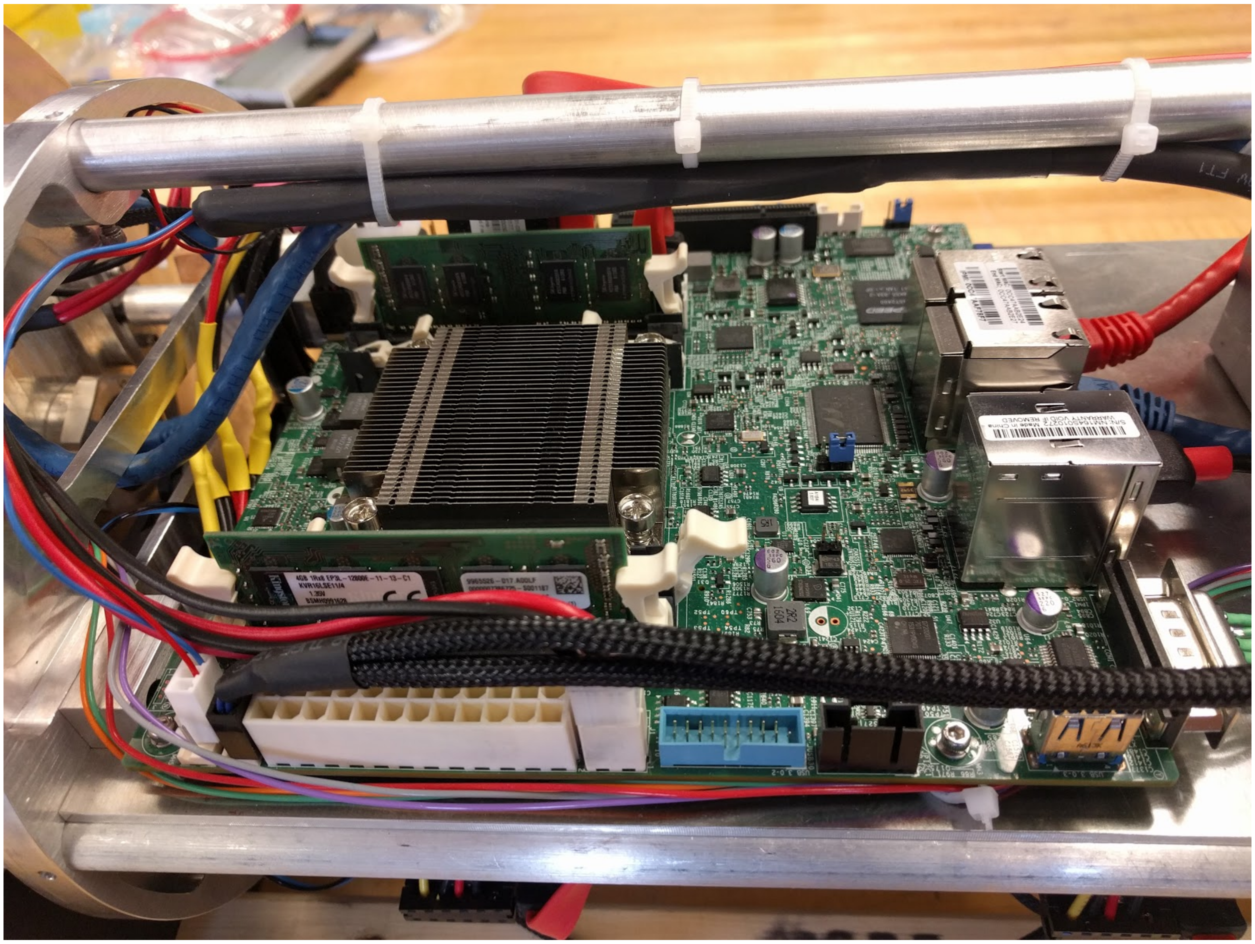

Figure 3.7: Pressure vessel computer

failure does not remove a continuous section of flight. We also wrote one image every few minutes to a generic 128 GB SanDisk Cruzer USB flash drive as an alternative storage medium, in case all spinning disks failed unexpectedly. We set up the Debian operating system on a RAID array with three-times redundancy on two spinning disks and a dedicated ADATA ISMS312 industrial 32 GB SSD.

3.5 Onboard network

We enabled communication between subsystems and the telemetry systems with an onboard network. NASA provides a standardized package for telemetry, as well as an antenna dedicated to an Iridium Pilot connection. We connected to the SIP via Ethernet to RS232 converters and formatted our commands and downlinked data to the SIP specified formats. Iridium Pilot behaved like a standard internet connection from the user perspective, so connecting our network just required an ethernet cable.

We connected our local network with two Ethernet switches, each with a connection to a dedicated RS232 converter. We used Cat6 grade Ethernet cable and tested our cables, switches, and converters in a thermal vacuum chamber to ensure operation at float altitude. The switches and RSS232 switches were not entirely redundant. Each switch communicated to a subset of pressure vessels, while each RS232 communicator connected to one of two redundant communication channels on the NASA SIP system. If we lost an ethernet switch we would lose communication to that subset. However, the dual switches prevented loss of the entire payload if one malfunctioned.

CSBF also provided a science stack, which communicated over the same channels provided by the SIP. We included readout from our experiment for the science stack, and the stack included discrete command outputs. We used the science stack as a backup for our own telemetry and readout systems.

We designed custom communication software to meet our expected needs and flight conditions. I describe this software in section 5.3.

3.6 Power

The PMC-Turbo power system consists of 15 solar panels made by SunCat Solar, LLC. These panels connect to two independent battery boxes. Six panels connect to one battery box, which powers five of the seven pressure vessels. Nine panels connect to the other battery box which powers the remaining two pressure vessels and the lidar subsystem. These power systems are separated to reduce the number of single-point failures of the experiment. Each set of solar panels are connected to a battery box with a TriStar MPPT charge controller, which supplies power at the appropriate voltage to two Valence 24V lithium iron magnesium phosphate batteries with a combined capacity of 1 kWh. The lithium batteries are connected to a custom relay board, which distributes power to the pressure vessels and lidar connected to the battery box. The power for

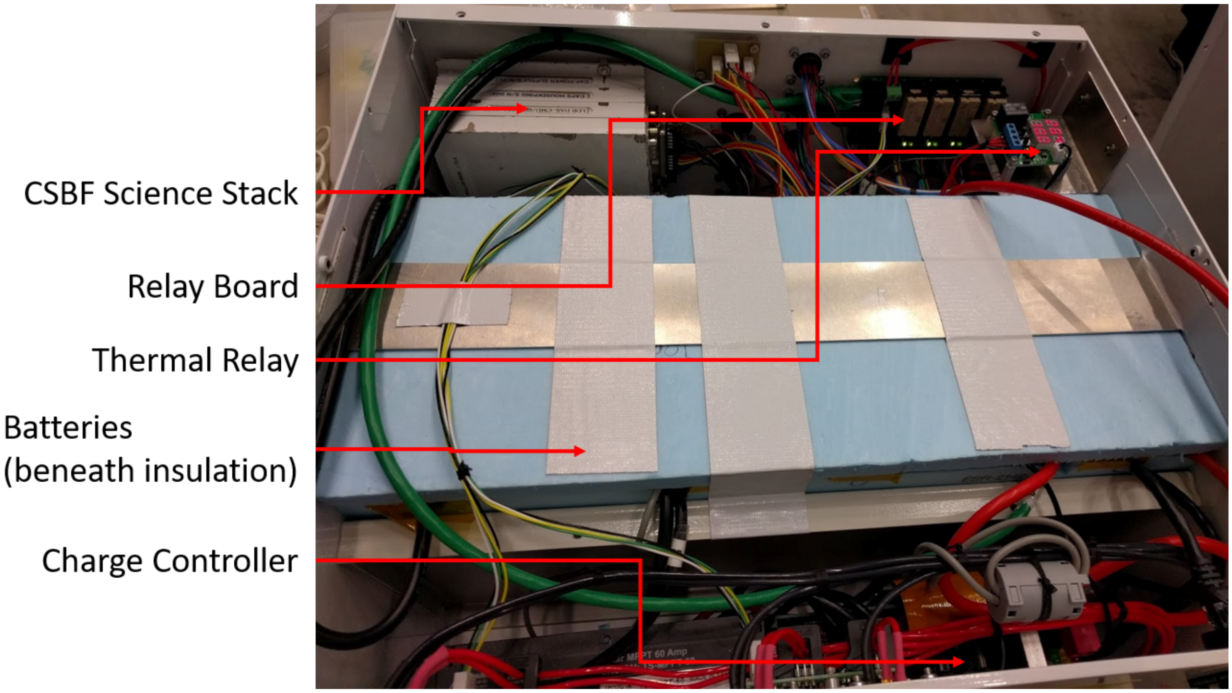

Figure 3.8: Interior of one of the PMC Turbo battery boxes

each subsystem is routed through a latching relay. Figure 3.8 shows photo showing the charge controller, relay boards, and insulation for the batteries inside the battery box.

The relay board directly interfaces with the CSBF science stack, bypassing our own communication system. The ensures that we can still control and monitor the power to our pressure vessels even if a computer crashes or we have a communication glitch. The cables connecting the power relay boards and pressure vessels include wires which read out analog signals monitoring voltages, currents, and pressure. In addition to these measurements, the relay board routes analog signals for the battery voltages, solar cell currents, and lidar currents to the CSBF science stack, which sends the housekeeping data to the ground on a separate channel from the main experiment readout. This provides a redundant system status measurement in case of malfunction in the more sophisticated flight control software running on the computers contained within the pressure vessels. Even in the event of pressure vessel failures, the ground team can monitor currents, voltages, and pressures of the various subsystems, which provides basic diagnostic information. The ground team can also power subsystems on/off using the CSBF science stack directly to open/close relays. Furthermore, in the case of a catastrophic failure (such as a short), an individual subsystem could be electrically disconnected from the rest of the experiment. We designed all subsystems to automatically start in a nominal configuration upon power up.

On the pressure vessel side, DC power is supplied to the pressure vessel directly from the battery bus, and a high efficiency DC/DC converter (UIE48T10120) regulates to +12 VDC with and directly powers the motherboard. All other components inside the pressure vessel are powered from the motherboard, eliminating the need for additional relays or control circuitry.

During ascent, we do not have pointing to keep our solar panels oriented towards the sun. We needed to preserve battery capacity for heaters to keep the lidar coolant liquid during ascent, and without sufficient data on the convective cooling of the troposphere, we left two pressure vessels powered off to keep a safe margin in our power budget. After we reached float and began pointing our solar panels towards the sun, we never used more power than the solar panels provided. Additionally, we opened the relays shortly before termination to prevent damage to the spinning disks from the forces resulting from the parachute or ground impact.

3.7 Rayleigh Lidar

The PMC Turbo payload included the Balloon Lidar Experiment (BOLIDE), the first high-power lidar to be successfully operated on a balloon platform. A team from the German Aerospace Center (DLR) developed the instrument and we worked with them to integrate it with our power and telemetry system. A lidar sends out light and measures the return backscatter as a function of time. Lofting a lidar beneath a balloon gives several experimental advantages. At 38 km altitude, the sky brightness noise for the lidar is reduced by two orders of magnitude compared to the ground. The backscatter signal also scales as one-over-distance squared, and the balloon is about half the distance to the PMC layer from the ground. We also had the capability to take coincident measurements of PMCs with both the lidar and images since both instruments were mounted on the same platform. For a detailed description of the instrument, I recommend that an interested reader review the technical paper the DLR team published [46].

BOLIDE includes a 532 nm laser with an average output of 4.2 W, 100 Hz pulse repitition

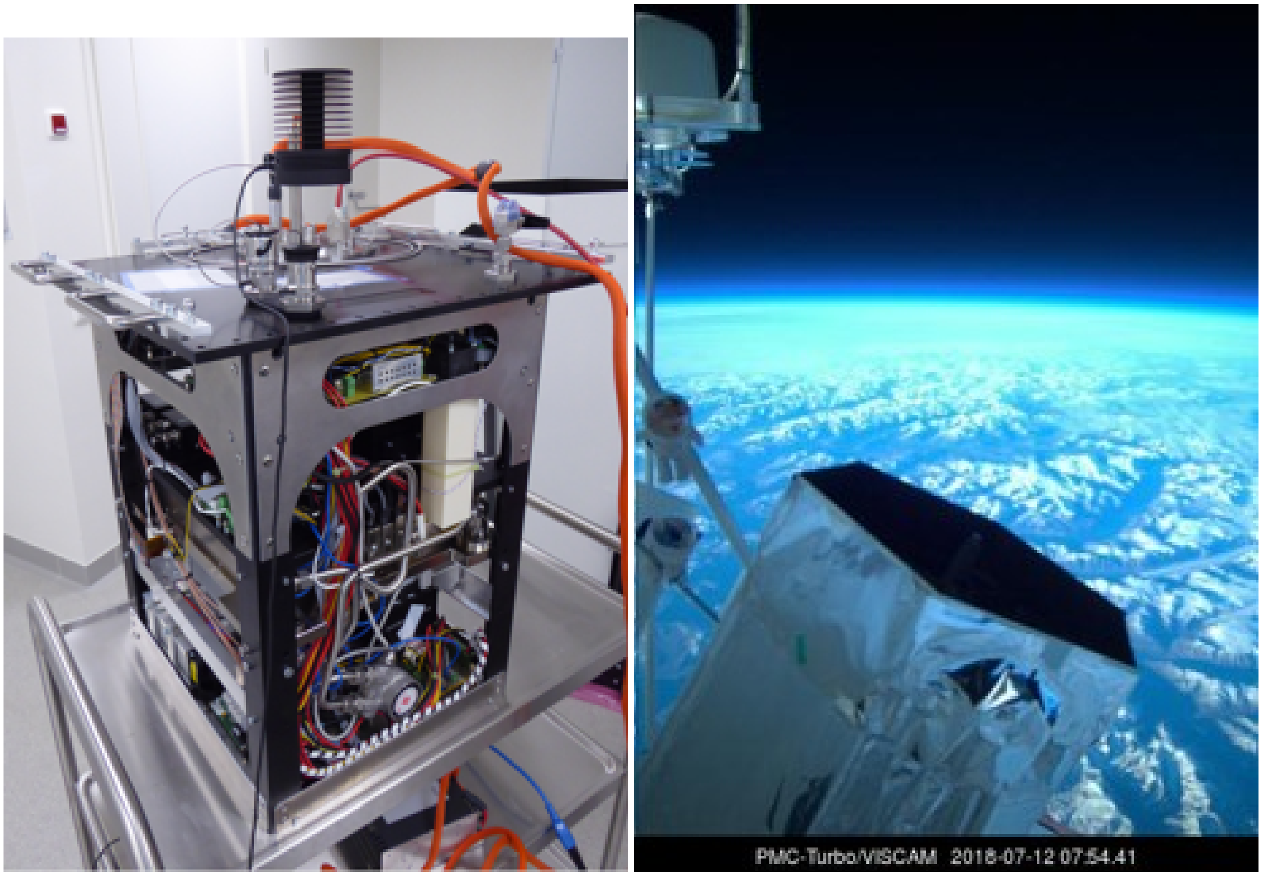

(a) Contents of lidar pressure vessel

(b) View over lidar telescope at float

Figure 3.9: The Rayleigh lidar flown aboard the PMC Turbo gondola

frequency, and 5 ns pulse length. A pressure vessel houses this laser and a computer running the instrument, telemetry, and collecting data. Figure 3.9 panel a shows the contents of this pressure vessel. The beam from the laser is transmitted into the sky and a 0.5 meter parabolic mirror telescope receives the return signal, which is sent to detectors in the lidar pressure vessel. Figure 3.9 panel b shows a view at float across the aperture of this telescope. The lidar included a radiator circulating liquid glycol for cooling. Both the telescope and radiator feature prominently at the front of the gondola in Figures 3.4 and 3.4.

The DLR team pointed the laser beam 28 degrees off-zenith. This avoided the balloon, and coincided with the center of the collective field of view of the cameras in azimuth and the upper edge of their field of view in elevation. A cyan dot marks the location of the beam in the projected image in Figure 8.1 in Chapter 8.

3.8 Telemetry Channels

NASA provides telemetry hardware with their balloon infrastructure and we used these telemetry channels to meet our requirements monitor and command our subsystems. Our own communication software was designed with the NASA telemetry in mind and I describe the software we designed for the gondola and the software we used to send and receive data from the ground in Chapter 5.

The Columbia Scientific Balloon Facility (CSBF) provides the SIP (Support Instrumentation Package) to ballooning science groups. Their telemetry package includes four communications antennas; two communicate with the Iridium network and two with the TDRSS network.

TDRSS is a network of communication satellites used primarily by NASA and the military. They were primarily launched in the 80s and 90s and can have missing reception at the poles due to their equatorial orbit. Iridium is a private satellite network, which was launched in the late 90s and early 2000s. They maintain connection over the poles due to longitudinal orbits and their low earth orbit.

The SIP also includes high bandwidth Line-of-Sight (LOS) telemetry accessible while the gon-

Component	**Description**
Cameras (7)	Allied Vision Prosilica GT 4907, Kodak 16070 CCD (3232x4864 pixels), shutterless, high frame rate, burst-mode imaging options, custom auto-exposure algorithm.
Camera lenses	Canon 50 mm f1.4 (4), Canon 135mm f/2 (3), L series, apochromatic
Computers (7)	Supermicro ITX Server boards with Intel atom processor. Three times redundant RAID OS on SSD and spinning disk partitions. Attached Labjack A/D boards monitor detailed housekeeping.
Data storage	28 8-Tb Seagate drives, 32 TB for each imaging system
Pressure vessels	0.5” Al cylinders (7), powder coated, 1200 hPa pressure, each hosting a camera, lens, computer, 32 TB storage, full system software control/comms./data link
Power system	Suncat solar panels (15), TriStar MPPT 60 A charge controllers, Valence U1-24RT batteries, 1370 W in 2 circuits, split camera and lidar loads, redundancy against a single circuit failure, switchable loads, 2 kWh battery ascent backup. Relay boards connected directly to NASA SIP provide analog housekeeping over power umbilicals and direct power control
Rayleigh lidar transmitter and receiver	532 nm wavelength, 100 Hz PRF, 45 mJ/pulse, 5 ns pulse length, fiber coupled, 0.3 nm bandwidth, photon-counting avalanche photo diodes, active thermal control, 1.6 m2 radiator, commercial flight computer with i5 processor, 1 TB redundant flash storage, FPGA-based I/O controller, Linux OS, C++ software
Telescope	0.5-m f/2.4 quartz mirror, protected Al coating, 165 µrad FOV
NASA SIP	Linux OS. Camera interface written in C. Image processing, telemetry, and flight control written in Python. Distributed flight control capability for redundancy.
Network	Resilient coordinated network of computers. Gigabit Ethernet. Synchronized image capture to 10 ms. Serial-to-ethernet interface with NASA SIP.

Table 3.1: Component descriptions

dola remains close to the launch location. We maintained LOS for roughly 24 hours, including launch.

We access the Iridium network over three links: Iridium pilot, the short-burst data, and the dialup mode. Pilot has a separate dedicated antenna, an order of magnitude larger bandwidth, and uses a different communication protocol from other Iridium channels. Whenever possible, we use Iridium Pilot, since the network consistently reaches a bandwidth of 100 kilobits per second (kbps).

Link	**Satellite Network**	**Bandwidth**	**Image Cadence (15 kB image)**	**Image Cadence (200 kB image)**
Pilot	Iridium	80 - 100 kbps	1.2 s	16 s
Short-burst data (SBD)	Iridium	255 bytes/min	-	-
Dialup Mode	Iridium	<= 2 kbps	60 s	13 mins
Omni-directional antenna	TDRSS	6 kbps	20 s	4 mins
High-Gain Antenna	TDRSS	<= 92 kbps	1.3 s	17 s
Line of Sight (LOS)	LOS Antenna	115 - 234 kbps	0.5 - 1 s	8 - 16 s

Table 3.2: Downlink comparison

The Iridium dialup mode has 2 kbps bandwidth compared to the 100 kbps of Pilot, but provides an alternate channel on a separate antenna. The short-burst data mode reliably sends a 255 byte message at a one minute cadence. We use these short messages to send essential housekeeping data.

The TDRSS system includes a high-gain antenna and an omni-directional antenna. The high-gain channel has a bandwidth of around 92 kbps, while the omni-directional antenna gives 6 kbps. The gondola also communicates with a line of sight system for the first 24 hours of flight. In the ideal operation scenario after we float out of range of the LOS link we will use the Iridium Pilot connection and the TDRSS high-gain antenna for a total downlink bandwidth of about 200 kbps. Table 3.2 shows a comparison of the various communication channels included in our telemetry system, as well as downlink speeds of data compressed by the Controller software moduel (described in section 5.3.4.

We communicate with the SIP through an RS-232 interface. Iridium Pilot is an exception - we connect to the Pilot antenna directly via Ethernet. We use two RS-232 to Ethernet converters to connect to this interface, and wrote communication software capable of communicating over a variety of links (see section 5.3.3). The consolidation of our network over Ethernet and standardization of communications allows us to implement a distributed flight control system described in section 5.3.2.

The SIP also includes a science stack and GPS system. We include commands on the science stack to flip relays connected to our instrumentation, so we can power cycle or shut off misbehaving instrumentation that we are unable to contact using the primary TDRSS or Iridium channels.

The lidar team requested 16 kbps of bandwidth to the LIDAR whenever possible, which included 4 kbps for the IR imager. While the LOS link is active, they requested 50 kbps for an initial calibration, and anticipated a testing and configuration period of 1-3 hours. This bandwidth represents between 10-20% of our total downlink bandwidth. In the case of a problem with an individual camera or the lidar subsystem, we can give the functional systems less bandwidth and focus on troubleshooting.

3.9 Integration, Launch, and Flight Overview

We spent nearly 60 days integrating and testing our payload in Palestine, Texas at the Columbia Scientific Ballooning Facility (CSBF). At this location, we performed flight readiness tests on our hardware and software, including the thermal vacuum tests outlined in Chapter 4. We also integrated the components developed at University of Minnesota, GATS, and Columbia, as well as integrated our experiment with the CSBF standard balloon hardware.

After we had passed communication and flight simulation tests, we disassembled our experiment and shipped it to Esrange Space Center near Kiruna, Sweden. We rebuilt our experiment, reintegrated the various subsystems, and repeated the hardware tests to make our experiment flight-ready. Figure 3.10 shows the hangar at Esrange as the CSBF team hoisted our fully-integrated gondola to weigh and select an appropriate amount of ballast for our flight. We waited for suit-

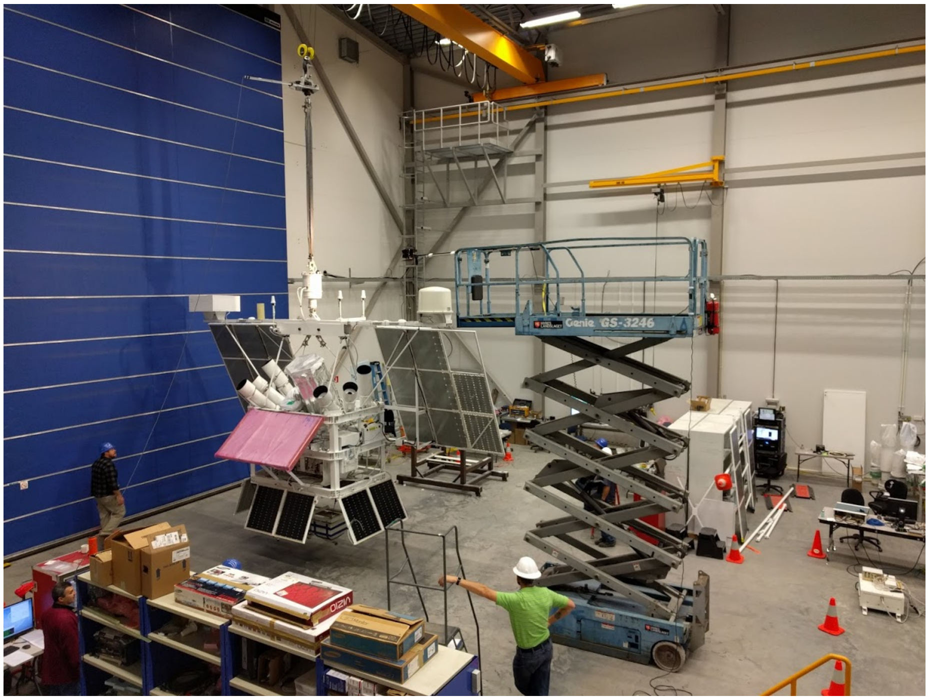

Figure 3.10: PMC Turbo gondola weighed for ballast in hangar at Esrange

able flight conditions. Balloon experiments require specific wind conditions for launch and several hours of stable conditions preceding launch while the flight team prepares. We had eight attempts that scrubbed due to uncertain weather before we finally launched from on July 7th, 2018 (07:30 UTC, 21.1°E, 67.9°N). Figure 3.11 shows a photo of our field team standing in front of the integrated payload during a launch attempt at Esrange Space Center. From left to right they are Christopher Geach, Bernd Kaifler, Bifford Williams, and C. B. Kjellstrand (the author).

The balloon floated westward over Greenland and Baffin Island before termination over western Nunavut on July 14th (05:30 UTC, 109.4°E, 66.8°N). The balloon remained between 37 and 39 km altitude between ascent and termination. Upon landing, the instrument sustained only superficial damage and it was recovered by July 22nd. During flight, the PMC Turbo cameras captured about 6 million images, of which about 60% contain images of PMCs.

Figure 3.11: PMC Turbo field team

Figure 3.12: Gondola at recovery site

3.10 Recovery

We terminated PMC Turbo over western Nunavut on July 14th (05:30 UTC, 109.4°E, 66.8°N). The payload landed upright on the tundra. Due to the remoteness of the landing site, the recovery team took several days to recover the payload. They shipped the pressure vessels (containing the hard drives) in a shipping container with another recovered balloon experiment going directly to our lab in Colorado, and they shipped the remainder of the PMC Turbo instruments to the CSBF facility in Texas. We travelled to Palestine to assist Bernd Kaifler in the retrieval of the DLR lidar data and hardware, packed the remaining gondola components into a truck, and drove them back to Boulder.

As seen in Figures 3.12 and 3.13, the PMC Turbo gondola landed upright and with little dam-

Figure 3.13: Aerial view of gondola at recovery site

age. The NASA SIP, associated solar panels, and ballast hopper on the bottom of the payload took the brunt of the impact, but our instruments had nothing more than superficial damage. Even the fragile and exposed lidar radiator on the front of the payload survived.

Chapter 4: PMC Turbo Cameras

The PMC Turbo science goals required a similar spatial resolution and signal to noise ratio (SNR) as the EBEX cameras that motivated the experiment. However, they required a much larger field of view (FOV) and higher image cadence in order to track turbulence dynamics as they evolve and move across the sky. In this chapter I will explain the design and development process of our camera systems.

4.1 Field of View

We used wide FOVs to capture the context of features and narrow FOVs to investigate small-scale dynamics. While EBEX captured images of PMCs with spatial resolution that could resolve the inner scale of turbulence, the small extent of the EBEX FOV did not allow us to follow individual dynamics as they moved.

EBEX flew 200mm F/1.8 lenses with 9 micron pixels. This configuration gave EBEX a resolution of 9.3 arcseconds/pixel and a smaller FOV of 4.0° x 2.6°. While the aperture could open to F/1.8, the experiment used a F/3 aperture setting for the whole flight.

We designed PMC Turbo with both 50mm F/1.24 wide-field lenses and 135mm F/2 narrow-field lenses. The narrow-field lenses achieved a resolution of 11.3 arcseconds/pixel. We were willing to sacrifice some spatial resolution compared to EBEX for the wider narrow-field FOV of 10° x 15°. Additionally, our budget prevented us from flying the EBEX lenses. The EBEX lenses were no longer commercially available when we designed PMC Turbo and cost too much on the secondary market. The wide-field lenses captured a much larger 27° x 40° FOV with a lower spatial resolution of 30.5 arcseconds/pixel.

When projected from the gondola at 38 km altitude to the PMC layer at 83 km, the wide-field

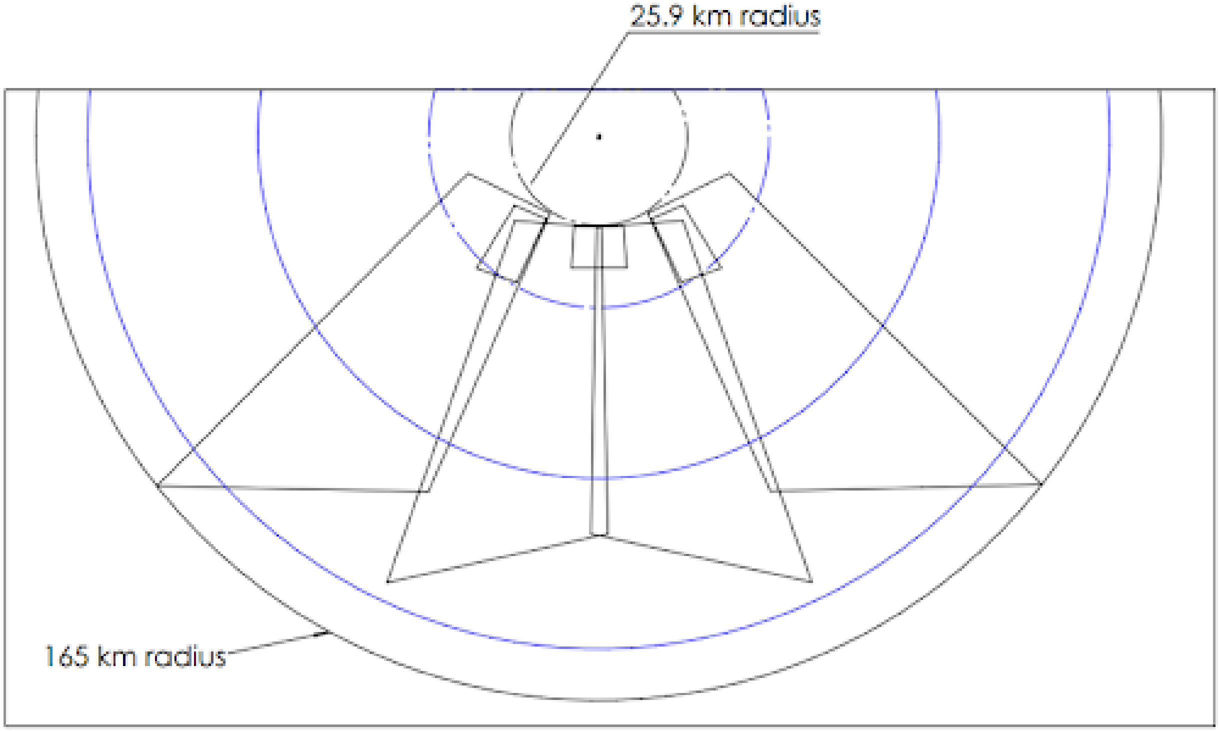

(a) Planned projected FOV

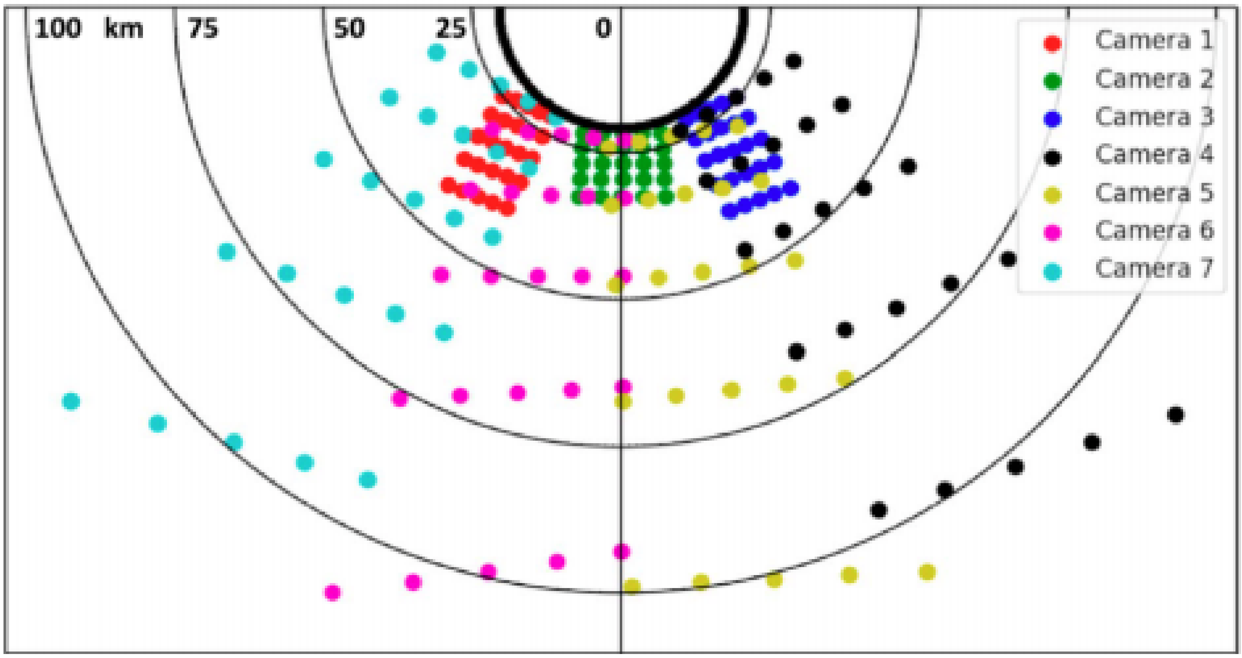

(b) Measured projected PMC Turbo field of view image has an 8 meter per pixel resolution at the zenith edge of the image (25° off-zenith). The resolution increases with off-zenith angle to 18 meter per pixel resolution at 65° off zenith. The narrow-field lenses had a projected resolution of 3 meters per pixel at the zenith edge. Since the narrow-field FOVs were much smaller, the spatial resolution varied less across the image. For comparison, EBEX had a projected resolution of 2.5 meters per pixel.

Table 4.1 shows a comparison of resolution and FOVs across instruments. Comparing the FOVs on the PMC plane is not straightforward due to the variety in viewing procedures. Neither balloon and ground imagers view PMCs directly from below. Balloon imagers must avoid looking at the balloon directly overhead while ground instruments must be located suitably far away from the North or South pole to reduce background sky brightness during the PMC season. This means they also view with some off-zenith angle towards the PMCs over the pole. When observing the PMC plane from below, whether from the ground or from a balloon, the FOV traced on the PMC plane and the resolution per pixel depends heavily on the viewing angle in addition to the camera characteristics. The spatial resolution projected onto the PMC plane scales as $1/\cos\theta$ where θ is the off-zenith angle. As a result, spatial resolution varies significantly across a FOV that covers a large range of off-zenith angles. In Table 4.1 I compare the resolution at small off-zenith angles for instruments that view from below.

The CIPS instrument aboard a satellite captures images from orbit, but moves rapidly relative to the Earth's surface. It stitches together a composite image from data captured during the 15 minutes when the satellite moves over one of the poles. Generally speaking, the narrow-field cameras observing the PMC layer record useful data on scales of tens of km, wide-field cameras on scales of hundreds of km, and CIPS records on scales of thousands of km.

We positioned the wide FOVs side-by-side to create a large composite FOV. We found that if we pointed each camera FOV aligned with the horizon, the lower edges of the wide-field cameras would diverge at large off-zenith angles and we would have gaps in our composite field of view. To avoid such gaps, we introduced roll to our camera mounts to increase the amount of overlap at large off-zenith angles. Figure 4.1a shows the planned composite FOV of all cameras projected

Instrument	Field of View	Pixel area on the PMC plane
PMC Turbo	27° x 40° (wide) 10° x 15° (narrow)	8.2 m increasing with off-zenith angle (wide) 3.0 m (narrow)
EBEX	4.0° x 2.6°	2.5 m
CIPS	80° x 120°	1 km x 2 km (rectangular) [14]
Ground-based cameras	130° x 85° (wide) 9.5° x 6.3° (narrow)	10 m increasing with off-zenith angle [9]

Table 4.1: Comparison of field of view and pixel area on the plane of PMCs between instruments

from the gondola at float onto the plane of the PMCs.

As noted, despite obtaining the best spatial resolution at small off-zenith angles, we needed to avoid viewing the balloon directly overhead. It scattered a great deal of light and would overexpose and introduce background noise into regions of our image. We positioned our narrow-field cameras at the smallest off-zenith angle possible and at the overlap between the wide FOVs to ensure we capture the context, evolution, and movement of any dynamics that pass through the narrow FOVs.

Figure 4.1b shows the actual field of view we achieved, measured using pointing from stars in images. I describe the process we use to find pointing in section 6.2. These measurements have been projected onto the plane of the PMCs at 83 km altitude, while our gondola floated at 38 km altitude. Cameras 1-3 are narrow-field while cameras 4-7 are wide-field. Each camera has been represented by a grid of points corresponding to pixels evenly spaced on the camera CCDs - the edges, 1/4 across the image, 1/2 across the image, and 3/4 across the image. The grid FOV representation shows the distortion of our rectangular FOVs when projected onto the PMC plane. While we record rectangular images on our CCDs, we developed software to correct these data by projecting these data with the true morphology and size of imaged dynamics. I describe this process in section 6.2.2.

The top center point in Figure 4.1b labeled "0" represents the point directly above our gondola on the PMC plane. The line extending vertically downwards from "0" corresponds to the anti-sun direction. Semicircles of increasing radii are drawn at 25 km increments. The bold semicircle just short of 25 km represents the maximum extent of the off-zenith angle traced by the balloon. As one can see comparing Figures 4.1a and 4.1b, we reduced the minimum off-zenith angle required by our balloon between our initial plans and the final pointing of our cameras. During our planning, we changed our choice of balloon due to logistical considerations. The new balloon blocked less of the sky directly overhead, so we took advantage of the smaller off-zenith angles available. The basic plan for our composite FOV changed little aside from this decrease in off-zenith angle.

4.2 Camera details

Our choice of camera was constrained by the need for a well-depth comparable to EBEX, pixel size that would allow for similar resolution as EBEX, and a software-hardware interface that allowed for remote control. To meet our budget, we needed commercially available cameras and lenses. The Kodak 16070 charge-coupled device (CCD) was the only commercially available sensor that matched our requirements.

The Kodak 16070 CCD image sensors have 3232 x 4864 pixels with a well depth of 40,000 electrons, a 7.4 micron pixel size, and a quantum efficiency of 20-35% in the probed wavelengths. We used Allied Vision Prosilica GT 4907 cameras that included this CCD because they utilized a software development kit that allowed us to write software to control the camera hardware. We communicate with the cameras via an Ethernet cable, using a standard GigE Vision link, which connects the camera to the pressure vessel computer. Our software, described in Chapter 5, controls the aperture, focus, and exposure through this interface.

We planned to fine-tune focus, aperture, and exposure to adapt to live sky conditions during flight. While we planned to keep the lens focus at infinity and the aperture fully open, we wanted the capability to adjust the focus since we observed small thermal changes in the focus in our testing. The lens focus control defaulted to zero focus upon power up, and we also wanted to verify that our initialization procedures worked each startup. While we anticipated leaving the aperture open, we also knew that a fully-opened aperture increased vignetting and required precise focus adjustment, so we anticipated reducing the aperture opening if we observed a high SNR. We also wanted to adjust exposure time, since we expected a range of sky brightness during flight.

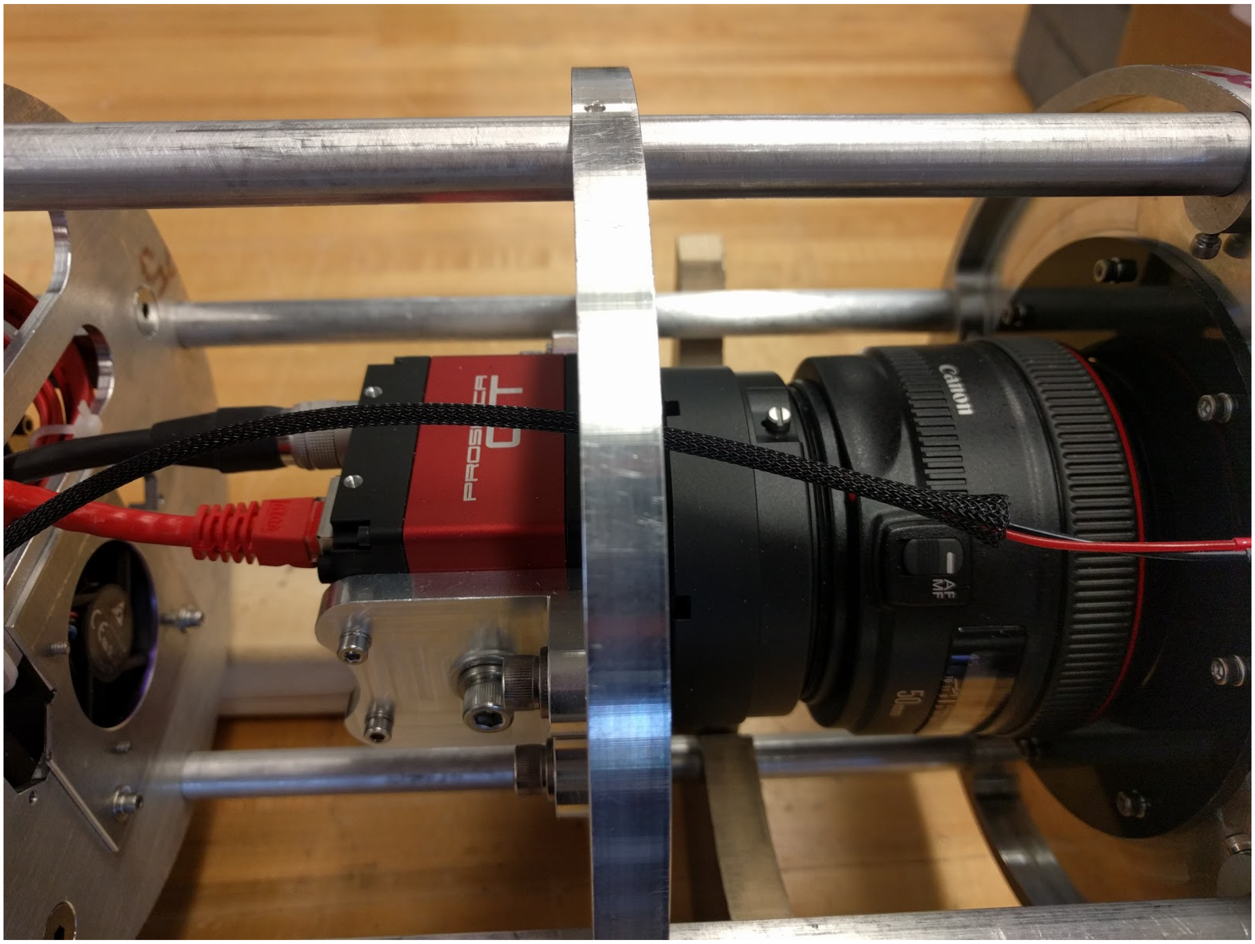

Figure 4.2: Allied Vision camera mounted in the pressure vessel frame

We mounted a Hoya #25A 600 nm filter in front of each lens to improve the SNR of features traced in PMCs. The filter suppresses blue scattered light from the residual atmosphere, thereby attenuating the white light from PMCs less than the background sky brightness. Figure 4.2 shows a closeup of one of our cameras mounted in the pressure vessel frame. Figure 3.6 shows the arrangement of the cameras, lenses, sensors, and computer hardware of the pressure vessels.

We bolted simple baffles to the lens side of the pressure vessels to block stray light from outside the camera FOV. We used aluminum tubes of the same diameter as the pressure vessels painted white on the exterior to reduce heating and black on the interior to reduce reflections into the lens. The baffles are visible on the lens-side of the pressure vessels in Figures 3.4 and 3.5.

4.2.1 Burst exposure

Our cameras included a function allowing for a "burst" of several exposures in quick succession. When we arm the camera using our software interface (described in section 5.2), the camera starts a "burst" at the next whole second. It exposes the CCD for a configurable time (with a minimum exposure time of 35 microseconds), then waits a configurable time, exposes again for the same time, and repeats.The images will be synchronous to a precision about about 1 ms - on the order of 1% of a typical exposure time. This process is shown in Figure 4.3. We utilized this functionality in order to minimize motion blur as described in section 4.9.2.

4.2.2 Bottlenecks

When an image is recorded by the camera, the data from the CCDs is temporarily stored to a buffer within the camera, where it is then sent to the camera computer over gigabit ethernet. The Pipeline software (see section 5.2) running on the camera computer receives the image and writes the data to one of the four data disks situated in the same pressure vessel.

Gigabit ethernet limits the sustained image capture rate to about 3.5 images per second, while the camera buffer can only capture 7.8 images per second. While we can capture short bursts at the higher cadence, if we maintain the maximum capture rate for more than a few seconds the ethernet

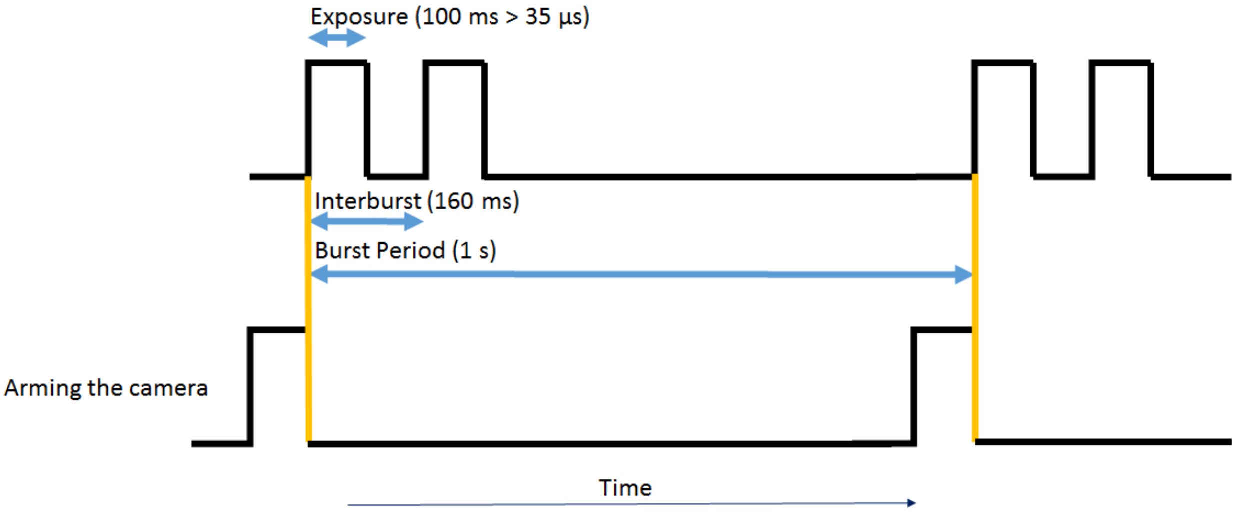

Figure 4.3: Diagram of the image capture process

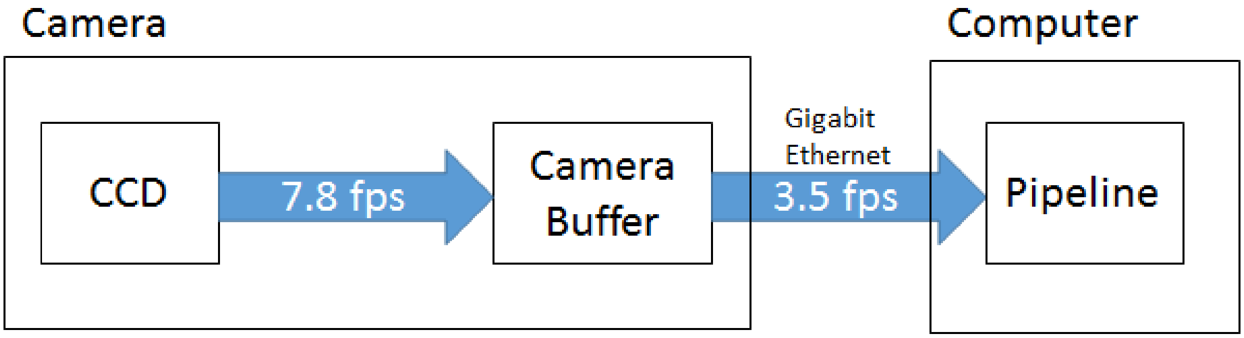

Figure 4.4: Bottleneck overview from CCD to Pipeline

will not keep up and we will overwrite buffers.

These bottlenecks are outlined in the Table 4.2 and all bottlenecks are shown in Figure 4.4. While not met due to the limited duration of the flight compared to the Antarctica design, there is also a limit to the sustained images per second stored to disk set by the disk capacity of each pressure vessel. The frame rate is also limited by the image exposure duration. For example, it is not possible to capture more than 3 images per second (accounting for the 60 ms recording time) at 300 ms exposure.

To track features and analyze their evolution, we only needed about one image every 10 seconds, so our bottlenecks did not threaten our ability to meet our science objectives. However, we hoped to assess the utility of burst capture modes to improve our signal. Since we flew from the Arctic, we had little risk of filling our hard drives prematurely, so we captured bursts of 4 images every 2 seconds.

4.3 Signal-to-noise ratio expectations compared to EBEX

The most important consideration when designing the camera system was observing PMCs with sufficient SNR to achieve our science objectives. The signal (light scattered off PMCs) varied due to the altitude, temperature, latitude, and weather, while the background noise (the background sky brightness) changed throughout the day. The cloud signal rides on top of a large ‘background’ sky brightness. The signal is much smaller than the background, so the noise will be dominated by Poisson noise of the background light. Therefore,

$$SNR \approx \frac{S}{\sqrt{B}} \tag{4.1}$$

where S is the cloud signal and B is the background brightness.

The amount of signal versus background was not constant and difficult to determine from first principles. We knew EBEX captured images with sufficient SNR to identify and analyze features, so we used EBEX sensitivity as a baseline.

Rate	**Definition**	**Max FPS**	**Limiting Factor**
Sustainable rate to save images to disk	Average images/s we can sustain for the whole flight without running out of disk space (assuming no compression at all and a 7 day flight)	3.4 fps	Disk space
Rate of image acquisition for second time scales	Frame rate we can achieve for short bursts of time (assuming sufficiently short exposure times)	7.8 fps	Camera buffer
Rate of image acquisition for minute time scales	Frame rate we could sustain if we had infinite storage on disks (assuming sufficiently short exposure times)	3.5 fps	Gigabit ethernet

Table 4.2: Image acquisition rate descriptions

In order to quantify this process, we used the ratio R of the SNR we expect for PMC Turbo to the SNR we measured with the EBEX cameras:

$$R = \frac{SNR_{PMCT}}{SNR_{EBEX}} \tag{4.2}$$

I define R to be the product of ratios accounting for differences in exposure time, hardware, and sky conditions between PMC Turbo and EBEX.

Since we can adjust the exposure time of our cameras, but not the hardware or sky conditions, it is convenient to split R while comparing the EBEX and PMC Turbo sensitivity into two factors. R_{int} is the ratio in PMC Turbo and EBEX SNR due to differences in exposure time. R_0 is the ratio in PMC Turbo and EBEX SNR due to everything else.

$$R = R_{int} R_0 \tag{4.3}$$

R_{int} is straightforward to calculate. The brightness of both the clouds and the sky background change slowly compared to reasonable exposure times of hundreds of milliseconds. Therefore, the photon flux accounting for both S and B is constant, both will scale linearly with exposure time, and our SNR scales with the square root of exposure time. Therefore, the contribution to R from exposure time difference between EBEX and PMC Turbo will be:

$$R_{int} = \sqrt{\frac{t_{int,PMCT}}{t_{int,EBEX}}} \tag{4.4}$$

However, we cannot indefinitely increase exposure time to increase SNR. Motion blur would reduce our resolution and our sensors would become overexposed.

R_0 is more complicated. The cloud signal for PMC Turbo scales with our ratio of our camera hardware sensitivity to that of EBEX R_{camera}, ratio of cloud brightness due the apparent thickness of the PMCs for PMC Turbo and EBEX $R_{thickness}$, and the ratio of cloud brightness of the PMCs due to latitude $R_{latitude}$. Therefore we find:

$$S_{PMCT} = R_{camera} R_{thickness} R_{latitude} S_{EBEX} \tag{4.5}$$

The background for PMC Turbo also scales with R_{camera}, ratio of sky background brightness between PMC Turbo and EBEX due to the different altitudes at which the experiments fly $R_{altitude}$, and the ratio of sky brightness background brightness due to difference in elevation angle of the cameras $R_{elevation}$:

$$B_{PMCT} = R_{camera} R_{altitude} R_{elevation} B_{EBEX} \tag{4.6}$$

Therefore, we can compute our expected SNR in terms of the EBEX SNR:

$$SNR_{PMC} = \frac{R_{thickness}R_{camera}R_{latitude}S_{EBEX}}{\sqrt{R_{camera}R_{altitude}R_{elevation}B_{EBEX}}} \tag{4.7}$$

and we find R_0:

$$R_0 = \frac{R_{thickness}R_{camera}R_{latitude}}{\sqrt{R_{camera}R_{altitude}R_{elevation}}} \tag{4.8}$$

In order to verify that our cameras would capture data with sufficient SNR to achieve our science objectives we needed to quantify R_0 and determine possible exposure times to quantify R_{int}. To achieve these tasks we:

- Compared the sensitivity of our camera hardware to the EBEX camera hardware.
- Determined the constraints on our exposure time by motion blur and sky brightness.
- Anticipated the difference in signal and background due to different flight plans and viewing angles.

We acknowledged the large variability of sky conditions and the small sample size of PMC balloon imaging. Before the summer of 2018 the only published balloon-borne observations of PMCs came from EBEX. While we wanted to develop the best plan possible, PMC Turbo would be the first experiment of its kind, so we built a robust telemetry system and adjustable imaging system to monitor and adapt to live observations. I describe the software we built to control the cameras in Chapter 5. While we anticipated adjusting to sky conditions during flight, we wanted to estimate SNR so we could develop an exposure plan before flight.

4.4 Comparison of camera sensitivity

To find R_{camera} we needed to quantify the difference between EBEX and PMC Turbo hardware sensitivity. Our sensitivity scales with the photon flux on each pixel and scales with the quantum efficiency of the CCD. Thus the signal scales with the solid angle of each pixel (proportional to the pixel area A_{pixel} divided by the focal length f of the lens) times aperture area $A_{aperture}$ times quantum efficiency Q. Since I will calculate ratios between all these values, I neglect constants.

$$S \sim \Omega \sim \frac{A_{pixel}}{f^2} \tag{4.9}$$

$$S \sim A_{aperture} \tag{4.10}$$

$$S \sim Q \tag{4.11}$$

Due to industry standards for lenses, it is convenient to use the f-stop (written as F/# and defined as focal length divided by aperture diameter) in place of the focal length and aperture area. Note that by this definition

$$fstop^2 \propto \frac{f^2}{A_{aperture}} \tag{4.12}$$

Therefore, the contribution to R_0 from the relative sensitivity of the PMC Turbo hardware is

$$R_{camera} = \frac{\frac{Q_{PMCT} A_{pixel,PMCT}}{fstop^2_{PMCT}}}{\frac{Q_{EBEX} A_{pixel,EBEX}}{fstop^2_{EBEX}}} \tag{4.13}$$

The pixel area and lens characteristics for PMC-Turbo and EBEX are listed in Table 4.3.

Both EBEX and PMC-Turbo used a red filter, which is close to a step function at 600 nm. Above this cutoff, the ratio of $Q_{PMC-Turbo}$ to Q_{EBEX} is close to 1:2. Figures 4.5 and 4.6 show the manufacturer-provided quantum efficiency in the visible spectrum.

R_{camera} for each camera is noted in the last column of Table 4.3. Our wide-field cameras, with a small f-stop, were much more sensitive than the EBEX cameras, while our narrow-field cameras were not. While we planned to set the apertures of our narrow-field lenses to a more dilated f-stop than EBEX, the lower quantum efficiency and smaller pixel size of our CCD reduced our

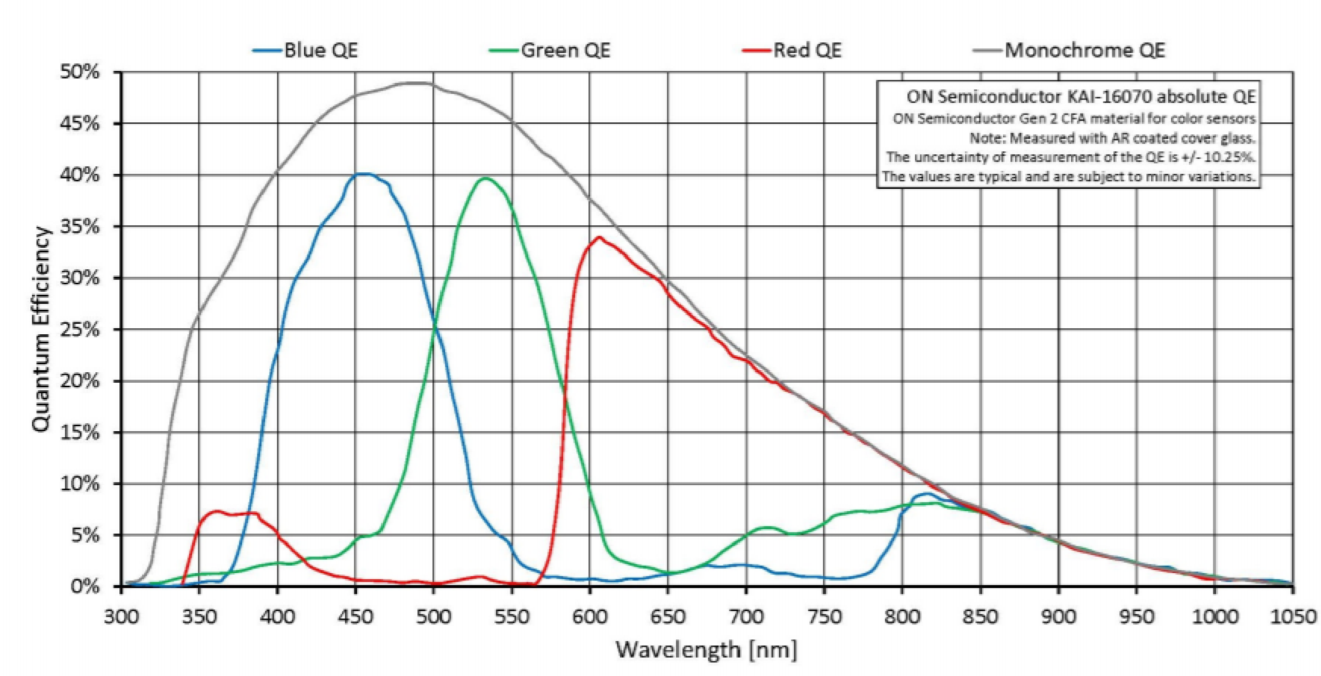

Figure 4.5: Quantum Efficiency of PMC-Turbo CCD from camera spec sheet.

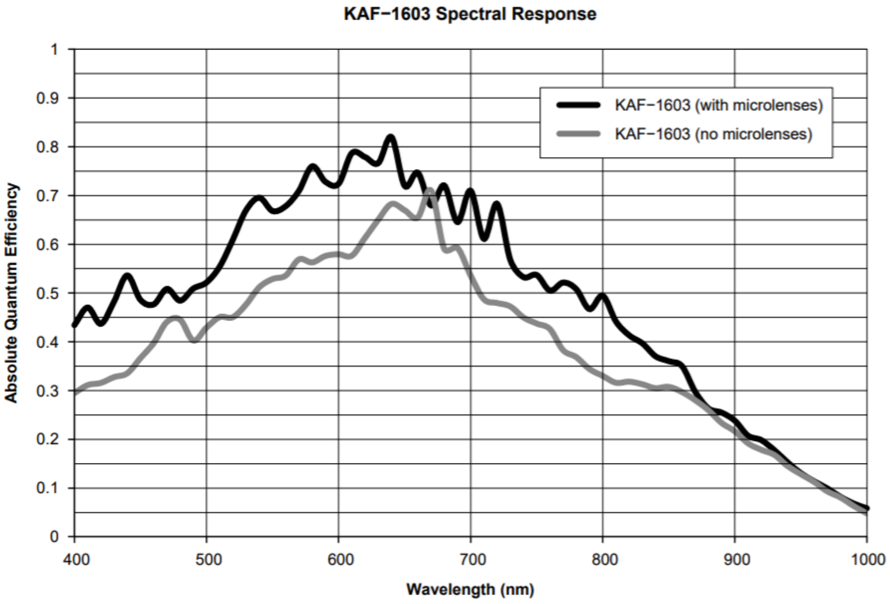

Figure 7. Typical Spectral Response

Figure 4.6: CCD quantum efficiency of EBEX star cameras from CCD spec sheet.

Camera	fstop	Average QE	A_{pixel} (μm^2)	R_{camera}
EBEX	f/3	0.40	81	1
Narrow FOV	f/2	0.20	55	0.76
Wide FOV	f/1.24	0.20	55	1.98

Table 4.3: The camera and lens characteristics for EBEX, the narrow field of view, and the wide field of view cameras.

sensitivity compared to EBEX.

4.5 Exposure constraints from sky brightness

We needed to characterize the sky brightness background both to estimate our SNR and to constrain exposure time. The sky brightness depends on imager elevation (the angle the imager makes with the horizon), sun elevation, and balloon altitude. I used Modtran sky brightness simulations originally used for EBEX to predict how sky brightness would change. I then used measurements of sky brightness taken by EBEX and scaled them using the model results for viewing angle and the relative sensitivity of the cameras. We used EBEX as a baseline and compared the background we expected in terms of a ratio $R_{background}$ between the PMC Turbo and EBEX cameras. We defined the ratio $R_{background}$ to be:

$$R_{background} = R_{camera} R_{altitude} R_{elevation} \tag{4.14}$$

4.5.1 Sky brightness as a function of imager elevation angle

Figure 4.7 shows the the sky brightness as a function of telescope elevation, sun elevation, and the difference between sun and telescope azimuth. This data comes from simulations run for background estimates for the EBEX star cameras. In this plot the baseline has been defined to be 1) elevation of 50° and 2) 100° difference between sun and telescope azimuth. The other data points show the scaling relative to that baseline.

The shapes of the points on the scatter plot show the model results for different azimuth point-

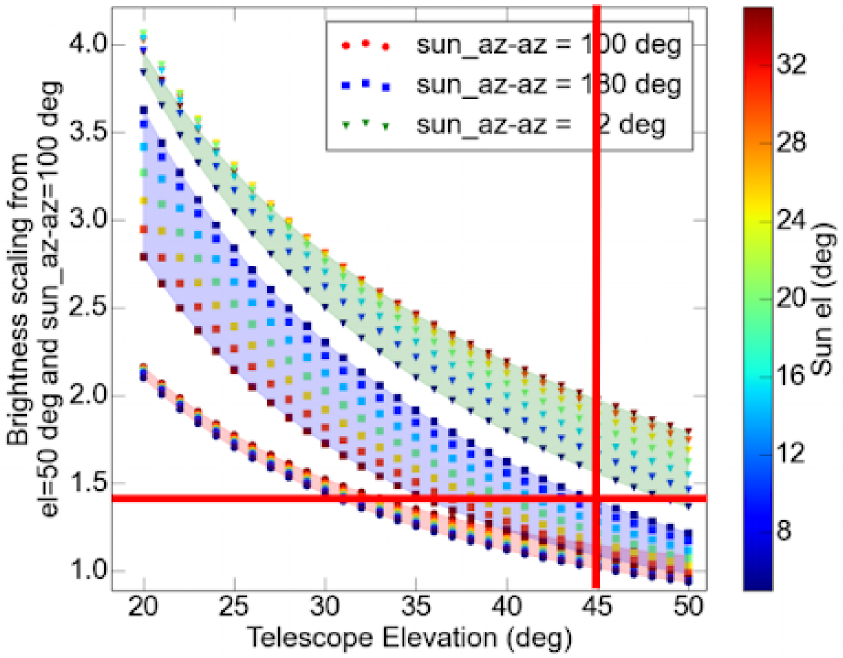

Figure 4.7: Relative sky brightness versus telescope elevation for three pointing cases

ing. The square shows anti-sun pointing (180° azimuth difference), the circle shows 100° azimuth difference, and the triangle shows pointing just slightly off from the sun (2° azimuth difference). We knew the PMC Turbo cameras would point anti-sun, although our wide field cameras would extend in azimuth some 50° to either side of anti-sun. Exactly anti-sun would be the brightest sky condition we expected to observe, so we were most interested in the anti-sun (square-labelled) data.

The sky brightness changes with sun elevation, so we expected a range of sky brightness observations for each case of azimuth pointing. The color of the markers notes the sun elevation at each point. The shading behind the points notes the trend of each azimuth difference brightness versus telescope elevation for a range of sun elevations noted in the right sidebar. While balloon experiments fly near enough to the pole that the sun does not set, it will change position in the sky over the day resulting in changing sky brightness. For simplicity, we estimated the brightest skies measured by EBEX compared to the brightest skies we anticipated for PMC Turbo.

The red lines on Figure 4.7 note the telescope elevation and brightest sun elevation for EBEX.

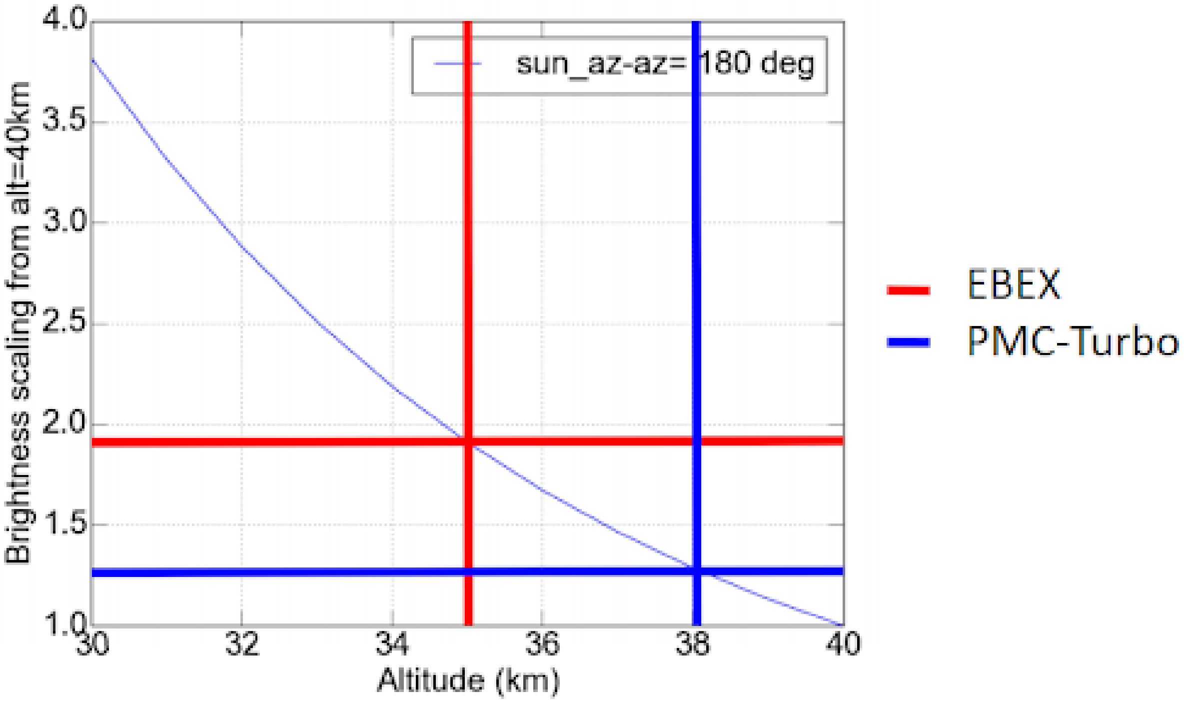

Figure 4.8: Relative sky brightness versus balloon altitude

We compared our plans for telescope pointing to this reference point. We ran this analysis before deciding on the precise orientation of our lenses and we used significantly larger FOVs than EBEX, so we looked at a range of elevation angles to compare to the EBEX baseline: about 50° to 35° for the wide-field cameras and 50° to 40° for the narrow-field cameras. We used a narrower range of elevation angles for the wide-field lenses since we prioritized higher resolution data from smaller off-zenith (higher elevation) angles.

From this range of PMC Turbo elevation angles we expected a sky brightness scaling of 0.9 to 1.4 for the wide field of view cameras, and a scaling of 0.9 to 1.25 for the narrow field of view cameras, both compared to the EBEX brightness scaling baseline marked with red lines.

4.5.2 Sky brightness as a function of balloon altitude

The sky brightness also varies with altitude. We expected to fly higher than EBEX, so we estimated the change in sky brightness due to our predicted balloon altitude. Figure 4.8 shows the change in sky brightness with altitude assuming anti-sun pointing, compared to a baseline of the

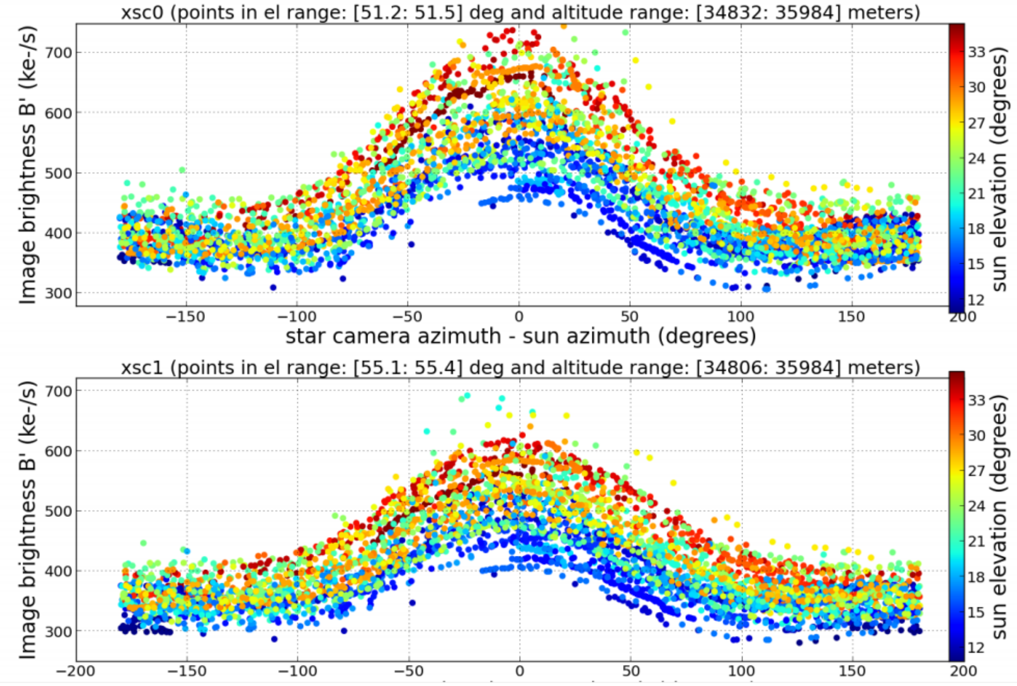

Figure 4.9: Measured EBEX sky brightness

sky brightness at 40 km. The red lines mark the 35 km EBEX balloon altitude, while the blue line marks the 38 km PMC Turbo balloon altitude. we expected PMC Turbo to measure 0.66 of the sky brightness compared to EBEX due to the higher altitude.

4.5.3 EBEX sky brightness measurements and PMC Turbo predictions

We used the EBEX measurements of sky brightness to scale the photon flux according to our predictions of telescope elevation and altitude. Figure 4.9 shows the sky brightness observed by EBEX as a function of sun elevation angle and star camera azimuth minus sun azimuth, scaled to F/1.8 f-stop. While the EBEX cameras were set at F/3 for the duration of flight, these measurements were scaled to F/1.8 because the apertures had the capability of opening to F/1.8.

When we took a maximum sky brightness of 500 ke-/s measured by EBEX and account for our expectations for hardware differences, elevation, and altitude, we predicted maximum sky brightness of 110 ke-/s for the narrow field of view cameras, and 330 ke-/s for the wide field of view cameras. In order to avoid filling our 40 ke- wells, individual image integration times could

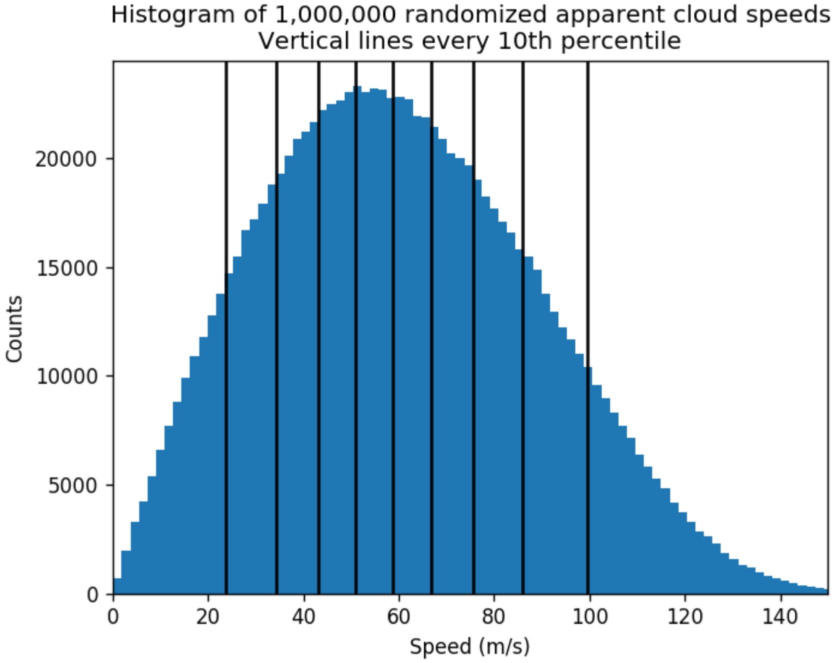

Figure 4.10: Apparent motion model (gondola and cloud motion)

not exceed 400 ms and 135 ms, for narrow and wide lenses respectively, in the high-brightness case.

4.6 Exposure constraints from motion blur

During flight, we wanted as long exposure times as possible to maximize SNR. However, we also wanted to avoid motion blur from the relative motion of the PMC field due to the motion of the camera platform and the bulk advection of the clouds themselves.

A NASA-supplied rotator controlled the orientation of our payload. It kept the cameras pointed anti-Sun in the azimuth direction to keep sunlight out of our imagers and incident to our solar panels. The NASA rotator technicians predicted azimuth oscillations with amplitude of 1° and a period of 42 s. From previous observations, including EBEX, DeepWAVE, and ground based experiments, we expected 50 ± 20 m/s bulk velocity of the PMCs due to background winds.

We used these motion predictions to construct a model taking into account motion from both the clouds and our gondola. We assumed a Gaussian distribution of bulk cloud motion according to our predictions and we matched them with motion taken at random points in the 42 second oscillation. We then ran the model a sufficient number of times to allow for statistically significant results. Figure 4.10 shows the output of the motion blur model with one million samples.

The narrow-field cameras had a spatial resolution of 3 m per pixel while the wide-field cameras had a spatial resolution of 8 m per pixel. Using the model presented, we expected <1 pixel motion-blur with the narrow-field lenses for every 100 ms exposure time 16% of the time and <1 pixel of motion blur with the wide-field lenses for every 100 ms of exposure time 75% of the time. I describe how we developed our exposure time after we had calculated the expected SNR in section 4.9. I describe the motion blur we measured in flight in appendix B.3.

4.7 Signal expectations

4.7.1 Cloud cross-section difference due to viewing angle

EBEX and PMC Turbo viewed PMCs at different angles, and we expected differences due to different cloud cross-sections viewed by each camera. Since the PMC layer is not dense, we assumed that the backscattered light from clouds scales linearly with the depth of the cloud layer. As the off-zenith angle of a camera viewing the PMC layer increases, the cross-section of the cloud layer viewed by that camera will increase, and the light scattered by those clouds will increase.

Since we had no measurements of the vertical structure of PMCs viewed by EBEX, we assumed the cloud layer had the same vertical thickness for PMC-Turbo and EBEX. EBEX included two star cameras mounted at different angles, and we used the camera that viewed the sky at an off-zenith angle of 39.5° for calibration. For reference, the PMC Turbo cameras pointed over much larger FOVs (see table 4.1), but the top edge was only 25° off-zenith. We needed to scale the expected signal by a term $R_{thickness}$:

$$R_{thickness} = \frac{t_{pmc}}{\cos\theta_{PMCT}} \frac{\cos\theta_{EBEX}}{t_{pmc}} = \frac{\cos\theta_{EBEX}}{\cos\theta_{PMCT}} \tag{4.15}$$

where t_{pmc} is the thickness of the PMC layer, and θ is the elevation angle of each imager.

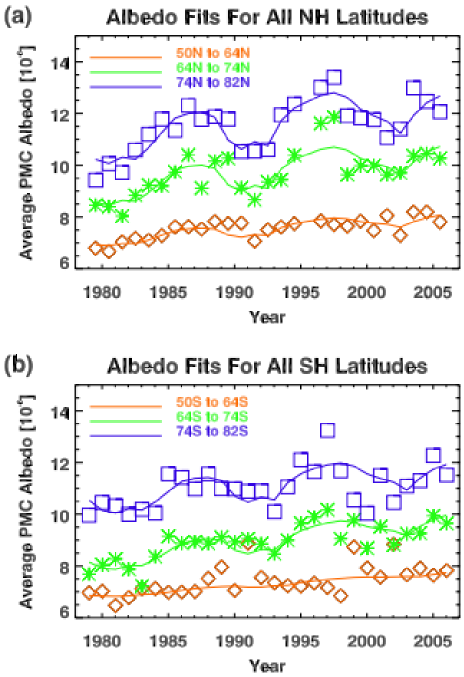

Figure 4.11: Seasonal PMC albedo fits

4.7.2 Brightness variations in PMCs by latitude

PMC Turbo would fly in the Artic, which meant it would reach a less polar latitude than EBEX did. PMCs are brighter closer to the poles. We accounted for this difference in brightness with a scaling term $R_{latitude}$, defined as the ratio of brightness of the PMCs at the PMC Turbo flight latitude to the brightness of the PMCs at the EBEX flight latitude. We found Deland et al. [19] described the seasonal average PMC albedo for Northern and Southern hemispheres. Figure 4.11 shows these results.

EBEX flew close to the center of the 74S to 82S band, while we expected PMC-Turbo to fly close to the center of the 64N to 74N band. Therefore, we used the previous measurements to estimate $R_{latitude} = 0.86$

4.8 SNR Expectations

Since R_0 depends on viewing angle, it will vary across our FOVs. However, due to competing effects of PMC layer thickness and path length through the atmosphere, R_0 varies by less than a percent in the narrow field of view and by only 4% in the interesting region of the wide field of view. We find for the narrow and wide lenses that R_0 is:

$$R_{0,Narrow} \simeq 0.83 \tag{4.16}$$

$$R_{0,Wide} \simeq 1.35 \tag{4.17}$$

4.9 Exposure plans

4.9.1 Constraints

Both our signal and background scale linearly with the exposure time t as $\sqrt{t}$ so the exposure time required for the same SNR as EBEX is

$$t = \frac{300ms}{R_0^2} \tag{4.18}$$

Using the $R_{0,Narrow}$ and $R_{0,Wide}$ calculated in the previous section , we find that to achieve the same SNR as EBEX, during bright (high noise) but expected conditions, PMC-Turbo would need to integrate for 435 ms for narrow field of view images, and 165 ms in the wide field of view case.

In the same bright but expected conditions, sky brightness constrained our exposure times to 400 ms and 135 ms. Therefore, neither of the cameras could attain the same SNR as EBEX, although they could come close. With 135 ms exposure times, the wide-field cameras would attain a SNR ratio R of

$$R = R_{0,Wide}R_{int} = 1.35\sqrt{135ms/300ms} = 0.91 \tag{4.19}$$

compared to EBEX. The narrow field cameras would attain a SNR ratio R compared to EBEX of

$$R = R_{0,Narrow}R_{int} = 0.83\sqrt{400ms/300ms} = 0.96 \tag{4.20}$$

Furthermore, our motion blur models put soft constraints on our exposure time. We used the model described in section 4.6 to predict the percentage of observations we will obtain with one pixel or less of motion blur.

With the 400 ms exposure required for the narrow-field lenses we would need less than $\frac{3m/pixel}{400ms} = 7.5m/s$ apparent motion to measure one pixel or less of motion blur. We expect this apparent motion less than 5% of the time.

We find much more favorable conditions for the wide-field cameras given their higher sensitivity and larger spatial resolution. We need less than $\frac{8m/pixel}{135ms} = 60m/s$ apparent motion to measure one pixel or less of motion blur. Again using the apparent motion model, we expect this motion about 50% of the time.

4.9.2 Solutions

We expected the constraints on exposure time from sky brightness and motion blur to prevent us from attaining the same SNR as EBEX in a single exposure. Furthermore, the constraints placed on our exposure plan pulled us in two directions; we wanted to increase exposure time to increase SNR, but reduce exposure time to reduce motion blur. We needed to find a compromise that allowed us to achieve our science objectives.

While we could not use CCDs with larger well depths or lenses with higher sensitivity, we selected cameras with burst capture capabilities. The Allied Vision camera modules can capture 7.8 frames per second in short bursts (section 4.4 provides a detailed description of the image cadence bottlenecks). Our exposure plan included capturing bursts of four images every 2 seconds. We planned to track motion between frames using feature-tracking software such as TrackPy and co-add the images together if we needed a higher SNR. This would effectively increase our exposure time while avoiding overexposure or motion blur. The buoyancy period of the dynamics was around 10 seconds, so co-adding images captured over 1-2 seconds would not reduce our ability to achieve our science objectives.

Another option to increase SNR was binning pixels. As noted in section 4.4, camera sensitivity scales with pixel area. Both signal and noise scale with pixel area, so SNR scales with $\sqrt{A_{pixel}}$. If we bin a NxN square of pixels, we increase effective pixel area by N^2 and SNR by N. This reduces our spatial resolution by the same factor. However the inner scale of turbulence at the PMC altitude is 20 m - larger than either our narrow-field 3 m pixels or our wide-field 8 m pixels. Many dynamics we expected to analyze had much larger scales than the 20 m inner scale of turbulence [54] [9].

One advantage of co-adding burst images or binning pixels was that we could do either during post-flight analysis. Motion blur could not be removed after the flight. On the other hand, our primary concern during flight was capturing identifiable images of PMCs. Using a fixed exposure time to capture motion blur risked both overexposure and capturing insufficient SNR, especially in the absence of communication to the ground. We did not have experience co-adding burst images of PMCs since the EBEX experiment had a far lower image cadence of 30 seconds.

The fixed exposure method had potential benefits, but also included more risk, so we elected to prioritize a safer auto-exposure method. We implemented a custom auto-exposure algorithm that checked image statistics and adjusted the camera exposure according to configurable parameters. Notably, we required that only a small percentage of the pixels were overexposed - expected due to stars and a low rate of malfunctioning pixels. We also implemented a configurable hard cap on the exposure to avoid unacceptable motion blur. Auto-exposure still allowed us to bin pixels after the fact, but had the downside of allowing motion blur up to the capped exposure time.

While we prioritized and defaulted to the auto-exposure method, we still captured bursts of images. We allowed the auto-exposure algorithm to select the exposure time and modified the burst cadence to the selected auto-exposure. Once we had used our ground software to confirm that we had captured PMC images with auto-exposure, we would continue using auto-exposure for an hour, after which we would switch to bursts of shorter fixed exposures with lower motion blur and SNR. While we prioritized confirming and downlinking useful PMC images, we wanted to test both exposure methods for future flights.

Figure 4.12: Testing the camera arrangement at Columbia University

For the results of our plan refer to appendix B.2. We monitored the system closely and customized the exposure throughout flight.

4.10 Pressure Vessel testing

After developing the camera systems, we performed tests to simulate flight conditions. Figure 4.12 shows one trial on the roof of Pupin Hall on Columbia campus during twilight. Tests during sunset allowed us to test our camera performance by checking tropospheric cloud signal and star signal across a range of background sky brightness levels.

We tested camera performance at the temperatures we expected to encounter during flight, both at full sea level pressure and in a thermal vacuum chamber. Early tests involved containing

Figure 4.13: Thermal testing the pressure vessel using dry ice

the pressure vessels in a cooler and increasing the temperature with passive heating of the power expenditure of the cameras, or decreasing the temperature by filling the cooler with dry ice (show in Figure 4.13). We tested lenses through a range of thermal conditions to understand the focus drift with changing temperatures.

In addition to communication tests and testing the integrated payload, we tested our pressure vessels at CSBF in a thermal vacuum chamber. This chamber cooled or heated to expected flight temperatures, and then evacuated, allowing us to test hardware in the atmospheric conditions we expected.

We expected that water vapor inside the vessel would condense and freeze as the pressure vessel cooled while ascending through the tropopause. This would block the window to the lens and presented a critical threat to our science objectives. To counteract frost blocking our view, we purged the pressure vessels with nitrogen.

The pressure vessels included pressure and temperature sensors, so we checked for leaks over days, weeks, and months. We pressurized the vessels to 1.3 atmospheres, so the pressure difference between pressure vessels and the sea level air pressure was 0.3 atmospheres. However, at float, the atmosphere can be well-approximated as a vacuum, so the pressure difference would be 1.3 atmospheres. Therefore, we expected much higher leak rates. We found leaks when we sealed the pressure vessels if dust or metal shavings landed on the O-ring on the seal. These slow leaks became apparent within days.

After careful sealing and successful week-long tests, we convinced ourselves of the seals by pressurizing the vessels before shipment from Texas to Sweden. Several months later we found negligible leakage. We also tested the pressure vessels in the thermal vacuum chamber for any unexpected behaviors at low pressures. The pressure vessels remained pressurized through our science flight and arrived pressurized at our lab after recovery and shipment from Northern Canada.

Chapter 5: Software

5.1 Design Requirements

We designed our experiment software with several requirements:

1. The software needed to manage the data throughput from cameras to the hard drives.
2. The software needed to be robust to failure of individual pressure vessels, communication components, or other subsystems.
3. We needed to have the ability to command the payload from the ground, monitor each subsystem through aggregated housekeeping, and sample imager data.

Our data handling requirement drove our selection of computer hardware (described in section 3.4.1) since the large data volume generated by our cameras required a server-grade motherboard to store to disk. We developed software that handled up to 64 MB/s from the camera over short periods and a sustained 32 MB/s to the hard drives.

Once we had selected hardware that could handle our data throughput requirement, we designed our software to meet our requirements for resilience. To reduce the impact of an isolated disk failure, each computer ran software to grab data from the connected camera and distribute the images to the four hard drives within the same pressure vessel.

Since we required powerful computers for data storage, we found no downside to including flight control capabilities in each individual computer, as opposed to the more common design of using a dedicated flight control computer. Our system had no need for a dedicated flight control computer, as any pressure vessel could assume responsibility of the communication between local systems and our telemetry connections. This increased the resilience of our system to single point failures.

Balloon-borne payloads include experimental risks that can result in the loss of collected data. Furthermore, PMC Turbo was the first experiment of its type, so our predictions included a large uncertainty in sky conditions and optimal viewing strategy. To reduce the risk inherent in balloon-borne platforms and to adapt and fine tune our observation strategies in real time, we developed a robust communication system. We continuously monitored our instrument statuses and we downlinked as much data as possible to retain some scientifically useful data in the event our payload could not be recovered. We developed our software to use the telemetry channels made available by NASA to send compressed and packetized science data and housekeeping to the ground. To monitor the data received on the ground, we developed software to track data sent down and send commands to the payload.

While we wanted to monitor and command the payload as much as possible, we needed to account for expected communication outages and the resulting absence of commands. We implemented these procedures to ensure that our camera systems captured and stored images to disk even if we lost contact with them. Our cameras had no real-time control requirements. The operating system uses a Linux program (supervisor) to automatically start the data acquisition and communication software in a useful state and when the pressure vessel receives power, the motherboard automatically boots the operating system. The data acquisition software includes a watchdog that restarts the operating system after 10 minutes without new images. The default camera settings included an auto-exposure algorithm to maintain useful exposure times and a nominal focus sufficient to capture good data.

In this chapter, I discuss the design of the software we wrote. Section 5.2 describes the software we developed to meet our data acquisition requirements. Section 5.3 describes the software we developed to manage communication between subsystems on our balloon-borne platform and between our experiment and the ground monitoring stations. Section 5.5 describes how our software operated during the flight of our experiment. Finally, section 5.6 describes the software structure we used to coordinate across analysis projects.

We wrote the bulk of our software in the Python programming language. This language allows for speedy development and is well-known among scientific programmers. We used continuous integration tools described in section 5.4 to ensure reliable and speedy software development. The software we wrote will be distributed to the scientific community in early 2022 in the SkyWinder package via the NASA supported Python in Heliophysics Community. While I will describe the software at a high level in this chapter, I recommend interested readers to look further at SkyWinder, which will be open-source.

5.2 Data Acquisition

5.2.1 The pipeline

We call the software module responsible for data acquisition "the pipeline". Due to the structure of the Vimba software development kit (SDK) that the camera manufacturer released for our cameras, the pipeline also acts as our interface with the camera hardware. It sends commands to the camera, arms the camera to capture an image, receives the image data, and writes the image to one of the four data disks.

The primary responsibility of the pipeline is moving data from the camera buffers to the hard drives. Upon initialization, the pipeline creates a configurable number of raw image buffers and puts them into an input queue. The pipeline also instantiates an output queue, where the buffers will be moved when filled with image data. The pipeline starts one "AcquireImage" process and several "WriteImage" subprocesses which watch the input and output queues instatiated by the pipeline. The AcquireImage process passes the buffers of the input queue to camera via the SDK. It periodically checks whether these buffers have been filled and it moves them to the output queue once they have been filled. The WriteImage subprocesses periodically check the output queue and write these buffers to disk. The WriteImage subprocesses then move the now empty buffer back to the input queue. The pipeline performs lossless compression on the images when it stores them on the spinning disks using the blosc library [4]. This compression results in roughly 20MB per image file. In the absence of any external commands, the pipeline commands the camera to capture images at a regular interval (see section 4.2.1) and stores those images to disk. The pipeline starts

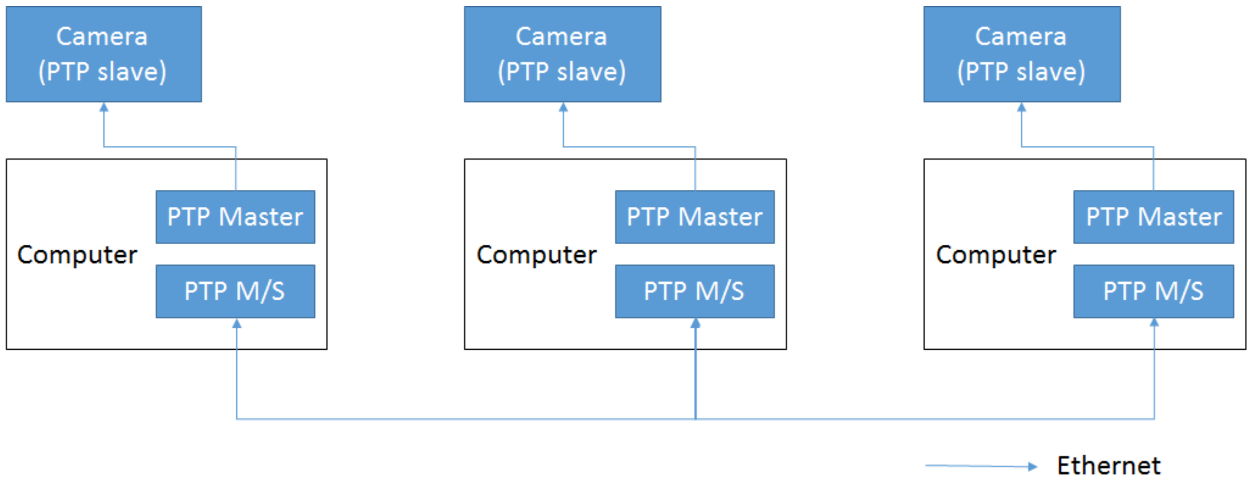

Figure 5.1: Precision Time Protocol synchronization architecture

this process automatically at boot-up.

The pipeline acts as our software-hardware interface with the cameras via the SDK. Allied Vision publishes the Vimba SDK with functionality including image capture, setting parameters for the camera (exposure time) and lens (aperture, focus), and capturing bursts of images. I describe exposure capture modes in section 4.2.1. While the SDK is written in C++, our own software includes a Cython wrapper to allow our Python code to interface with the SDK.

The pipeline instantiates a command queue. When a command is put into that queue by the controller (see section 5.3.4), the pipeline process will execute the command by calling the SDK function that directly command the camera.

5.2.2 Synchronization and Image Capture

We required our computers to be synchronized in time for communication and data collection. As described in section 5.3, our computers communicated between themselves both in routine operation and while communicating with the ground. We needed consistent timestamps for this communication. We also required that our science data be taken synchronously. We anticipated using composite images from several cameras during analysis and we wanted the individual images to be taken at the same time. Since the pipeline interfaces with the camera directly, we required that each instance of the pipeline be synchronized.

The cameras and camera computers use precision time protocol (PTP) called "ptpd2" - the industry standard for clock synchronization. Each camera computer runs a PTP instance configured in master/slave configuration and synchronizes with the other camera computers, and a second PTP instance in a master configuration that synchronizes with the corresponding camera. This architecture is shown in Figure 5.1.

5.3 Communication

Our hardware design consisted of several independent subsystems each capturing data synchronously. While the autonomy of these subsystems increased the robustness of our experiment, our need to remotely command and monitor our experiment required us to develop software for communication both between the individual subsystems aboard our gondola and between the gondola and our ground systems. In this section, I describe the software we implemented.

We use the Python remote object (Pyro4) module to enable communication between software processes. Pyro enables each process to use a Uniform Resource Identifier (URI) on the local network. After registering a URI, one process (such as the controller, described in this section) can call another (such as the pipeline) as a Python object. Not only does this facilitate communication between processes running on one machine, but our network structure allows each registered process to be visible and accessible to the entire network. The system uses this functionality every few seconds when the leader queries other communicators for housekeeping information (see section 5.3.2).

5.3.1 Architecture

Figure 5.2 shows a simplified overview of the software and hardware network. Seven pressure vessels contain the cameras responsible for collecting data used for our primary science objectives. We connect these pressure vessels to our network using two Ethernet switches. The two RS-232 Ethernet converters, two Ethernet switches, and a direct Ethernet connection to Iridium Pilot ensure that no single point of failure removes communication to all the channels. Our telemetry

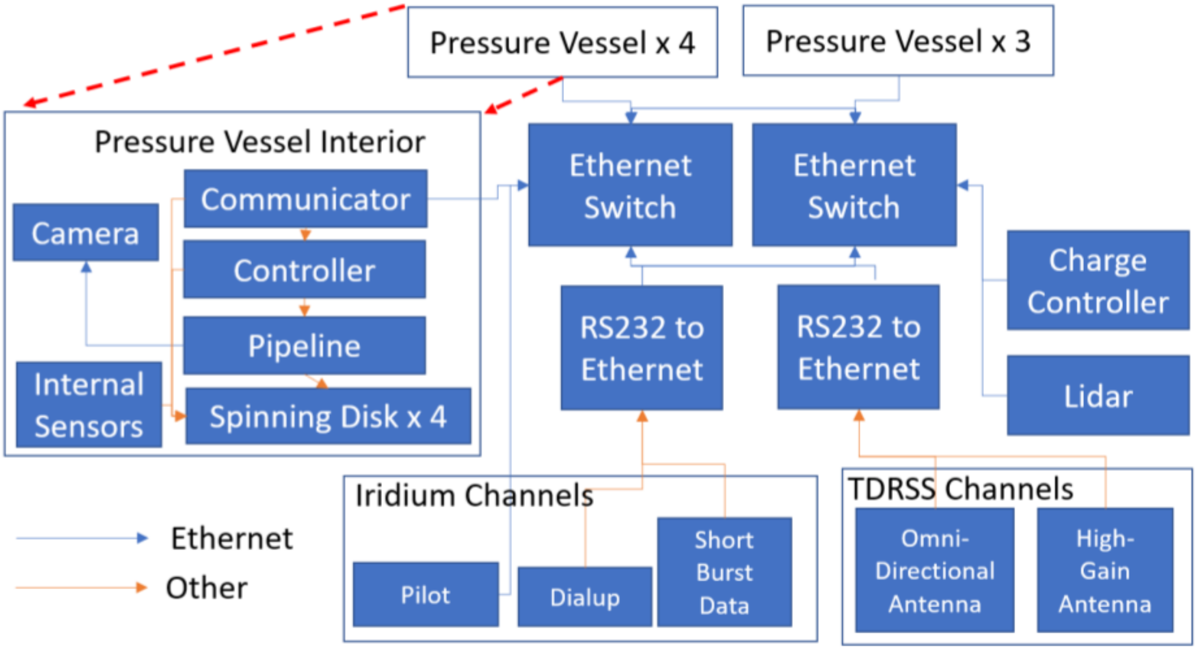

Figure 5.2: Overview of software and payload software architecture and network.

box includes two Ethernet switches connected to each other. Three or four of the pressure vessels, one of the two power boxes, and one RS232-Ethernet converter connect to each Ethernet switch. This ensures that if either Ethernet switch failed or one SIP connection failed, we would not lose communication to the entire payload. We distribute the wide and narrow-field lenses across the two Ethernet switches to avoid losing one category of FOV if an Ethernet switch failed.

The expanded view labelled "Pressure Vessel Interior" in Figure 5.2 shows the primary software processes of our software architecture: the "pipeline", the "controller", and the "communicator" described in this section. The pipeline, described in section 5.2.1, interfaces with the camera and hard drives directly. The communicator (section 5.3.2) is responsible for the communication between subsystems on our gondola - the pressure vessels, the charge controllers, and the lidar, as well as the communication over the telemetry channels. The controller (section 5.3.4) prepares files for the communicator to send to the ground and interprets commands to send to the pipeline.

5.3.2 The Communicator and Leader

The "communicator" software module coordinates between the pressure vessels, and communicates with ground operators. It aggregates housekeeping data, provides status reports, and receives, relays, and responds to commands. Each camera computer runs a communicator instance. While all communicators listen for commands from the ground, one communicator is designated the "leader" and it assumes the bulk of the communication duties. While one specific camera computer is designated leader by default, the ground operators can change which camera computer assumes leader duties remotely since each communicator instance includes the leader functionality.

Upon booting up, each communicator reads a configuration file to set operational parameters. These parameters include the initial assignment of leader duties to one communicator, the lenses associated with each computer, the power system elements monitored by individual communications, the downlink attributes (such as bandwidth), and the peer polling order prescribing the order and frequency subsystems are polled. All of these operational parameters can be changed during operation. For example, if we lose contact with Iridium Pilot, we would want to decrease the downlink bandwidth on that link so we do not spend computational resources sending data that we will never receive. We may also want to change the peer polling order if we observed an interesting feature in a specific camera's FOV and could tolerate less frequent updates from other cameras.

While each camera computer captures data and aggregates housekeeping metrics independently, the leader requests data from other communicators and prepares these data for downlinking according to the peer polling order. It packetizes the data using the format described in section 5.3.3 and pushes packets down telemetry channels at a configurable rate.

The leader also aggregates housekeeping data from each pressure vessel as well as from the lidar and charge controllers. The communicator packages housekeeping updates in short status summaries of 254 bytes. It sends these updates periodically over a high rate channel interspersed with the science data packets. The SIP also periodically requests such summaries and sends them to the ground over the very reliable short burst channel.

While all communicators monitor and decode all command packets from the ground, only the leader responds to the vast majority. Each command packet includes an address for the commanded subsystem, and non-leader communicators ignore commands with most destinations. The exception is the "SUPER_COMMAND" destination, which all communicators monitor so we can set a new leader in the event we lose contact with the previous leader. When the leader receives a command packet, it pings the command destination. If the ping returns, the leader retrieves the function corresponding to the command packet, the keyword arguments from the command packet, and executes the designated function using the Pyro4 URI. The leader logs both ping failures and command results in a command log. Ground-side observers can request command log files. Short status updates also include information about recently executed commands.

5.3.3 Packet structure

The communicator packetizes each file in chunks of 1000 bytes. We developed a packet format to simultaneously use multiple communication channels with distinct communication protocols, and track missing or incomplete files with the ground-side software.

Our telemetry hardware required that our software be downlink agnostic. The TDRSS, Iridium Pilot, and LOS communication links use distinct communication protocols. Our software communicated according to each of these protocols, but wrapped the raw data "payload" in a common packet format, which allows the communicators to package data in a consistent format regardless of where the data would be queued.

Our custom packet format also identifies itself with respect to all data we have downlinked. We received data from Iridium Pilot at a fixed IP address on Columbia campus in Manhattan, data from the LOS link at our launch location in Sweden, and the TDRSS data at computers in Texas. We could access all these geographically separated computers remotely, but we needed metadata generated from the communicator to identify the files. For example, the Nth file could be sent over the Iridium Pilot link to New York while the N+1th file could have arrived in Texas over the TDRSS link.

Further complicating matters, we needed our software to account for missing packets and incomplete files. We expected regular and sometimes a significant percentage, of missing packets and early on we had decided to use UDP packets. Unlike TCP packets, UDP packets include no handshaking to determine whether data has arrived at the destination, so we had no built-in method of knowing whether data was missing. However, the absence of arrival verification meant UDP packets made for more robust communications. In the event of low quality connections, we prioritized maximizing the chance that packets would get through, rather than jeopardize the communication by requiring a TCP response. Instead of using built-in packet verification, when the communicator prepares data for downlink, it includes metadata with the packetized chunks indicating the communication channel and the packet number, along with the total packet numbers. This allows the ground-side software to track missing packets and aggregate packetized data back into complete files. We also include a checksum to verify that individual bytes for packets had not been corrupted or lost (for example, one packet losing its "tail" and another losing its "head").

As a consequence of this packet structure, we could built ground software to track arriving packets and assemble files in real time. We could watch our data arrive and quickly identify when our telemetry channels dropped packets. Figure 5.4 shows the file completeness over the course of flight, which we were able track due to our packet format. We could also reconstruct files missing only a few packets. While we have not pursued these measures (since we recovered all our data), the packet structure added robustness to our communication system.

5.3.4 The Controller

The controller software module interprets commands from the communicator and relays them to the pipeline in order to control camera settings and retrieves images from the data disks. It also handles grabbing files from the hard drives and compressing these files to prepare them for downlinking.

During default operation, the leader will cycle through the configurable peer polling order and request data from communicators. The prompted communicator will ask the controller running on the same computer to grab the latest image. The controller downsamples it, and applies lossy JPEG compression in preparation for downlinking according to configurable parameters. We typically downsample by binning squares of 8x8 pixels to 1 pixel of averaged value. Table 3.2 shows downlink speeds of several such downsampled and lossy compressed images over various telemetry channels.

As we monitor the experiment from the ground, we often want to review specific images and files. The controller can also prepare specific images upon request or raw files (such as a raw housekeeping log or uncompressed image). We also included the functionality of requesting specific regions of the image. A ground-based user could request the default downlinked image to be an arbitrary pixel area (such as 512x512) selected from any location in the image at any possible downsample resolution (that is a resolution reachable via integer division of the original resolution of the image).

The controller can also run multi-step processes, such as a focus sweep. The purpose of a focus sweep is to check and fine-tune the lens focus. To this end, the camera cycles through a range of focus steps, capturing an image at each step, and downlinks the images for ground review. The controller interprets the focus sweep command from the communicator and automatically prepares and relays commands to adjust focus step settings and retrieve images taken at each focus step. Typically, we look at stars since they are nearly point sources and we manually select a small region of the image where we have identified stars. We prepare and downlink only this region to reduce the volume of downlinked data.

While the controller primarily acts as an interface between the communicator and the pipeline, it has some automated duties as well. On a periodic interval, it checks for completed commands, executes steps in multi-step commands (such as focus sweeps or downlinking a series of images), and updates the merged index of images and commands. Whenever auto-exposure is enabled, it also runs our custom auto-exposure algorithm.

5.3.5 Ground Software Overview

We developed custom ground software to display status updates and files received from our payload. The software reassembles the packetized files prepared by the communicator and displays included metadata. The telemetry software on both the ground and payload side worked with all of our telemetry channels. The ground side software also communicated with the NASA SIP module for more reliable access to housekeeping metrics. We routed physical diagnostics such as currents, voltages, and pressure sensor readings through the SIP module. The SIP communication also added an alternate back-up control method with commands to open and close relays between the power system and subsystems. In the case of a short, we could isolate a malfunctioning subsystem. Alternately, we could power cycle computers that had crashed.

We wrote ground side software to display updates in a quickly readable graphical user interface (GUI) for the ground monitoring team. We also wrote GUIs to display incoming files with the number of packets expected and received, as well as an image viewing GUI that includes image metadata.

Furthermore, we wrote software to facilitate commanding the payload. It translates human-readable commands into a compact form and facilitates switching command uplink channels. The command software tracks the command verifications included in downlinked housekeeping and displays whether the verification has been received for sent commands.

Finally, we developed a GUI to display image files received by the ground computer. In addition to convenient image displaying features, this GUI displayed image metadata and generated commands to request a graphically selected section of a specific image file. Figure 5.3 displays a screenshot of the GUI taken during flight displaying a downlinked image containing PMCs. The dynamic range has been stretched within the GUI software to emphasize the PMCs, visible as bright stripes oriented diagonally within the image. The left column displays metadata, including exposure time, aperture stop, file id, and focus step. The metadata also informs the viewer of the downsampling of the image and the time stamp of the image. The bottom line gives a command a viewer could send to request a highlighted portion of the image, selected using the tool visible in

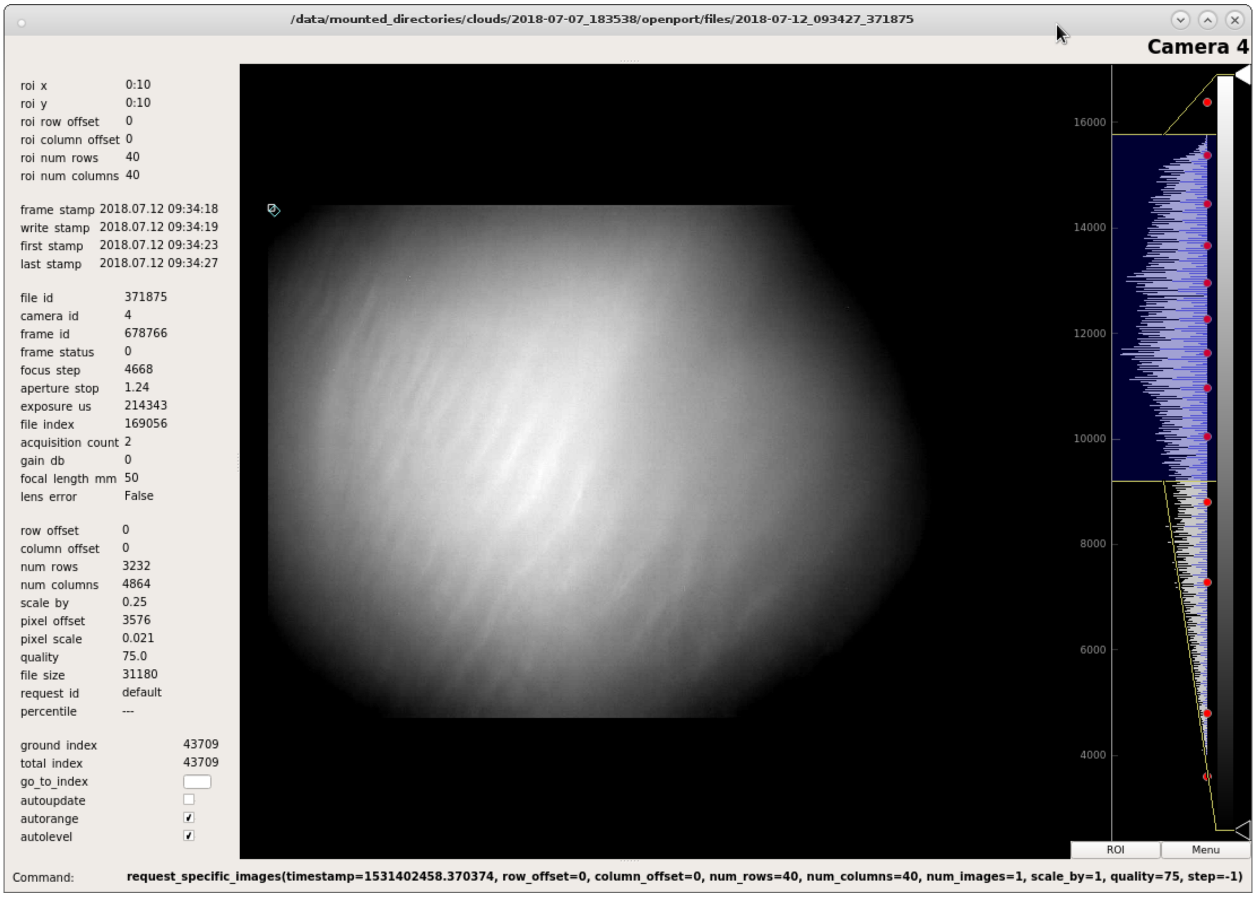

/data/mounted_directories/clouds/2018-07-07_183538/openport/files/2018-07-12_093427_371875

roi x	0:10
roi y	0:10
roi row offset	0
roi column offset	0
roi num rows	40
roi num columns	40
frame stamp	2018.07.12 09:34:18
write stamp	2018.07.12 09:34:19
first stamp	2018.07.12 09:34:23
last stamp	2018.07.12 09:34:27
file id	371875
camera id	4
frame id	678766
frame status	0
focus step	4668
aperture stop	1.24
exposure us	214343
file index	169056
acquisition count	2
gain db	0
focal length mm	50
lens error	False
row offset	0
column offset	0
num rows	3232
num columns	4864
scale by	0.25
pixel offset	3576
pixel scale	0.021
quality	75.0
file size	31180
request id	default
percentile	---
ground index	43709
total index	43709
go_to_index	☐
autoupdate	☐
autorange	☑
autolevel	☑

```
Command:    request_specific_images(timestamp=1531402458.370374, row_offset=0, column_offset=0, num_rows=40, num_columns=40, num_images=1, scale_by=1, quality=75, step=-1)
```

Figure 5.3: Image monitoring GUI with PMCs during the PMC Turbo flight

the upper left of the image. To the right a histogram of the image allows a viewer to change the display colorscale live and see image statistics.

5.4 Continuous integration and using a testing suite

We used continuous integration methods, including a comprehensive test suite and a code coverage report, to facilitate speedy development and to ensure the robustness of our code.

At its core, continuous integration refers to the practice of merging new code developments several times per day, rather than merging infrequently. The motivation for this development style is avoiding integration conflicts that can emerge as separate versions of the code diverge. In order to implement continuous integration, one needs to implement tests that new code developments have not broken existing functionality of the project.

We used the "Travis CI" service for continuous integration. This linked with our version control software (git hosted by Github). Every time one of our team members pushed a change to the git repository, Travis CI built a virtual environment to simulate our operating system, built the code (we mostly used Python, but our camera hardware interface used C++), and ran our suite of unit tests. We wrote the unit tests to catch expected and general errors that could occur. We used another service "Codecov" to check our test coverage. This service gave us a line-by-line report of the code that our tests used and summarized this data with a percentage of our code that our tests covered. If an addition or alteration pushed by our software team caused a test to fail, we would receive an alert.

5.5 Flight Performance

During flight we successfully sent commands in real time in response to the changing sky conditions, we observed PMCs even in low quality downlinked images, as shown in Figure 5.3, and we used the communication channels to run several live tests including using stars to dial in our focus settings with focus sweeps and measuring the sky brightness as a function of sun angle.

We maintained communication with the payload over the LOS link from launch for 20 hours

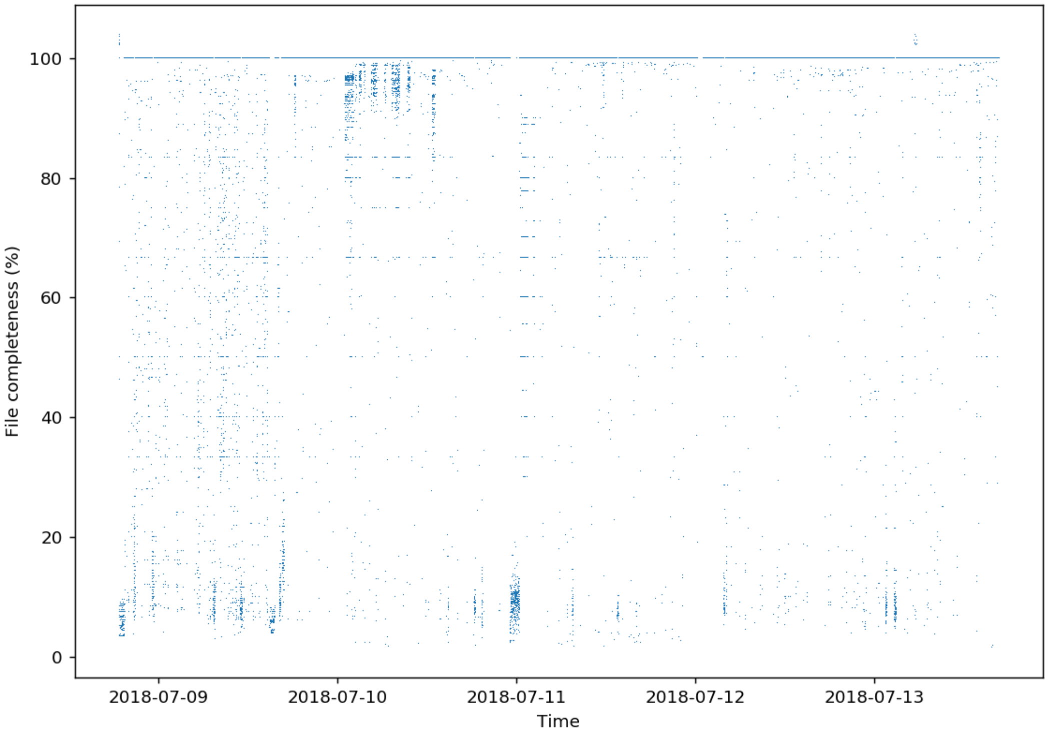

Figure 5.4: File completeness over the Iridium Pilot link

- until 9 July 03:38 UTC. We dropped 1% of the downlinked packets over the LOS link during this time, but we did not encounter any periods of the link dropping completely. Figure 5.4 tracks each distinct file id we received over the Iridium Pilot link, the arrival time of that file, and the percentage of packets from that file that we received. While we had a few brief periods without Pilot communication, Iridium Pilot dropped 0.1% of the packets when we had connection. These outages typically lasted less than 30 minutes, but we did have two Pilot outages that lasted over an hour. Over the duration of the flight, 92.3% of files sent were received completely.

TDRSS generally performed as well as Iridium Pilot. However, we encountered a bug with our ground-side computers receiving TDRSS data so we periodically needed to restart the software. Our ability to debug these issues were limited since the ground-side computers were located in Texas, while our ground team stayed in Sweden for the duration of flight. Furthermore, a network issue affecting the Columbia Scientific Ballooning Facility that housed our computers cut off access to TDRSS communication. As a result of these issues, we have less reliable quantitative measurements of the TDRSS performance. Anecdotally, TDRSS worked well when we did not encounter software or networking errors.

During flight we downlinked over 37,000 files over the LOS link, 245,000 files over Iridium Pilot, and 257,000 files over TDRSS. Of these 540,000 files, about a third were compressed images. We did not need to use the compressed images for analysis since we ultimately recovered our raw data, but they provided a backup option in case we had lost the payload.

5.6 Analysis software

In this section, I will discuss the most important attributes of the analysis software enabling the pursuit of our primary science objectives.

The LDB EBEX Analysis Pipeline (LEAP) successfully analyzed PMC images from EBEX [15], so I used the same structure for our analysis software. The software is structured such that "apps" generate specific data products while importing generalized procedures from shared libraries of code. This structure is standard for the development of software projects, which makes publishing and maintaining this code as an open-source package straightforward.

5.6.1 Libraries

The libraries include functions we frequently use in analysis programs. The intention behind this structure is that these tools will continue to be refined and developed, rather than duplicated during individual analysis projects. Libraries include functions performing image processing and projection, movie making, power spectrum calculation, and data handling and manipulation. Of these tools, I discuss the image processing, pointing, and projection procedures in section 6 as it central in all our image analysis.

5.6.2 Apps

While the libraries included code designed to perform a frequently used tasks, each app generated a specific data product. For example, I wrote separate apps to generate image series, power spectra statistics, and Lomb-Scargle periodograms. All these example apps drew from the shared image processing and projection libraries.

Each app inherited a framework and associated functionalities from a parent class. This class defined a common template imposing requirements and providing features for each app. This included receiving input parameters in a dedicated settings file. For example, the image series app settings included timestamps for images, which camera data to include, which flat-field procedures to use, which region of the sky to show, which color scale to use, whether to show timestamps, and whether to output a series of individual images or a movie file. Another important feature of the app parent class was generation of an output file. This file included the data product generated by the app, logs from running the app, and the settings used.

While the consistent structure and output does not change the data product, the consistent structure facilitates users other than the author in using apps. It also helps when a user wants to generate data products while using previous products as a reference.

Chapter 6: Data Reduction

During the PMC Turbo flight, we sent compressed images to the ground via our telemetry channels. A few of these images revealed bright structures we knew to be PMCs. However, our experience with EBEX PMC images taught us that many features would only become apparent after removing reflections and background noise from our data. We implemented image correction techniques to examine our data, and these became the first entries to our software libraries described in section 5.6. Furthermore, our cameras captured a rectilinear projection of the sky due to their geometry, so we needed to convert this projection back to the physical plane of the PMCs in order to correctly analyze scales and morphology of observed dynamics.

6.1 Image Calibration and Reflection Removal

All images were calibrated with a flat-field image, dark image, and simulated sky brightness. In this process we used the following calibration data:

- A dark image D defined before flight to account for the dark current in the CCD.
- A mean flat field F defined before flight from twilight images with varying brightnesses to account for vignetting, illumination differences due to the lens hardware, and variations in pixel sensitivity.
- A simulation of sky brightness S developed by another graduate student accounting for brightness due to air mass and the scattering angle between each pixel's view and the sun.

From these factors a calibrated image I' can be constructed from the raw data I using the standard flat-field equation:

$$I' = \bar{F}\frac{I - D}{F - S} \tag{6.1}$$

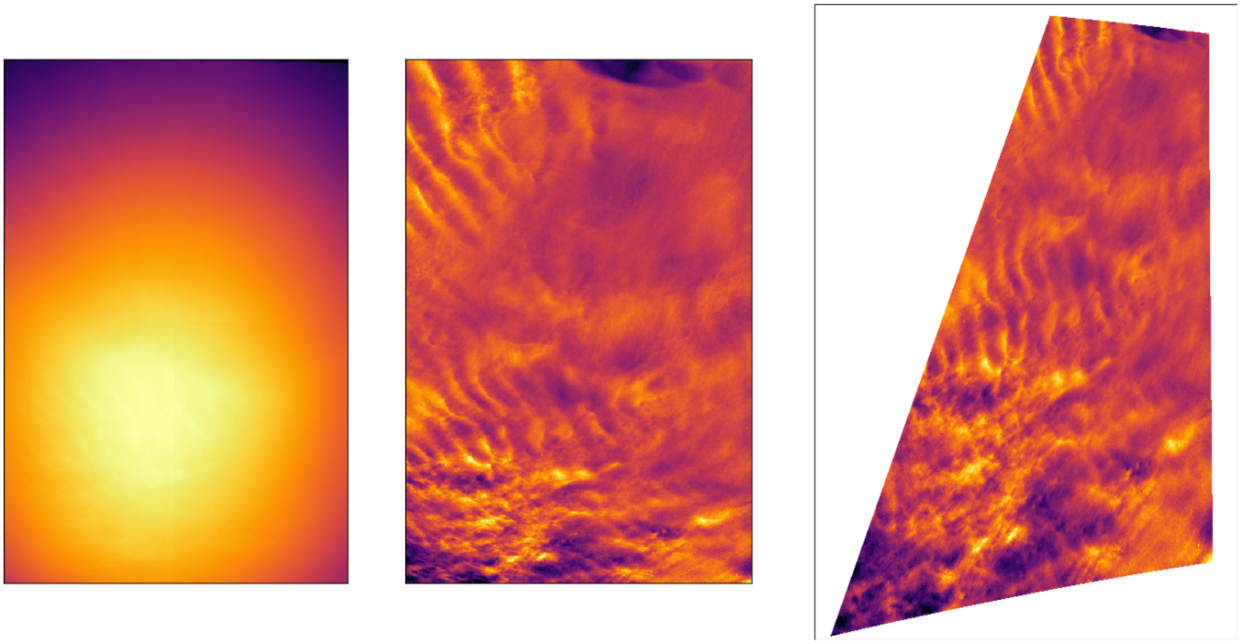

Figure 6.1: From left to right: raw false-colored image of one of the wide-field cameras containing PMCs; the same image after flat-fielding; and the same image after flat-fielding and projection based on the pointing solution. Up orientation in the first two images corresponds to the zenith, and up orientation in the projected image corresponds to the longitude of the sun. We projected the image looking from below

The adjusted image I' was divided by exposure time to standardize response between cameras as exposure times were not uniform. Finally, a moving average - typically of 10 minutes - was subtracted from I' to compensate for scattered light and generate the final image used for analysis.

Figure 6.1 shows a raw image to the left and an image corrected using the steps above in the center. Of these corrections, the removal of the moving average is by far the most significant.

6.2 Pointing

Images were captured on a rectangular CCD, with cameras pointed with the upper edge of the FOV aligned 25 degrees off-zenith to avoid the balloon directly overhead. This introduces rectilinear distortion, which was removed by finding the pointing of the images using background star fields. For each camera we found the sky location of an evenly-spaced grid of pixels (spaced every quarter of the CCD, including the edges). We interpolated over this grid to map each pixel in the CCD to the proper location on the sky.

The PMC-Turbo cameras were based on earlier star cameras designs from the EBEX experiment. While these cameras serendipitously captured high resolution PMC images, their purpose was to find the pointing of the EBEX telescope. Our pointing requirements were less precise than the EBEX instrument, and we were able to find pointing based on identified stars in our images.

6.2.1 Locating and Identifying Stars

In order to use the star field to find pointing solutions, we needed to locate and identify stars. We used a procedure based on the star finding procedure used in EBEX described in depth in Daniel Chapman's thesis [15] and used the image manipulation python package CV2 python, which wraps the well-known library OpenCV. The star identification algorithm operates as follows:

1. We mask previously identified "hot pixels".
2. We convolve the image with a Gaussian kernel of configurable size and sigma in order to smooth the image.
3. We divide the image into sections - or "cells" - of configurable size.
4. In each cell we look for values above a configurable threshold level.
5. We compare the pixel brightness values at above-threshold levels to the pixel brightness values in a dilated version of the same image. If the values are the same we have found a local maximum.
6. We select a configurable number (typically 1) of local maxima for each cell and return their coordinates.
7. As an optional additional step, we fit 2-dimensional Gaussian distributions to each blob. We can filter by the sigma of the Gaussian fit to filter out unphysical results caused by CCD artifacts that have slipped through our other filters.

Figure 6.2b shows stars identified following these steps. Figure 6.2a shows the location of these stars in the corrected image before projection.

After we locate stars, we used the off-the-shelf tracking software package Astrometry to get the right-ascension and declination (ra/dec) of an evenly spaced grid of pixel locations. From right ascension and declination we converted to azimuth and elevation of the grid using GPS timestamps and locations from the flight. The gondola was rigid, so we didn't expect our pointing solution to shift during flight. We calculated pointing periodically throughout flight to verify this assumption. Figure 4.1b shows the arrangement of all our camera FOVs found using the pointing calculated from identified stars. Each camera FOV in this figure shows the results as a grid, which represents the CCD locations we use to find a pointing solution for each pixel.

6.2.2 Projecting

Once we have a pointing solution for the evenly-spaced grid of pixels for each image, we project the raw image onto the plane of the PMCs to reconstruct their true scale and morphology. From the grid we interpolate the location of every pixel in the raw image. We wrote two processes to use these pixel locations to project the image. Each has unique benefits and drawbacks.

One technique is pixel projection. This technique maps the pixel brightness value to the location of the pixel on an x-y plane at the PMC altitude determined by the pointing solution. Compared to the method described below, this method is fast. However, this method did not generate evenly-sampled data as pixels at large off-zenith angles gathered light from a larger area than those at small off-zenith angles. This method can more easily rotate the projected FOV with changing pointing due to the rotation of the sun through coordinate transforms (recall the cameras always pointed anti-sun).

The second technique developed is grid mapping. In this method, an evenly spaced grid representing the sky at the PMC altitude is filled in the pixel brightness values. These values are found from the source image by mapping each grid pixel to the corresponding image pixel. A Cartesian grid on the PMC plane is chosen, with the origin chosen to be the location of the gondola and the

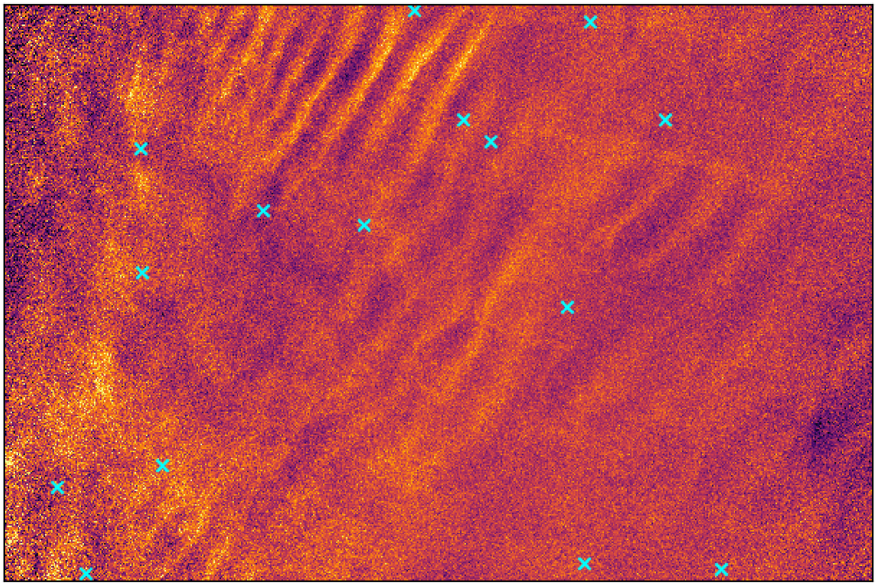

(a) Location of stars within an unprojected image

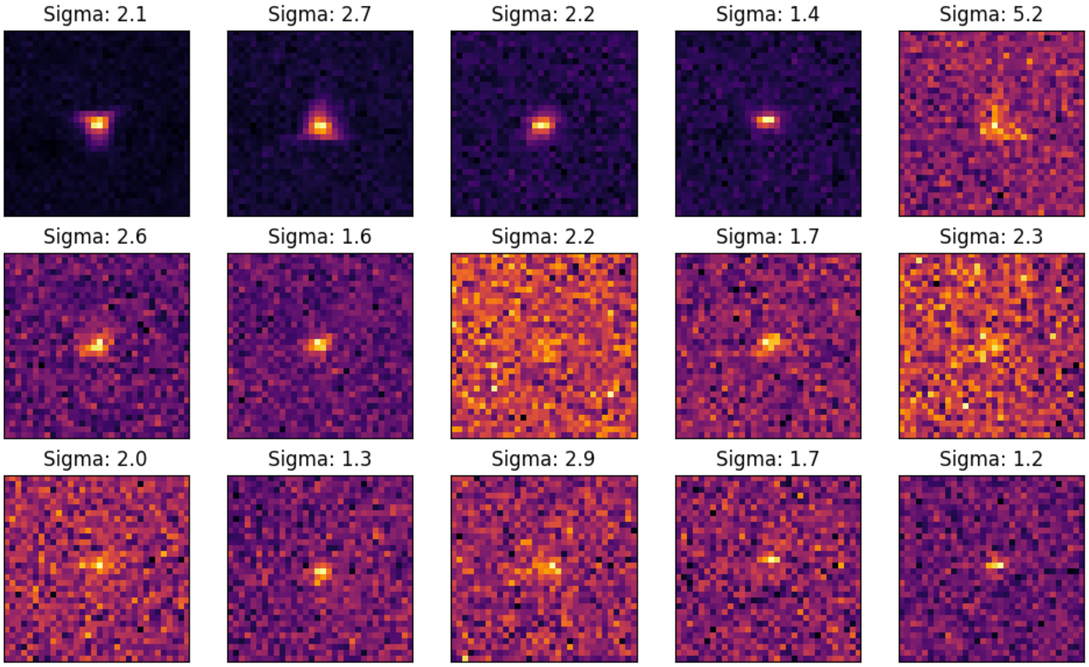

(b) Fifteen identified stars in the unprojected but corrected image in panel a

Figure 6.2: Star identification

-Y direction corresponding to the anti-sun direction. The grid can be instantiated at any resolution, so the spatial resolution of the final data product is limited by the raw image spatial resolution. While this process has been optimized to use standard look-up tables rather than calculating the pixel corresponding to each grid, the pixel-by-pixel fill still takes longer than the pixel projection. As a result, we tend to use this method during short duration events where the sun's rotation does not have a large effect or when we do not care about the cardinal direction of the dynamics. The evenly spaced grid facilitates many quantitative analysis techniques such as 2D power spectra. I use this method for the images shown in this dissertation since the events I analyze evolve on a short timescale compared to the movement of the sun.

Chapter 7: Complementary Data

7.1 Introduction

To maximize the return from our high resolution measurements of MLT dynamics, it is helpful to analyze our data in the context of other complementary measurements.

In addition to the science goals described in section 3.1, a primary objective of PMC Turbo was testing the experimental design. PMC Turbo was the first balloon-borne experiment designed to image PMCs during a multi-day flight and we hope it will not be the last. Part of the motivation to fly PMC Turbo over the Arctic, rather than the Antarctic, was that the accessibility of Arctic flights allowed for testing the experiment prior to a more expensive deployment and lengthy waiting period for an Antarctic launch opportunity. In this chapter, I describe complementary measurements both with the goal of achieving our science goals as well as identifying the most useful sources of complementary data to better coordinate observations during future flights.

This chapter will primarily discuss measurements from other experiments that help us understand the sources and influences on GWs that drive the instabilities traced in the PMC layer. These measurements include PMC brightness measured by onboard lidar built by DLR, temperature perturbations derived from the same lidar, lower altitude wind and temperature measurements derived from a global weather model, and satellite imaging of PMCs from the CIPS instrument.

This chapter also discusses measurements that help us understand when we can expect PMCs to occur. While our science goals prioritize understanding GWs and instabilities, we use PMCs to achieve these objectives, so understanding their behavior is important for future experimental design. Towards this objective, we use hourly winds in the MLT measured by meteor radar and cross-reference the winds against the observed PMC presence.

The complementary data presented here is not the subject of my own analysis. I present it to provide important context for GW dynamics in the MLT during the PMC Turbo flight. While PMC Turbo probed several decades of spatial scales, understanding GWs requires synthesis of many different types of measurements to cover the vertical and horizontal extent and scales.

7.2 PMC brightness profile

7.2.1 Science goals

As describe in Chapter 1, GWs are characterized by oscillatory horizontal and vertical motions that can be as large as meters to tens of meters per second and periods of a few minutes to many hours. In the MLT, the resulting vertical displacements can be several kilometers. PMCs move with the air, and we use PMCs displaced in this way as tracers for GWs. Advancing our understanding of GWs and instabilities in the MLT is necessary to achieve the PMC Turbo science goals described in section 3.1. The goal of the measurements described in this section is to identify GWs and other dynamics with periods of less than 60 minutes. These GWs propagated through the PMC layer and drove the dynamics we imaged with our cameras.

GWs are not the only phenomena that can cause vertical displacements of PMCs. Instabilities that cause GW dissipation also induce vertical motions at the spatial scales we measure (tens of meters to kilometers).

7.2.2 Measurement details

We measure the vertical motion of the PMC layer with the Rayleigh lidar included on the PMC Turbo gondola. The Rayleigh lidar was the first high-power (4.5 W) lidar to fly aboard a stratospheric balloon experiment. It emits 532 nm light and measures the light of the same wavelength collected by an attached telescope with a 0.5 m diameter mirror over time. After measuring the baseline level of 532 nm light, the lidar can measure the amount of light from the laser scattered back towards the telescope by intervening aerosols. We use the term "backscatter" to describe this measured quantity. By measuring the time delay between emitting a pulse of light and collecting the backscatter, we know the distance to the aerosols.

The lidar had a pulse repetition frequency of 100 Hz and a pulse length of 1.5 m (5 ns). After laser pulse is emitted the receiving instrumentation records received 532 nm photons in time bins. From this raw data, one can produce a profile of the amount of backscatter by distance. The PMC Turbo lidar pointed 28 degrees off-zenith to avoid viewing the balloon - upwards at the PMC layer.

The ice particles that make up PMCs are highly reflective in visible wavelengths. They are apparent in the lidar data as regions of high backscatter. There are no other highly reflective (at 532 nm) aerosols at the altitude where PMCs reside and our camera measurements of PMCs match the lidar results, so we have no doubt that the features the lidar observes are PMCs.

7.2.3 Observations

Figure 7.1 shows the measured backscatter at several times throughout the PMC Turbo flight. Each subplot shows the backscatter coefficient measured by the lidar over time and altitude.

The PMC Turbo lidar observed many instances of vertical motions having apparent periods of 5-60 minutes. Panel b shows vertical motions with periods around 20 minutes between 19 and 20 UT. Vertical motions with periods of 15 minutes are apparent in panel d shortly after 21 UT, and motions with periods near 20 minutes are apparent in the same panel starting at 22:40. Panel e shows periodic motion with a period near 30 minutes starting at 14:15, and again at 15:30.

The lidar also observed a few instances of motions with periods less than 10 minutes. Panel a, especially between 5:30 and 6 UT shows these rapid oscillations. We also see them in panel c at 10. Panel d contains such motions between 21 and 22 UT as well as between 23:30 and 00 UT. Panel e has very interesting short scale oscillations at 13:30 that I examine more closely in Chapter 8.

Finally, we see an unexpected dynamic: multiple distinct layers of PMCs. We can see multiple weak layers in both panel a and b persisting through most of the observation duration. Panel d at 23:30 and panel e between 14 and 15 UT show two especially bright layers. An interesting feature of these layers is that they appear to move upwards and downwards in a synchronized manner. This is particularly apparent in panel e between 14 and 15 UT and in panel b after 19 UT.

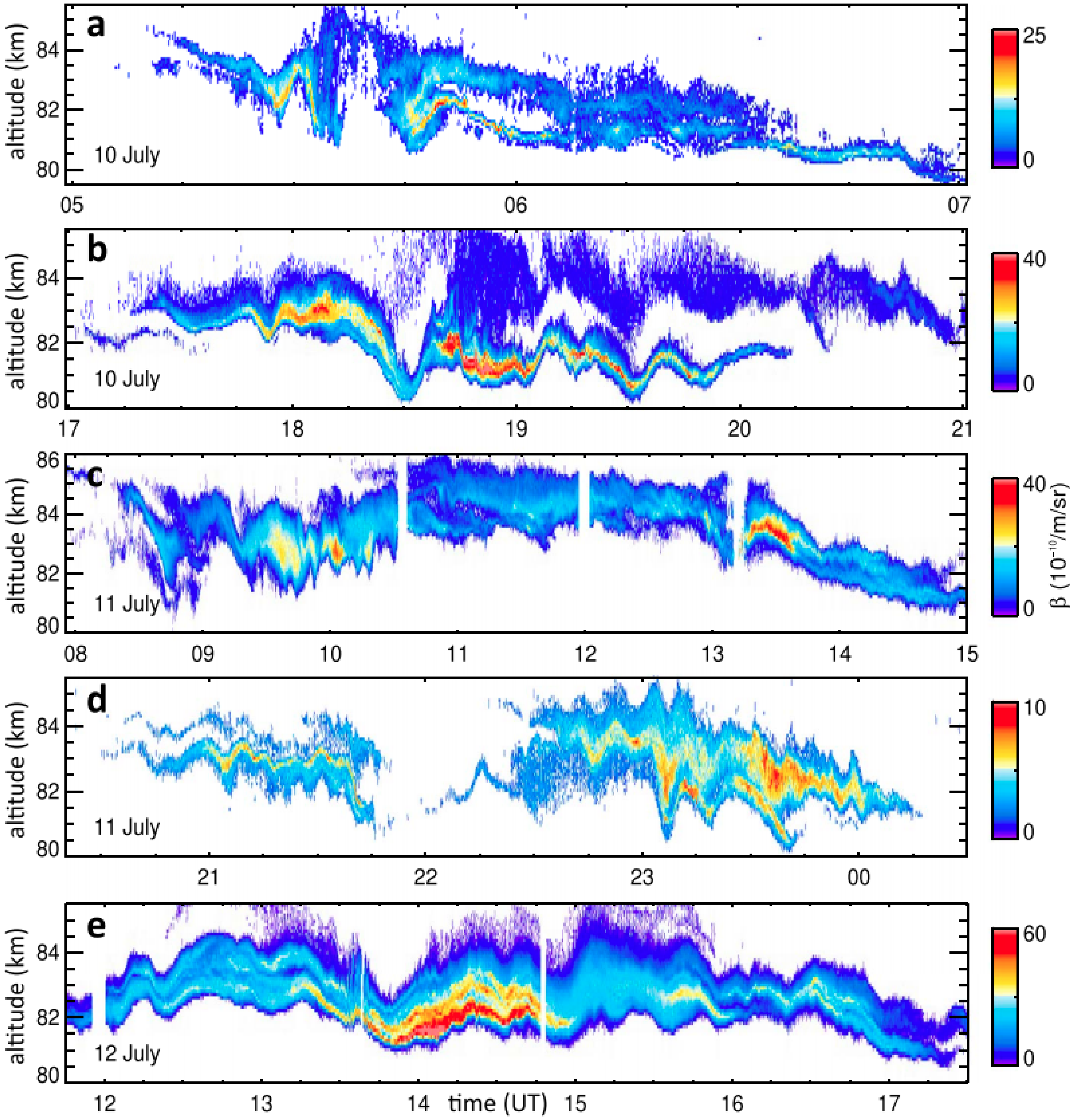

Figure 7.1: PMC backscatter measured by the Rayleigh lidar aboard the PMC Turbo instrument.

7.2.4 Discussion

Our observations of vertical periodic motions of 10-60 minutes matched our expectations about an observable effect of GWs on the PMC layer. We can use the frequency of these motions to estimate the vertical wavelength λ_z of the GWs. As noted in our 2017 paper analyzing PMC images [29], GW breaking instabilities limit the vertical displacement of hydrostatic GWs to

$$\zeta = w'/\omega_i \sim \lambda z/2\pi \tag{7.1}$$

where ζ is a vertical perturbation, w' is the vertical velocity of the GW, ω_i is the intrinsic frequency (the frequency relative to the flow). We were not able to measure w' with the PMC Turbo lidar, and we do not know the background winds so we cannot calculate ω_i. However, we do know from previous observations [21] that realistic mean winds do not Doppler shift small ω_i to large apparent values measured by a fixed observer. Using typical vertical velocities, we estimate the the GWs most likely causing the observed vertical motions of the PMC layer have a λ_z in the neighborhood of 5-10 km.

Our observations of vertical motions with periods shorter than 10 minutes match our expectations for the vertical displacements of the PMC layer by instabilities in specific cases. Chapter 8 describes one instance in which we identify Kelvin-Helmholtz instabilities in the lidar backscatter measurements.

We are currently studying the distinct layers we observe over several periods during flight. The persistence of these layers over time scales of hours and their synchronized movement suggests that they are not created by the dynamics that cause vertical motion with periods of <60 minutes. Possible explanations include meridional advection of air from regions of higher/lower PMC ice particle density and regions of persistent temperature differences, enabling differential PMC formation and sublimation, but we have yet to confirm these theories.

Broadly speaking, our investigation into the vertical motions measured by the lidar backscatter matched our expectations for vertical motions from GWs and instabilities in the PMC layer.

However, we see a diverse variety of dynamics during our flight and we do not have large sample sizes of any specific phenomenon or direct measurements of quantities such as wind speed or vertical velocity that would allow for more quantitative analyses. We have implemented feature tracking algorithms to determine horizontal velocities, but work still needs to be done to disentangle the movement of PMCs by ambient winds and the propagation and superposition of features traced by PMCs occuring at smaller and larger spatial scales respectively. We have found the PMC backscatter data is most useful analyzing specific events. For example, I used the lidar data from 13:20 to 13:40 to support my analysis of Kelvin-Helmholtz instabilities in Chapter 8 and we use the backscatter data to support analysis of mesospheric bores in our 2020 paper [26].

7.3 Temperature perturbations

7.3.1 Science goals

Our goal in measuring temperature perturbations was to observe signatures of GWs at altitudes between the gondola and the PMC layer in order to better characterize the GWs driving the dynamics traced by PMCs. As GWs propagate, they displace air vertically and horizontally, as noted in the previous section, and vertical displacements cause temperature fluctuations. The atmosphere temperature varies with altitude and there is a significant temperature gradient in many locations. Adiabatic cooling and warming of displaced air parcels results in temperature fluctuations as well as displacement of air along the temperature gradient. Accounting for these factors we find temperature perturbations T' with a vertical displacement δz to be

$$T' = -(dT/dz + g/c_p)\delta z \tag{7.2}$$

where g is the gravitational acceleration and c_p is the specific heat capacity [27]. See Appendix A.22 for details on the second term in parentheses.

GWs can be observed by the temperature fluctuations they cause in the atmosphere. In this particular case, we aim to observe the propagation of GWs between the PMC Turbo gondola altitude and the PMC altitude. This provides another window into the formation and context of the GW and instability dynamics imaged by cameras and contributes to our broad science goals outlined in section 3.1.

7.3.2 Measurement details

We use the Rayleigh lidar to measure temperature fluctuations between the PMC Turbo gondola at 38 km altitude and the PMC layer around 83 km altitude. Both Rayleigh and Mie scattering of light by air are well understood. Rayleigh scattering is a function of total density while Mie scattering is a function of the density of particles with similar sizes to the wavelength of light [35] [46]. The backscatter profile of the lidar can therefore be used to calculate a density profile, and from density one can find temperature by assuming hydrostatic equilibrium and applying the ideal gas law.

This procedure does not work in the region of the PMC layer. The PMC layer is 45 km away from the lidar so the Rayleigh scatter signal is weak compared the PMC backscatter. However, we can use this method to determine temperatures in the region between the gondola and the PMC layer.

7.3.3 Observations

Figure 7.2 panel a shows the temperature fluctuations derived from the lidar measurements over the full duration of the flight. Panel b shows these measurements only on July 12. T'(z) was derived using the process described above using a Butterworth filter with a cutoff of 15km, a 1.3 km averaging in altitude and 60/20 min averaging for panels a and b respectively.

Periodic features are apparent throughout flight, and I have highlighted several examples of such periodic structures in panel b with black lines. These features are present between 50 km and 70 km altitude.

Additionally, smaller scale temperature fluctuations are consistently present between 73 km and 80 km altitude. I have highlighted these features with a black oval. These features are less clearly

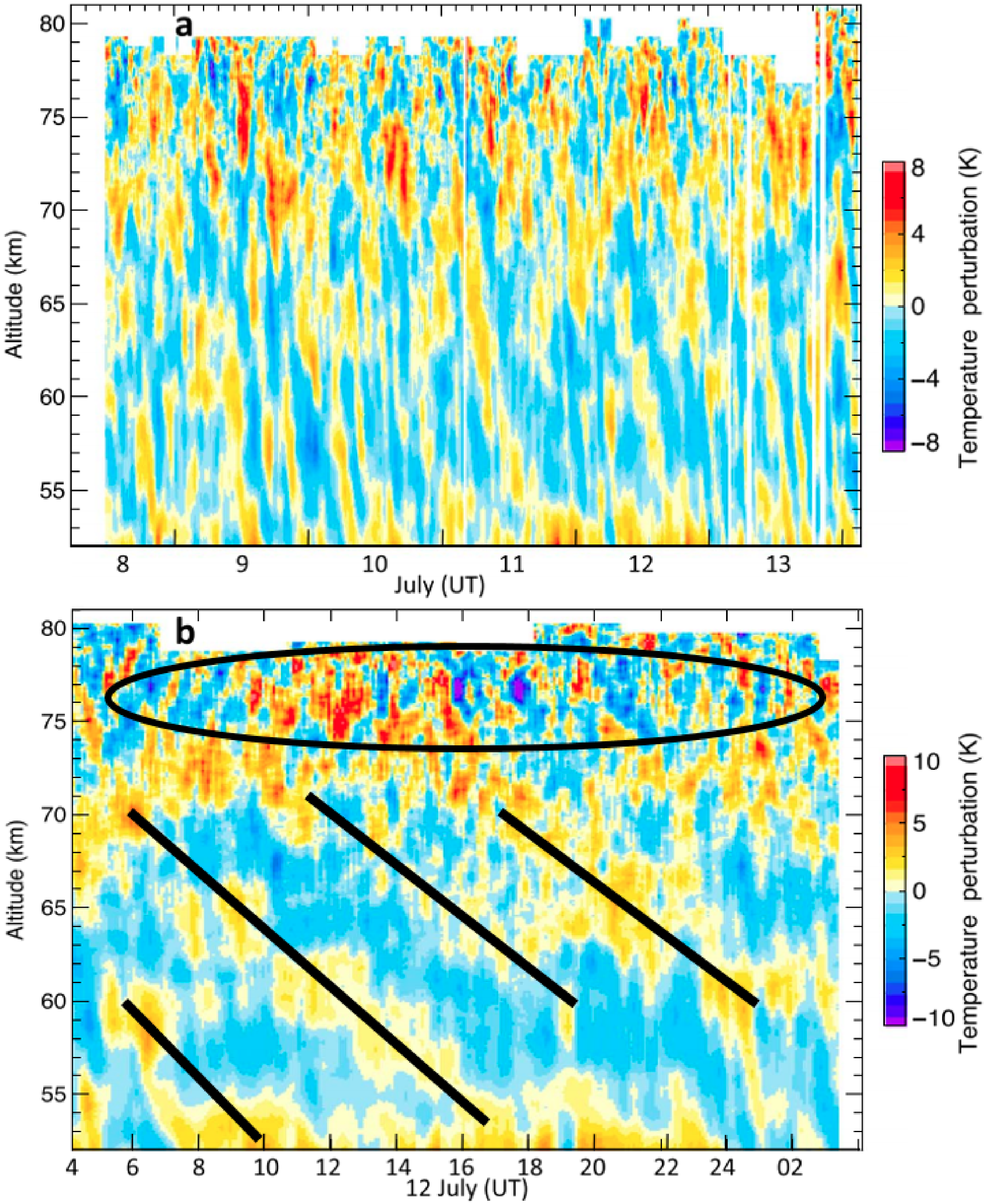

Figure 7.2: Temperature fluctuations derived from Rayleigh lidar measurements

periodic than the larger features at lower altitudes. However, we do see evidence of periodicity on the order of 1 hr - for example between 13 and 16 UT on July 12 and after 22 UT that same day. The smaller scale features also have larger temperature perturbations than the lower altitude features - 10 K amplitude as opposed to 5 K.

7.3.4 Discussion

The temperature fluctuations between 50 km and 70 km altitude match our expectations of the temperature fluctuations caused by GWs. While the observed phases of temperature perturbation propagate downward with time, a well-known characteristic of GWs is that their vertical phase velocity and vertical group velocity are of opposite signs [43]. Hence these observations are consistent with GWs propagating upward from below.

The higher altitude features do not match the behavior of GWs simply propagating upwards, but instead match our expectations of temperature fluctuations resulting from GWs propagating upwards, breaking, and forming secondary GWs. GW amplitudes increase with altitude due to the decreasing atmospheric density, and as amplitudes increase GWs become more prone to instabilities. Several studies have shown that as GWs break and dissipate, they can generate secondary GWs with smaller wavelengths, larger intrinsic frequencies, and larger temperature fluctuations with increasing altitude [10] [36], which match the smaller spatial scales and higher intensities we observe.

Our observations match the temperature fluctuations we would expect from GWs propagating upwards to around 70 km altitude, and then breaking resulting in more intense and higher frequency secondary GWs about 70 km. The PMC layer resides between 80 and 85 km altitude, so our measurements of temperature fluctuations suggest that the features we observe traced in the PMC layer are primarily driven by secondary GWs.

7.4 Local weather measurements

7.4.1 Science goals

The goal of the data presented in this section is to identify likely GW sources and critical levels that could have filtered GWs with specific horizontal phase speeds.

As described in Chapter 1, GWs can be generated at lower altitudes by orographic and nonorographic sources. As part of our science goal of understanding GWs influencing the PMC layer that we observe, we looked at low altitude weather measurements to find likely GW sources near the time and location of our flight. Orographic GWs are caused by winds over terrain resulting in vertical displacements. Nonorographic GWs have more diverse sources including convection, fronts, and jet streams. PMC Turbo flew over multiple mountainous regions, so we expected orographic GWs to contribute, at least indirectly, to the dynamics observed by the PMC Turbo cameras. We also expected nonorographic GWs from jet streams, which are prevalent in the summer at polar latitudes.

In order to understand the propagation of these GWs, we also inferred the potential influence of critical levels they may have encountered. A GW "critical level" is defined as the altitude where the background wind speed is equal to the GW horizontal phase speed. It can be shown using the Taylor-Goldstein equation that when the background wind speed and GW horizontal phase speed are equal, the GW vertical wavelength and vertical group velocity approach zero, the GW cannot propagate further upward, and must dissipate [56].

Critical levels have important consequences for the macroscopic influence of GWs on the upper atmosphere. They filter out GWs with specific horizontal phase speeds, allowing only a subset of GWs to deposit momentum at higher altitudes. This leads to macroscopic air flows, as the deposited momentum has a nonzero net magnitude and direction. Furthermore, while the “critical level” prevents propagation in theory, in reality GWs become less stable as they approach this level, so they tend to dissipate due to various instabilities before reaching the level. This dissipation can generate more dynamics, including secondary GWs.

7.4.2 Measurement details

The PMC Turbo gondola included no instruments to monitor weather below it. To investigate GW sources and critical level filtering, we use data from the European Centre for Medium-Range Forecasting (ECMWF). ECMWF is one of several weather models that simulates the physics of the atmosphere to understand global and regional weather.

Scientists cannot measure all points of the atmosphere at all times. However, one can reliably understand the state of the atmosphere at some point in the past by using the available measurements as boundary conditions for sophisticated atmospheric models like ECMWF. This process of "reanalysis" uses archived observations to create global data sets describing the recent history of the atmosphere, land surface, and oceans.

Unfortunately, the PMC Turbo gondola flew through a poorly measured region of the atmosphere. It is difficult to make measurements at 38 km altitude anywhere on Earth, and the Arctic is a difficult place to maintain measurement stations due to its remote and harsh conditions. ECMWF gives us a best guess for the large-scale dynamics in a huge data void. I present reanalysis results from 36 hours during the PMC Turbo flight. We use the results available to us to formulate an educated guess about likely sources of GWs observed as our gondola passed over the North Atlantic and critical levels due to background winds.

7.4.3 Observations

The ECMWF reanalyses horizontal winds are shown in Figure 7.3 panels a - h. The colors show the wind speed and the barbs show the direction. The left column shows these forecasts for 700 hPa geopotential height, while the right shows them for 200 hPa. The black lines show the smaller scale geopotential gradients. For reference, 700 hPa corresponds to around 3 km altitude while 200 hPa corresponds to around 12 km altitude - roughly the height of commercial jet flights. The blue dot over Greenland shows the location of the PMC Turbo gondola at July 11 00:00 UT.

The reanalysis horizontal winds show a couple of notable features. In panels a, b, and c we observe a fast winds extending over Iceland. These winds move towards the northeast and become

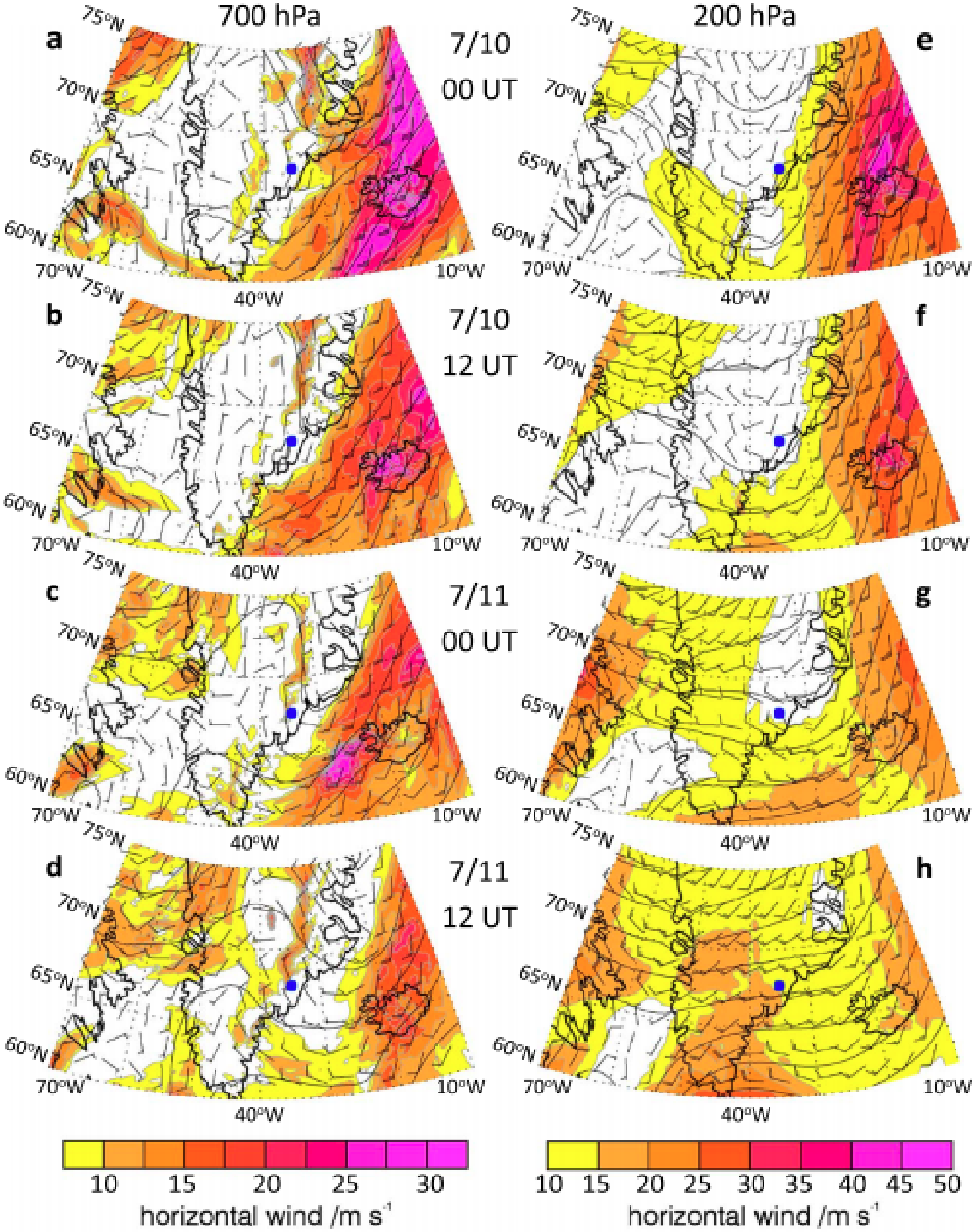

Figure 7.3: Wind results at 700 hPa and 200 hPa from ECMWF reanalysis

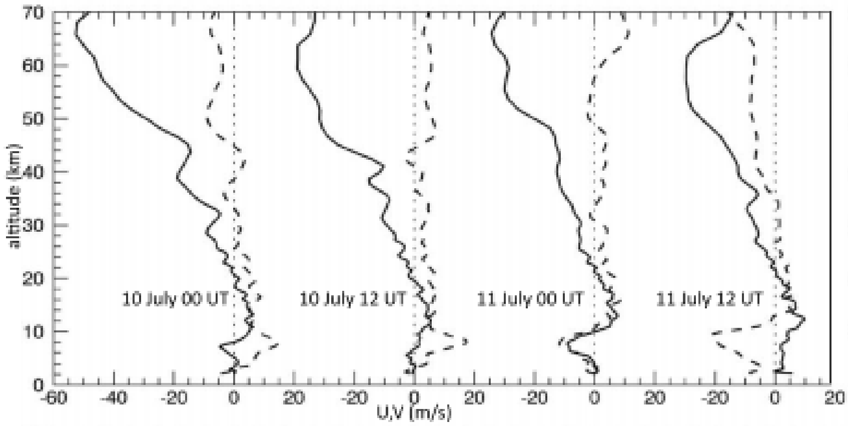

Figure 7.4: Vertical zonal and meridional winds from ECMWF reanalysis

weaker over the 48 hours shown in Figure 7.3. This feature is particularly apparent at 700 hPa geopotential altitude, although panels e and f show that it is weaker but apparent at 200 hPa geopotential height as well. The winds over Greenland rotate in direction and become more intense over time. This is particularly apparent at 200 hPa geopotential height.

Figure 7.4 shows the horizontal wind speed as a function of altitude at selected times during the PMC Turbo flight. The solid line represents "U", the zonal velocity of the winds (along latitude lines), while the dashed line represents "V", the meridional velocity of the wind (along longitude lines). We can see that the wind velocity was mostly in the westward (negative zonal) direction and that it goes from 30 m/s in this direction at 30 km altitude to about 50 m/s at 50 km altitude. The U and V components of wind velocity reverse near 10 km altitude, and then again around 20 km altitude.

7.4.4 Discussion

The evolution, morphology, and magnitude of the winds over Iceland and east of Greenland can be explained by a temporary jet stream. Jet streams are a common source of nonorographic GWs, so it is likely this one created GWs, especially on the 9th and 10th of July, when it was strongest.

The rotating and intensifying winds over the southern tip of Greenland can be explained by the presence of a polar low. Polar lows are low pressure systems found poleward of the main polar front where polar air meets tropical air around 60 degrees latitude. They last for a few days and have a regional scale matching the scale of the feature that we observe in the ECMWF reanalysis. They generate strong winds and exhibit rotations similar in morphology to a hurricane. In this case a polar low appeared to pass over over the rugged terrain in Greenland where strong winds likely generated orographic GWs.

These wind direction reversals we observe at low altitudes in Figure 7.4 form low altitude critical levels and give us insight into the available horizontal phase speeds of waves that could propagate upwards at different points in time. Since the direction reverses, their existed critical levels at low altitudes for small horizontal phase speeds in both eastward and westward directions.

The most interesting feature of these measurements is the increasing westward velocity at higher altitudes. These wind profiles reach a maximum between 65 and 70 km altitude. GWs with westward horizontal phase speeds near the maximum westward wind velocity would have dissipated at this altitude, generating instabilities and possibly secondary GWs. This supports our hypothesis presented in section 7.3 that the relatively intense and higher frequency temperature perturbations above 70 km altitude resulted from secondary GWs by demonstrating a source that could generate them. GWs with large westward horizontal phase speeds would be allowed to propagate to higher altitudes since the low altitude critical levels would filter only GWs with smaller horizontal phase speeds. However, we would expect such GWs to dissipate due a critical level at the altitude where we observe a transition from larger to smaller scale periodic structures.

7.5 Satellite imaging of PMCs

7.5.1 Science goals

One of our primary science goals for the PMC Turbo experiment is to identify GW dynamics, scales, and intensities that define the character and scales of GW dissipation events. One of the tricky aspects to studying these dynamics is that large-scale features dissipate by cascading through smaller and smaller features. We ultimately hope to understand this process.

PMC Turbo resolves the smallest scale features – down to the inner scale of turbulence. We hope to use complementary measurements to extend to larger scales.

7.5.2 Measurement details

The Cloud Image and Particle Size (CIPS) instrument aboard the NASA Aeronomy of Ice in the Mesosphere (AIM) satellite captures images of PMCs over the poles. Images from this instrument have been used to find expected PMC occurrence by season, and study large scale GW, planetary waves, and tidal studies [14]. We hoped to make coincident measurements between our cloud images and the CIPS cloud images. I describe a few instances of CIPS overlap and the PMC images in this section.

CIPS captures a global scale composite image as it orbits around the pole. However, the spatial resolution of the instrument is two orders of magnitude larger than our instrument as noted in Table 4.1. In contrast, PMC Turbo moves around the pole much slower and our cameras capture a much smaller region of the sky with a higher resolution. We wanted to use these two distinct measurements to investigate relationship between coincident small and large scale dynamics.

During the PMC Turbo flight, the AIM orbit crossed the PMC Turbo location mostly during periods of weak or absent PMCs. However, we did find several coincident measurements in which our instrument recorded PMCs. Figure 7.5 shows the images from these times.

7.5.3 Observations

I mapped the albedo measured by CIPS in panels a through c and plotted the instrument FOV in the known geographic orientation. The PMC data we recorded at the time of CIPS overpasses shown in panels a-c is shown in the same rows in panels d-f.

The CIPS data in 7.5a shows phase structures with horizontal wavelengths around 50 km located 100-200 km north and west of the PMC Turbo FOV. Meanwhile, the data from our imagers in 7.5d reveal features with some periodicity at 10-20 km scales. These features consist of FOV bright PMCs arranged in roughly parallel fronts 10-20 km apart. However, the fronts are not uniform nor

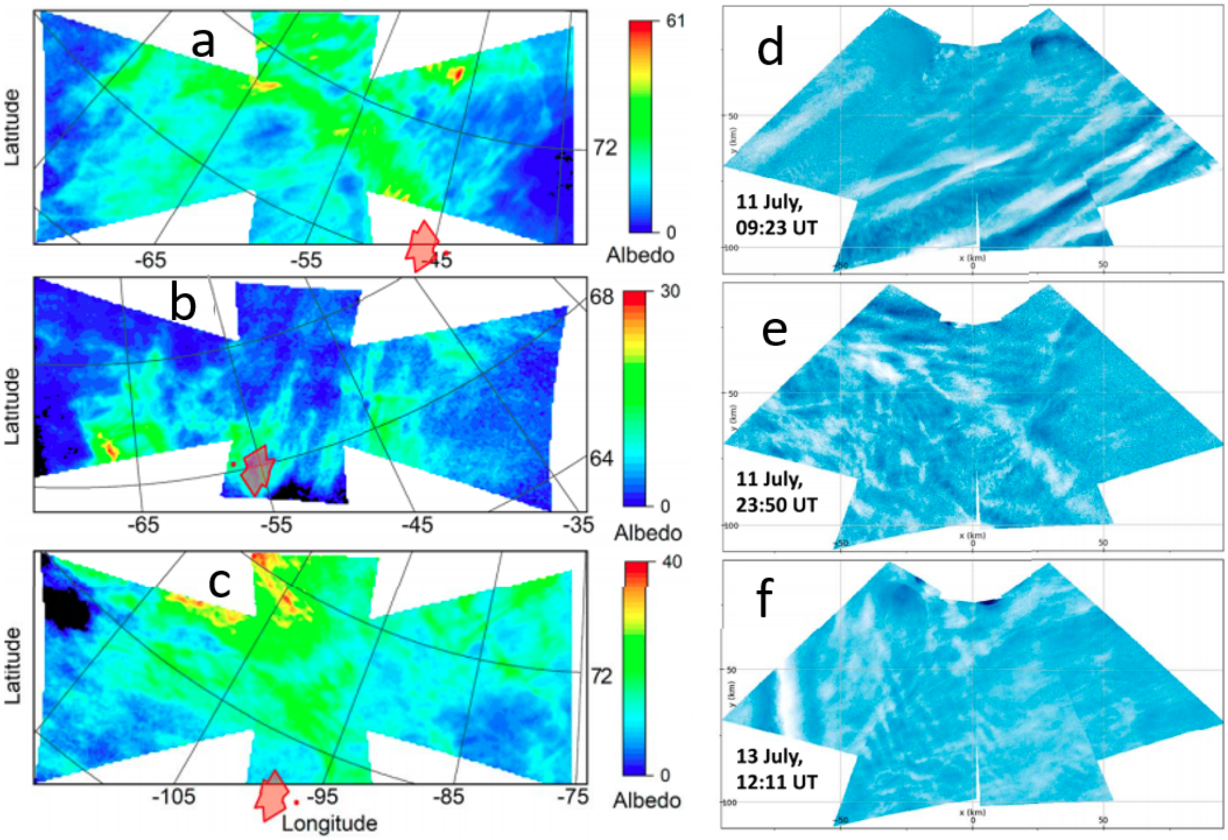

Figure 7.5: Coincident data between CIPS and PMC Turbo. Each row corresponds to one time.

exactly parallel - several converge or intersect. The upper and lower regions of the projected image show smaller-scale features as well superimposed upon the larger periodic features.

Panel 7.5b contains a complicated field, especially in the region of the PMC Turbo FOV. There are evident periodic features with wavelengths running roughly horizontal to the CIPS FOV with a wavelength of 200 km, but these features display jagged edges suggesting a superposition of dynamics of many scales. In our PMC imaging at this time, shown in 7.5d, we likewise see a complicated multiscale field extending to scales of 5 km or less.

Panel 7.5c shows evidence of very large structures with horizontal scales of hundreds of km. Just north of the PMC Turbo FOV location we see smaller fluctuations with scales around 30 km. The PMC Turbo projected image in panel f provides a more detailed view of these smaller structures. Again, we see bright features of a variety of scales including a bright band to the far left of the projected FOV and centrally located crossing fronts spaced at roughly 5 km.

7.5.4 Discussion

The structures we observe with scales of 50 km in Figure 7.5a can be explained as successive GW phase structures with horizontal wavelengths around 50 km. There are several mechanisms by which GWs could make these patterns: the creation of slow temperature perturbations allowing for the sublimation and particulation of PMCs or the large scale movement of PMCs either in the meridional or vertical direction. GWs are the most likely source for these fluctuations due to the absence of other dynamics at the 50 - 100 km scale in the MLT. GWs are also the likely source of the features we observe in our PMC imaging at the same time (Figure 7.5d). The features, at 10-20 km scales, are too large to be KHI at the PMC layer (described in Chapter 8) and too prevalent to be created by mesospheric bores [26]. In the context of the broader CIPS measurements, there seem to be a wide spectrum of GW wavelengths present at this time in the MLT.

Like panel a, the features with scales of 200 km in Panel 7.5b suggest GWs with large wavelengths. However, while these features extend across the CIPS FOV in panel a, they extend across a more limited area in panel b. The jagged edges suggest smaller scale dynamics of 50-100 km also influencing PMC brightness. This is particularly apparent near the PMC Turbo FOV, where a periodic pattern with a horizontal wavelength of 50 km is superimposed on the larger background. The multi-scale dynamics suggests a strong likelihood of instabilities to develop at small scales.

In the PMC Turbo image during this time (7.5e), the chaotic albedo variations suggest GWs with wavelengths of tens to hundreds of km and which would interact strongly with large-scale shears at the PMC altitudes. Therefore, we believe the larger scale features to be GWs with tens of km scales, while the smaller features are instability dynamics rapidly transitioning to turbulence. The lidar data at this time, shown in Figure 7.1 panel c, shows a single PMC layer with large vertical changes on a period of 5-10 minutes. This is consistent with multiscale GWs suggested by the CIPS and PMC Turbo imaging. Disentangling the large scale GWs and the smaller scale instabilities related to GWs is tricky, and we are currently developing analysis methods to more quantitatively analyze events like this.

Following the same reasoning as panels a and b, the features from 7.5c are likely caused by GWs with horizontal wavelengths of 100s of km. The 30 km features north of the PMC Turbo FOV provide some evidence of superpositions of GWs of smaller wavelength, which is supported by the PMC Turbo imaging. In particular, the bright band to the left and the crossed features in the central of the FOV indicate that dynamics of several scales are influencing the PMC brightness. Furthermore, each of these dynamics is aligned independently, which indicates likely propagation in separate directions as propagation direction is orthogonal to the orientation of wave fronts.

Unfortunately, due to the six-day duration of our 2018 flight, PMC Turbo and CIPS did not coincide frequently enough to collect sufficient data for statistical analysis. We hope to investigate this further in the future.

7.6 Meteor radar

7.6.1 Science goals

In addition to studying the sources and propagation of GWs towards the PMC layer, we used complementary data to study the PMC layer. Achieving our primary science objectives requires using PMCs as tracers, and the goal of the measurements presented in this section is understanding those tracer's prevalence.

The occurrence frequency of PMCs during the summer season has been studied extensively. We carefully considered the occurrence frequency of PMCs while planning our experiment's launch window and surveyed previous research on the PMC occurrence frequency by date [47] [8]. PMC Turbo did not fly sufficiently long to contribute to these studies. However, we can use the data collected during the flight to explore PMC occurrence over timescales of hours to days.

During our flight, we observed PMCs about 60% on the time. As we reviewed the lidar data, we noticed that PMCs tended to appear and disappear with a period near 12 hours. This led us to investigate whether the effect could be explained by semi-diurnal tides.

Conditions in the MLT are influenced by tides caused by the sun and moon. The sun influences the conditions by heating the daytime side of the Earth, while the moon influences the MLT through gravitational effects, much as it does the ocean's tides [16]. These periodic influences have a broad spectra ranging from 8 hours to 18.6 years. For this analysis we neglect most of these frequencies as theory and previous experiments have found the most significant effect in the MLT to be the semi-diurnal tide [34] with a period of 12 hours.

The semi-diurnal tide consists of winds with large zonal magnitudes relative to their vertical magnitudes. However, the vertical component of semi-diurnal tide persist over hours resulting in displacement of air on km scales and associated adiabatic cooling/warming. Experimental results from the MaCWAVE campaign indicate that semi-diurnal tide creates temperature fluctuations with an amplitude of 20 K [86]. Sustained temperature changes of this magnitude influence PMC particle formation and sublimation. PMC Turbo flew at the outer edge of the PMC region where temperatures are near those leading to PMC particle sublimation, so temperature fluctuations on the order of 10 K will lead to observable differences in PMC occurrence. Therefore, we predicted that the influences of the semi-diurnal tide resulted in the PMC occurrence and disappearance we observed.

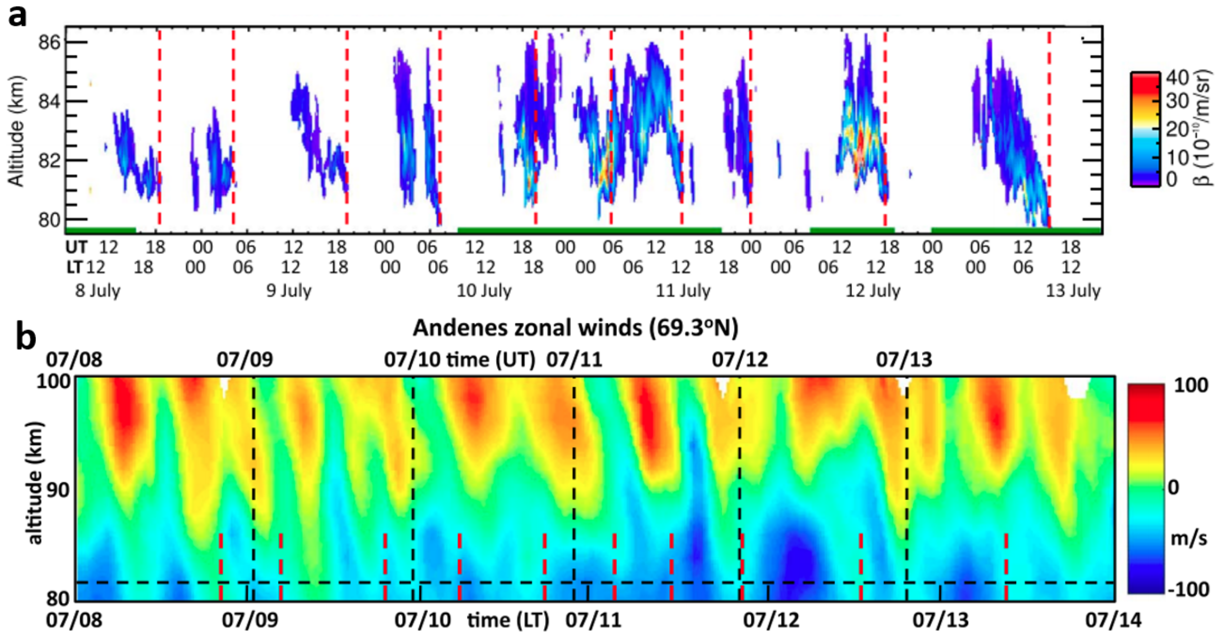

Figure 7.6: Panel a: PMC backscatter profiles measured during the full PMC Turbo flight. Panel b: zonal winds above the Andenes rocket range during the PMC Turbo flight

7.6.2 Measurement details

Meteor radars measure the location of meteor trails to trace ambient winds at 80-100 km altitude. We use zonal wind measurements from a meteor radar located the Arctic Lidar Observatory for Middle Atmosphere Research (ALOMAR), located at the Andøya Space Center in Andenes, Norway (latitude 69.3° N). We apply a low-pass filter to this data when we search for tidal signatures.

Our Rayleigh lidar is the most sensitive measurement of PMCs aboard our gondola. We use the backscatter profiles to determine when PMCs are present above the gondola.

7.6.3 Observations

Figure 7.6 panel a shows the PMC backscatter measured by the Rayleigh lidar for the duration of the PMC Turbo flight. The red dashed lines indicate disappearance of the PMC layer. As one can see, the layer occasionally did not reappear for many hours and occasionally reappeared shortly thereafter - not the length of PMC absence. Figure 7.6 panel b shows zonal winds measured above

ALOMAR during the PMC Turbo flight. ALOMAR is a stationary instrument while PMC Turbo drifted westward. The dashed black lines extending vertically mark UT displayed on the upper x axis, while the tick marks on the lower x axis ark the local time of the balloon during flight. Dashed red lines mark the times of the dashed red lines in panel a. The horizontal dashed black line marks the rough altitude where PMCs reside.

7.6.4 Discussion

There is a periodic component to the zonal wind speeds, and the dominant period does appear to be semi-diurnal, although there are clearly features of other frequencies contributing to the zonal winds. For this analysis, I assume the semi-diurnal influence dominates and neglect other motions, with the intent finding a first-order estimate and comparing to the expected influence based on the MaCWAVE measurements.

We estimate a vertical wavelength of the semi-diurnal tide to be 100 km [27] by using the phase variations with altitude and time and the measured zonal wind speed. The circumference of the the earth around the 69.3° N latitude band and the defined period of the semi-diurnal tide gives us the horizontal wavelength of the features: 7070 km. We know the angle of propagation to be $\theta = \tan(\lambda_h/\lambda_z)$ and using the small angle theorem we find

$$w' \sim u' \frac{\lambda_h}{\lambda_z} \tag{7.3}$$

where w' is the vertical wind, u' is the horizontal wind, λ_h is the horizontal wavelength and λ_z is the vertical wavelength. We find an expected vertical wind speed of 0.2–0.4 m/s, which over the duration of a tidal phase, results in a vertical displacement of 1.4 - 2.8 km and corresponding adiabatic temperature variations of 10-20 K. This matches the temperature variations measured by MaCWAVE. Since these results closely match, our current hypothesis for the appearance of PMCs is that the dominant effect determining PMC sublimation/particulation at the measured latitude is temperature fluctuations caused by the semi-diurnal tide.

7.7 Lessons learned and future plans

We can describe a likely picture of the GW environment during our flight using the complementary data presented in this chapter. From the ECMWF reanalyses we see that weather in the troposphere and stratosphere likely generated orographic and nonorographic GWs with broad spectra. As these waves propagated upwards, many encountered critical levels and dissipated. The temperature perturbations derived from the Rayleigh lidar data and ECMWF vertical wind profiles show us that GWs with large westward phase speeds dissipated just short of the PMC layer, generating shorter wavelength and more intense secondary GWs. We see from backscatter profiles measured by the Rayleigh lidar that these secondary GWs directly influenced the PMCs we viewed by moving the PMC layer vertically and driving instabilities traced by the PMCs. The CIPS images lead us to believe that other GWs of very large wavelength were not filtered and formed of multiscale dynamics through superposition of a broad spectra of GWs and secondary GWs. I will show in Chapter 8 that this hypothesis of the MLT influenced by multiscale dynamics resulting from GW superposition is further supported by observations and analysis of Kelvin-Helmholtz instabilities.

The greatest improvement on these analyses would be to increase the sample size of events we examine. While we have case studies lasting several hours, we do not observe consistent dynamics. In our PMC data we observe such phenomena as mesospheric bores, vortex rings, and Kelvin-Helmholtz instabilities. In our CIPS data we observe fronts indicative of GWs and more complicated fields likely caused by multiscale dynamics. In our lidar data we observe periods of diffuse layers, isolated layers, and multiple bright layers. However, during the PMC Turbo flight we did not observe large numbers of any of these features. As a result, we can develop good hypotheses for our observations, but we encounter challenges quantitatively testing those hypotheses.

The goal of increasing the sample size of specific observed phenomena can be met by numerous balloon flights and longer balloon flights. Implementing these solutions poses logistical challenges. Each balloon-borne experiment requires several years of work for a small team and the utility of balloon-borne experiments to many fields places high demand on limited balloon launch opportunities.

"Piggyback" payloads provide a solution to these challenges. A piggyback payload is an instrument attached to a separate experiment's primary science payload. We have begun to implement piggyback; we attached one of the PMC Turbo cameras to the SuperTIGER payload (a cosmic ray experiment) for a 2019-2020 flight. The benefit of piggybacks is a dramatic reduction in labor and cost. The drawback is that limited power and weight budgets reduce the scope of the experiment. I describe the piggyback in Chapter 9, and we are currently analyzing the data it collected.

Chapter 8: Kelvin-Helmholtz Instabilities

8.1 Overview

A primary science goal of PMC Turbo was to identify the dynamics, scales and intensities of the GWs, instabilities, and turbulence that define the character and scales of GW dissipation events at PMC altitudes. To achieve this goal, we surveyed the data collected by the PMC Turbo flight and searched for evidence of general small-scale GW and instability dynamics traced by the PMC layer. Kelvin-Helmholtz instabilities, or KHI, are one example of these dynamics. KHI presented itself in a dramatic and persuasive manner in multiple cases. We used KHI observations to identify the scales and characteristics, and enable comparisons with models that quantify their implications for the atmosphere and parameterizations of these dynamics.

8.2 Observation and Identification of KHI

Between 13:25 and 13:40 UT on July 12 2018, PMC Turbo imaging exhibited bright striations stretching across much of our composite FOV. The imaging and profiling of this event provided compelling evidence of an extensive and strong KHI event with strong modulations by larger-scale GWs. The extensive analyses of these KHI and their various secondary instabilities comprised the major analysis efforts included in this thesis.

8.2.1 KHI and our science goals

KHI and the turbulence and mixing they induce play major roles in energy dissipation and in defining vertical structure and variability through the atmosphere, oceans, and other stratified and sheared geophysical fluids [64] [67] [89] [90] [92] [83] [84]. KHI and the secondary instabilities generated by KHI play a central role in the dissipation of GWs. Furthermore, the importance of specific KHI events depends on their scales, the environments in which they arise, and the character and intensities of secondary instabilities driving their turbulence transitions. Therefore, energy and momentum deposition of the GWs strongly influences KHI formation and character. Observations and theory addressing KHI dynamics in the atmosphere, oceans, and laboratory have spanned 60 years. The earliest atmospheric study by Witt [88] employed ground-based stereo PMC imaging from northern Sweden in 1958 and described the GW and embedded KHI responses with remarkable accuracy and foresight. Other early observations in the atmosphere, ocean, and laboratory further quantified KHI event evolutions, their dependence on the environmental Richardson and Reynolds numbers, Ri and Re (described in appendices A.2 and A.3), and the various secondary instabilities that arise, several of which were neither identified nor quantified in the atmosphere until much later [12] [69] [79] [80] [81] [91] [92].

More recent atmospheric observations revealed environmental influences on KHI formation and evolution, their causal links to GWs at larger scales, and the dynamics accompanying instabilities driven by KH billow interactions [9] [40] [41] [60] [38]. Broadly speaking, GWs influence KHI in two main ways. Large scale GWs can generate extensive shears resulting in KHI [9][40][84][88]. A review of previous KHI observations also reveals evidence of modulation of the underlying shear from smaller-scale GWs [24] [38] [41] [50] [60], though these were not identified and recognized to be important until MLT imaging resolution improved. Importantly, KHI are now increasingly recognized as an important mechanism by which GWs influence the MLT and one we hoped to identify and analyze with PMC Turbo experimental data.

8.2.2 Image measurement Details

The utility of PMCs to act as sensitive tracers of small-scale GW and instability dynamics in the MLT has long been recognized [88], but previous observations were limited either by the viewing geometry or the seasonal limitations imposed by ground-based observations. PMC Turbo was able to reduce the off-zenith viewing angle, reduce the viewing distance, and had no downtime in imaging due to lack of viewing in full sunlight.

Dynamics occuring in the PMC layer create regions of more and less concentrated ice particles. Regions with a higher density of larger, brighter ice particles reflect more light than regions with a lower density, so we use brightness variations in the images recorded by the PMC Turbo cameras to identify features over time scales sufficiently short to not contribute significant ice sublimation. Furthermore, since we view from below, regions with deeper PMC layers will appear brighter. Our goal was to identify and describe the dynamics that led to variances in ice particle density, so we were generally interested in the relative brightness between regions rather than the absolute brightness measured.

We assume on the timescales we study, PMC brightness in any given volume is conserved following an air parcel (for small vertical excursions) and the PMCs are thus a good tracer of large- and small-scale motions. While GWs and tides cause temperature variations that affect the sublimation and formation of PMC ice particles, KHI dynamics evolve on a sufficiently rapid time scale that the ice particles that make up the PMCs do not sublimate significantly, so they maintain their brightness over short intervals. As described in section 7.6, temperature fluctuations from tides have timescales with periods of 8 hours or greater, while the dynamics we observe persist for minutes. Tidally-induced temperature variations are therefore not significant on the timescales examined in this chapter.

8.2.3 Image Observations

The KHI dynamics discussed in this chapter were observed on 12 July 2018 when PMC Turbo was located above Baffin Island, Canada near 68° N, 72° W. During this time, strong periodic variations in brightness were widespread in the PMC layer across a 50 x 50 km section of the sky, particularly from 13:25 to 13:35 UTC. Figure 8.1 shows the PMC layer at one instance during the ongoing event. The brightness variations extend across most of the left and central regions of Figure 8.1. These features persisted for tens of minutes. Recall that we captured images with a 2 second cadence, and by tracking individual phase fronts over a series of images, we found these features generally advected from Southeast to Northwest at about 75 m/s and were oriented around

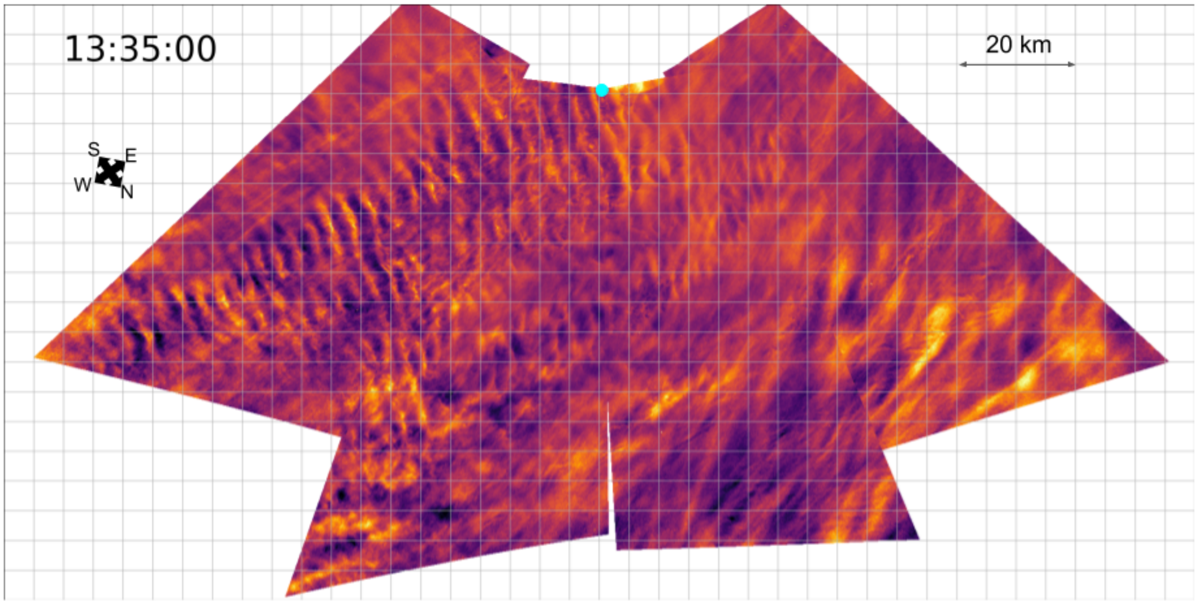

Figure 8.1: Projected images from the four wide FOV cameras on board the PMC Turbo instrument. Images were obtained at 13:35:00 UTC, at 68°N, 72°W. The images have been projected as if viewed from below. The cyan dot indicates the approximate location of the Rayleigh lidar beam. The color scale of this image is linear, and ranges from purple to yellow with increasing brightness. Kelvin-Helmholtz instabilities span much of the left half of the FOV.

45 degrees to this advection.

These periodic structures exhibited fluctuations that were coherent in time, have a mean wavelength of about 5 km, and were identified as KH billows because of their evolution in time, and the small-scale features revealing secondary instabilities seen in modeling of these dynamics.

8.2.4 Lidar measurement details

Lidar backscatter profiles were employed to identify and measure the KH billows. The PMCs are highly reflective in the emitted wavelength of the lidar. The light scattered back to the lidar telescope is time-binned as it is received, so the lidar analysts derive the brightness of the PMCs as a function of distance from the lidar.

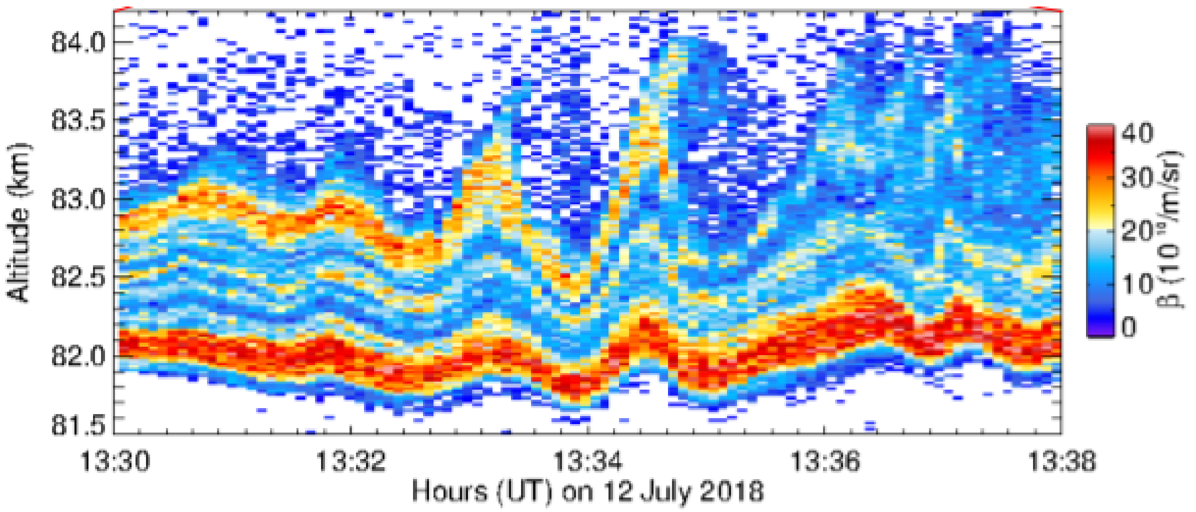

Figure 8.2: Lidar backscatter profiles during the period of strong KHI

8.2.5 Lidar observations

Figure 8.2 shows near-vertical lidar profiling of the PMC layer between 13:30 and 13:38 UTC at 20 m and 5 second resolution. Recall that the location of the lidar beam is shown on Figure 8.1 as a cyan dot at the central top region of the FOV and that we observed sequential fronts of the KHI move through the location of the lidar beam due to the horizontal advection from Southeast to Northwest at ~75 m/s. As several billows move through the beam, we observe vertical motions of the PMC layer with 1-1.5 minute periods traced in a fine-scale, multiply-layered PMC. Unfortunately, while the KHI persisted in the PMC widefield FOVs for some 15 minutes, only these few billows advected through the lidar beam. We see that the deepest billow passing through the lidar beam from 13:34-13:36 UTC exhibits a lower edge at 82.3 km and an upper edge at 84 km, hence a billow depth of ~1.7 km.

8.2.6 Confirmation of KHI Character

The term "Kelvin-Helmholtz Instability" describes the class of instabilities that occurs at a shear layer. This can occur in a single fluid with a velocity shear or with a velocity shear at the interface between two liquids. This causes fluids from each layer to be perturbed vertically and "roll up". Figure 8.3 shows an example of this process from an early theory paper. A common

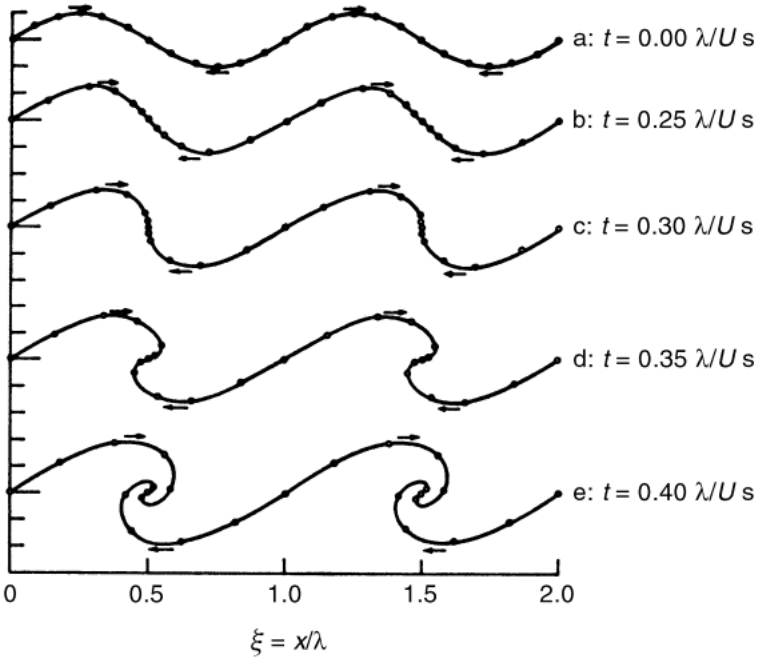

Figure 8.3: A vortex sheet rolling up as a function of dimensionless time and distance. From "The formation of vortices from a surface discontinuity" [65] [56]

Figure 8.4: Kelvin-Helmholtz instability in stratospheric clouds (1-5 km)

example of KHI are the waves that form on bodies of water as wind blows over the surface. This process is common in other geophysical fluids; Figure 8.4 shows stratospheric clouds tracing KHI.

We have several reasons the believe the features we observe are caused by KHI. The most compelling evidence comes from our lidar traces. The two large vertical features shown in 8.2 at 13:33 and 13:35 occur as two of the bright periodic bands pass through the lidar beam. The top of these two vertical features shows the same "curl" as the KHI shown in Figure 8.3 and Figure 8.4 between 83.5 km and 84 km altitude. We observe that the PMCs have several brighter and fainter layers at this time period. The top PMC layers show the largest vertical excursions while the lowest layers move the least, suggesting that the bright PMC layers occur below the primary shear layer leading to KHI. We only observe the faint "curl" at the very top of the PMC layer during both these vertical excursions. This is also consistent with KHI located near the top of the PMC layer.

The KHI entrained ice particles from the PMC layer and so we see the "back" of the characteristic wave shape traced in the lidar profiles. Figure 8.4 shows this same process when KHI entrains tropospheric clouds.

The lidar profiles explain why we see periodic bright and dark regions in the PMC imaging. The left side of the KHI in Figure 8.4 entrain air with high particle density and move it upwards and rightwards. The result is vertically-stacked regions of high particle density on the left side of the KHI. The right side of the KHI does the opposite: it entrains air from above the PMC layer (with few ice particles) and moves it downwards and leftwards. The regions of high vertically integrated PMC particle density are much more reflective and brighter. The consequences are brighter leading (rising) edges, darker trailing (descending) edges, and peak PMC brightness shifted toward the leading edges of the KH billows. The periodic brightness fluctuations we observe in PMC images such as Figure 8.1 are the successive leading and trailing edges of KHI extending across much of our FOV.

Our PMC images confirm the identity of these features as KHI. We observe the leading and trailing edges of the KHI exhibit undulations and mis-alignments along their axes as well as evidence of secondary instabilities. These instabilities are of considerable scientific interest, and I describe them in depth in section 8.3. These features are consistent with instabilities manifesting in KHI in laboratory flows and numerical modelling [78] [83] [24]. Furthermore, the only other periodic features that could account for similar observed spatial scales and phase structures cannot account for their morphology; small-scale ducted GWs can create periodic fluctuations in the MLT, but the misalignments we observe are not consistent with ducted GWs.

8.3 Observation and Identification of Secondary Instabilities

8.3.1 Background

Secondary instabilities in finite-amplitude KH billows have been observed in the atmosphere and laboratory for over six decades, and they exhibit a wide diversity of forms, several of which have been quantified only recently [9] [11] [13] [41] [68] [79] [80] [81] [78] [83] [84] [88]. They depend closely on ambient atmospheric conditions quantified by Re and Ri that are modulated by GWs, and their breakdown represents the final stages in energy dissipation.

At low Re, the only apparent instabilities of spanwise-uniform individual KH billows are longitudinal convective rolls aligned along the shear having large spanwise and temporal scales [48] [58] [57]. These scales decrease and the convective rolls occur nearer the outer edges of the billows with increasing Re and decreasing Ri [83] [85] [28] [24]. Secondary KHI arising in the stratified braids between adjacent billows were seen previously in the laboratory and in more recent high-resolution modeling at higher Re and low Ri [24] [27] [83].

Other instabilities arise where larger-scale motions cause inhomogeneities in the underlying shears inducing KHI. Where KH billow axes are nearly continuous but billow cores exhibit variable rotation rates or spatial modulation, KH billows and vortex tubes arising becuase of these misalignments precede twist waves, which can act to fragment the billow cores thereafter [6] [9] [77]. Where such perturbations yield close spacings between adjacent billows, they can also lead to local vortex pairing [83]. Such modulations are widespread in KHI observations [40] [41] and suggest that these dynamics are likely to contribute to KHI breakdown and turbulence in general shear flows influenced by GW motions.

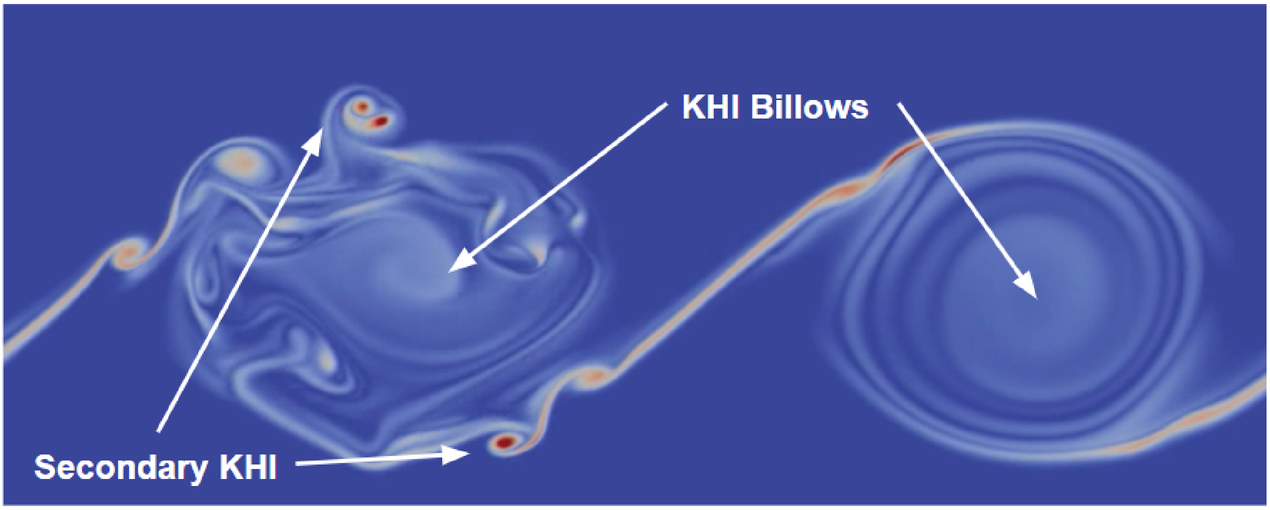

Figure 8.5: Simulated KHI billows showing secondary KHI

Also seen in this study, are among the only identified cases of tubes and knots arising from the interactions among adjacent KH billows having small *Ri* and large *Re* and resolved by imaging of thin layers in the MLT. These dynamics have only been observed in one other observation in OH airglow [38]. As with other instabilities discussed in this section, tubes and knots were seen in early laboratory shear flows [83] and argued by Thorpe 2002, especially Figure 12 [84] to be expected and widespread in the atmosphere as well. PMC Turbo imaging offers a unique perspective on these dynamics because of its ability to define the evolution of very thin layers revealing very small features continuously in time for KHI events having much larger initial scales. The simulations and laboratory studies of these predict that these tubes and knots exhibit dramatically higher energy dissipation rates than the secondary convective instabilities and KHI within individual KH billows.

8.3.2 Secondary KHI

Secondary KHI form on the strongly-sheared layers between adjacent KH billows and advect around the rotating primary billows. Figure 8.5 shows a simulated example of KHI including secondary KHI forming on the left billow. Secondary KHI have significantly smaller spatial scales than the primary KH billow because their wavelengths and depths are dictated by the much thinner intensified vorticity sheets between the primary billows (e.g., $\lambda_h \sim 4\pi h$, for h the half-depth of the intensified vorticity sheets and λ_h the horizontal wavelength). Secondary KHI are also expected and observed to be oriented largely parallel to the primary KH billows and to exhibit significant horizontal extents along the primary KH billows because the vorticity sheets that provide their sources have vorticity largely aligned with the primary billows.

Without considering the PMC brightness gradient, we would expect secondary KHI at any position around the primary KHI. However, we expect to observe them preferentially above and below the billow core, where the contrast is higher. However, the KHI layer we observe is located above the maximum brightness in the PMC brightness gradient. Therefore, we anticipate ascending secondary KHI advecting over the bright upwelling region. Since this region is already bright, the ascending secondary KHI does not appreciably change the brightness. Conversely, the descending secondary KHI advecting upstream occurs over the light bright descending region under the upstream KH billow, and we do anticipate an appreciable decrease in brightness and leftward advection. Our observations match these predictions.

During several periods of intense KHI, dark features are observed within the brighter leading edges of KH billows. Figure 8.6 highlights one instance of dark structures apparent within primary KH billow leading edges at 13:30:40. Figure 8.7 follows the evolution of the same structures within the billow edge highlighted in this Figure 8.6 with a cyan circle. The KHI moves toward the bottom and left of the image (to the Northwest). These small features are largely parallel to the KH billow cores and move past the billow edges over the course of a few minutes. Their scales (hundreds of meters) are much smaller than the KH billow wavelengths.

The dark structures within the KH billow edges develop from 13:27 to 13:34 UTC. Figure 8.6 shows a 25 km x 15 km area of the FOV and exhibits several KH billows, each of which includes the formation of the dark structures.

Figure 8.7 tracks the evolution of dark features present within the leading edge of a KH billow from 13:29:00 to 13:31:30. Note that the dark feature advects through the billow. The billow of interest is highlighted in Figure 8.2. The KH billow is tracked within a 5 km x 10 km FOV as it moves through the FOV with an apparent motion of 75 m/s northwestward.

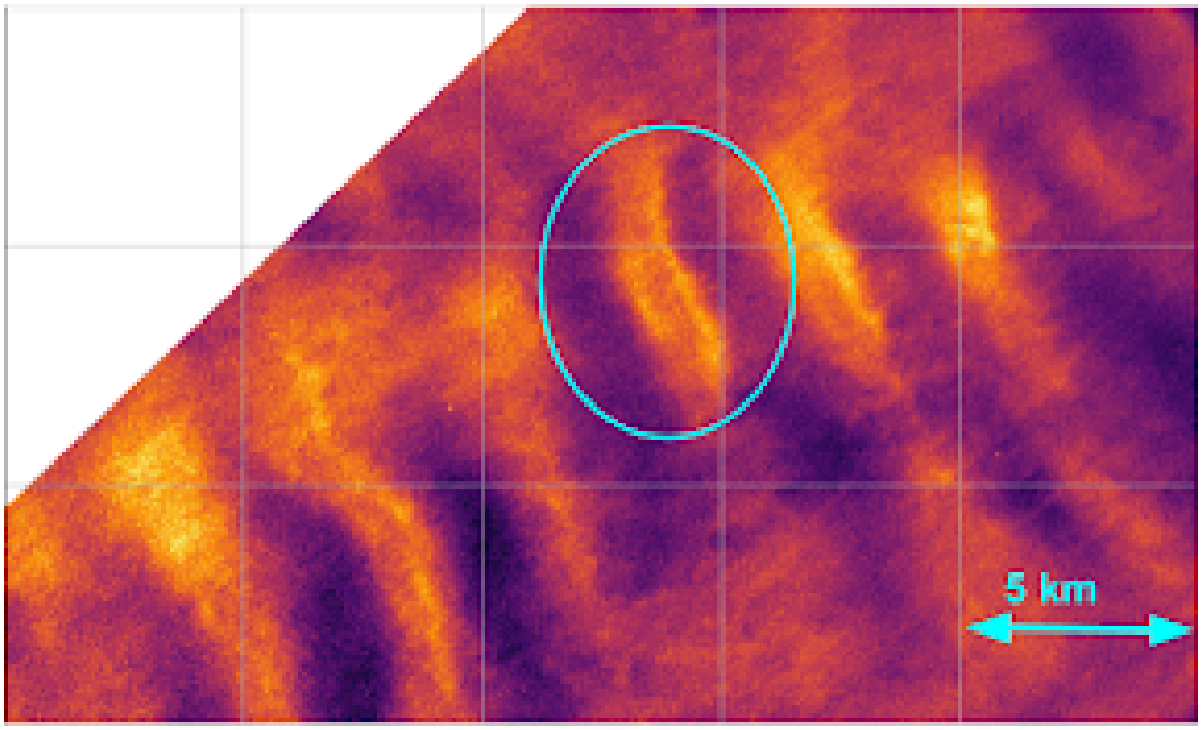

Figure 8.6: Secondary KHI manifesting on the fringes of primary KHI. One prominent example is highlighted.

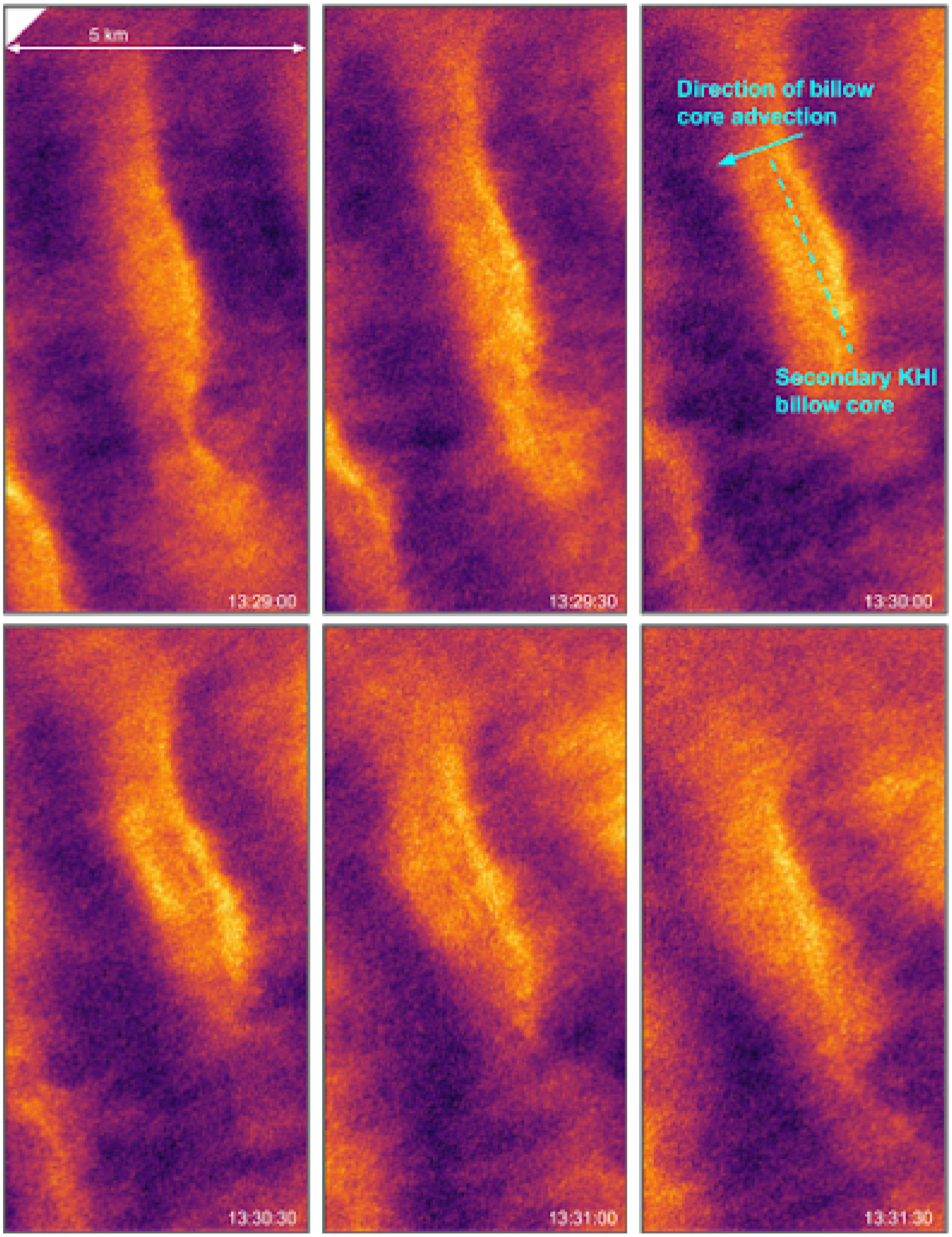

Figure 8.7: Tracking one secondary KH billow

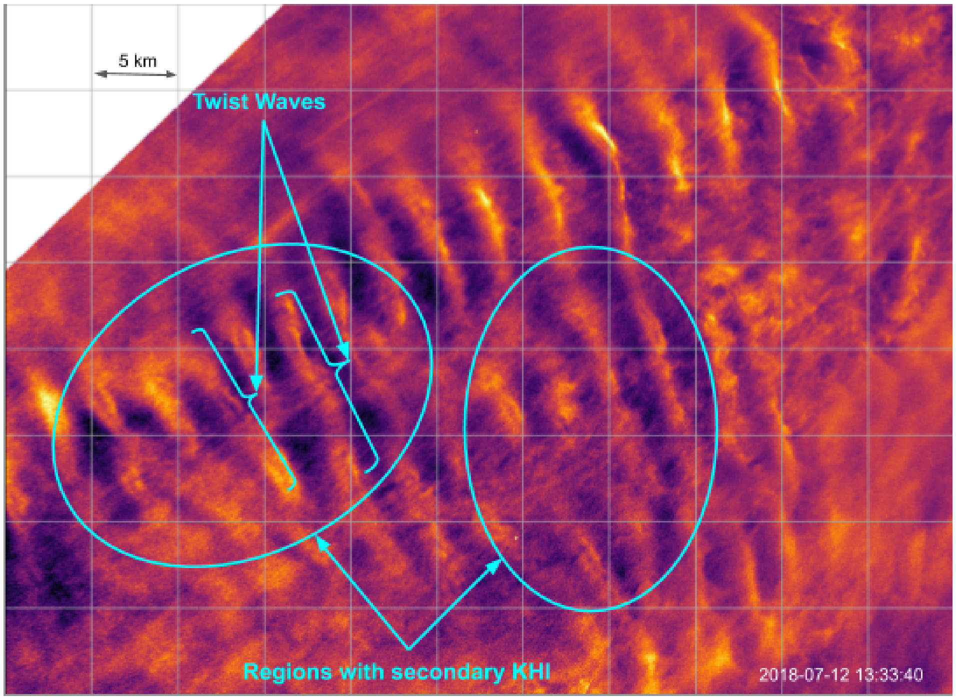

Figure 8.8: Secondary KHI and twist waves apparent within a broader KHI field

The panels of Figure 8.7 follow the development and motion of one of the dark features relative to a single KH billow as it advects across the sky. In the top left panel, the dark features are not yet visible within the KH billow edge. In panels 2-5, the feature is visible and moves from upstream (right) to downstream (left). The movement of the dark feature is consistent with the air motion due to the primary KH billow core. By the final panel, the feature is no longer visible and has either moved past the edge or dissipated.

We find no other plausible dynamics that explain the systematic formation of dark features parallel to primary KH billows having much smaller widths, Hence, we conclude that the narrow, dark features aligned along the primary KH billow axes must be secondary KHI.

Secondary KHI is also observed in images from 13:33 to 13:37, several of which are shown in Figures 8.8 and 8.9. Figure 8.8, captured at 13:33:40, shows a larger scale view of secondary KHI forming on almost every KH billow across the total field of view. I have marked regions with secondary KHI and individual twist waves. Note the large-scale modulation of the KHI intensity.

The secondary KHI at this time is more widespread across the region of intense KHI. It is

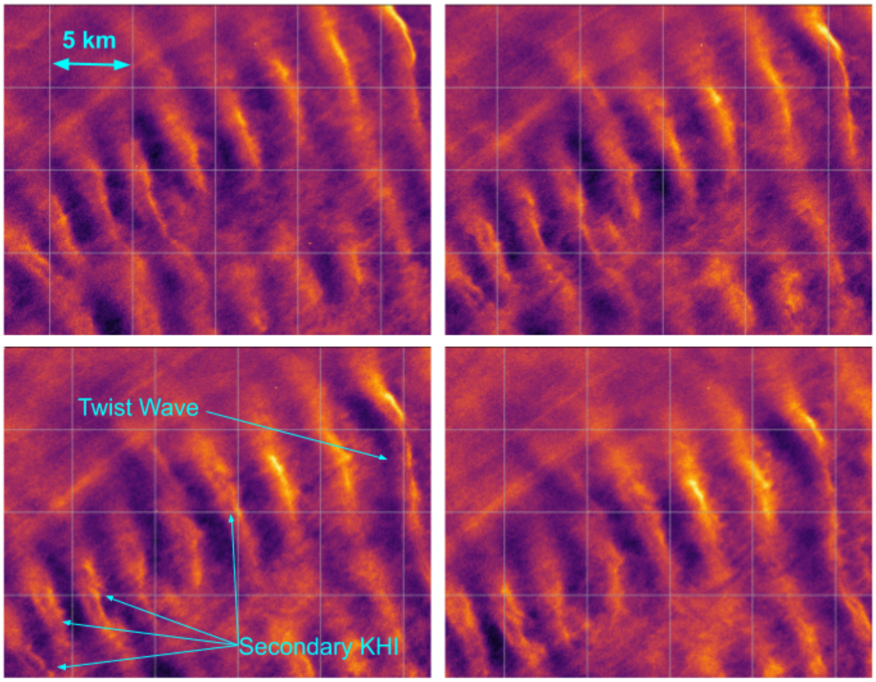

Figure 8.9: Tracking secondary KHI and twist waves in a region

common in our observations that a secondary KH billow progresses at different rates along the secondary KH billow core axis. While these events are nearly contemporaneous to the events shown in figures 8.6 and 8.7, they occur some 40 km away. We also observe KH billows undulating in the x-y plane along the billow core axis, which is consistent with the behavior of twist waves seen to occur alongside secondary KHI in the laboratory and in models.

Figure 8.9 shows a more closely zoomed region at 13:33:10, 13:33:30, 13:33:50, and 13:34:10. We continue to observe numerous examples of secondary KHI, twist waves. In Figure 8.9, the secondary KHI aligned along the billow is seen to advect around the primary KH billow at rates varying along the axis of the secondary billow. Several secondary KH billows demonstrating this behavior are noted in the third panel of Figure 8.9. The differential progression of the secondary KHI along the primary KH billow axis must be a result of differential primary KH billow rotation along the length of the billow core. This implies high background turbulence influencing the KHI dynamics.

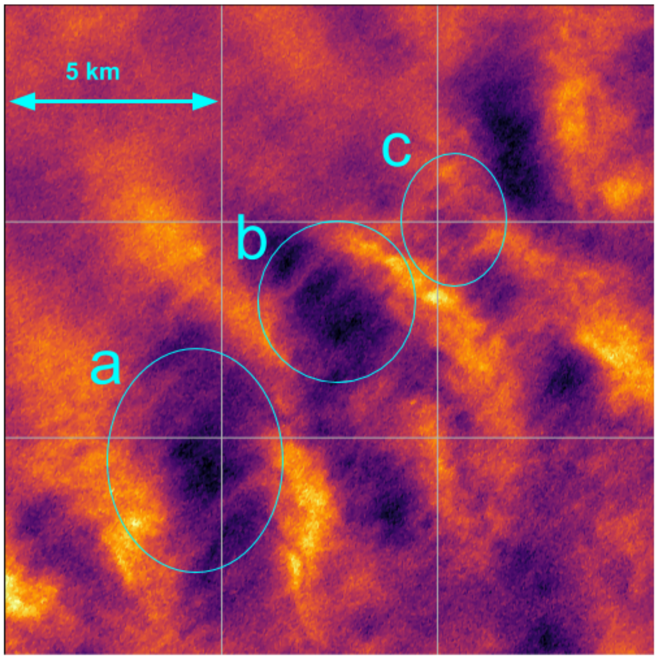

Figure 8.10: KHI demonstrating convective instabilities

8.3.3 Convective instability rolls associated with KHI

Figure 8.10 shows a 15 x 15 km projected section of the sky at 13:35:50 UTC. Highlighted regions show numerous filaments believed to be convective instabilities within successive KH billow cores. The cyan circles labelled “a” and “b” in Figure 8.10 highlight two regions with relatively brighter PMCs due to upward advection by the KH billows at their leading edges, as discussed in section 8.2.6. The filaments in Figure 8.10 extend lengthwise across the billow cores (about 5 km) but do not extend into the regions between adjacent billows. This extent indicates that they arise at the outer edges of the billows.

The dynamics and morphology of these filaments are consistent with convective rolls. Convective rolls become visible because they occur where there is a strong vertical gradient in PMC brightness and differential vertical advection between adjacent rolls yield variable brightness across the convective rolls when viewed from below, as modeled by Fritts et al. [28]. It is clear from our lidar traces in Figure 8.2 that the PMCs we examine in this chapter do have a strong vertical gradient in brightness. The filaments are observed to form perpendicular to KH billows, which is consistent

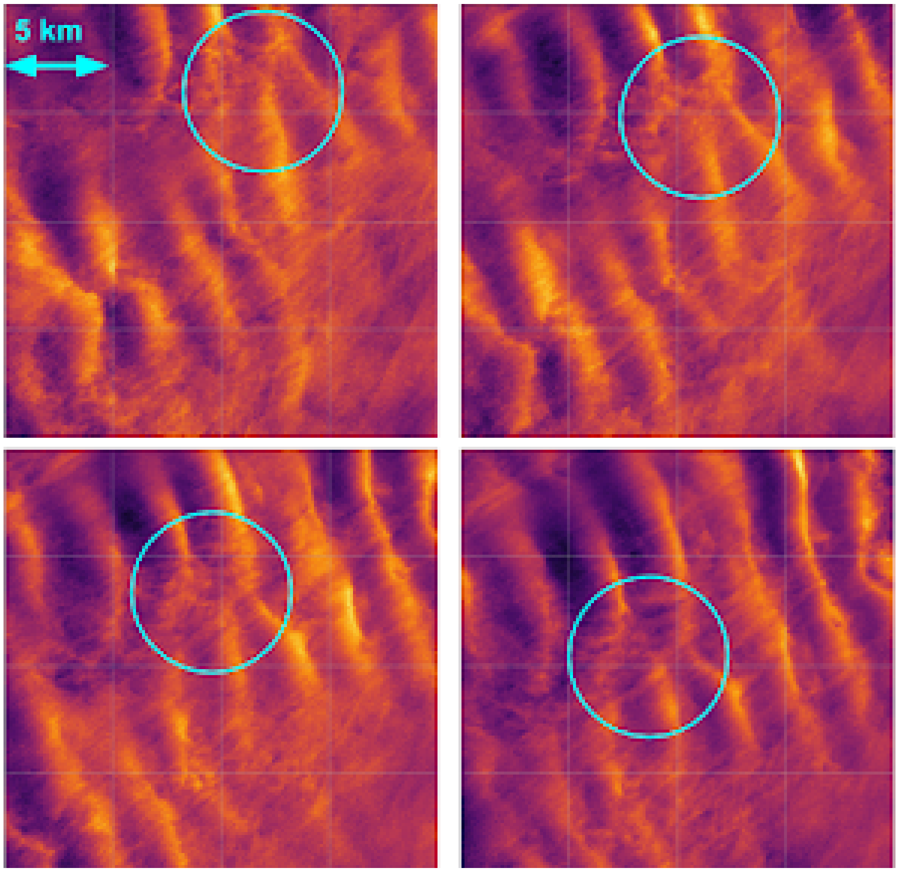

Figure 8.11: KH billow interactions over time

with both models and other observations.

8.3.4 Tubes and Knots

During the periods of intense KHI examined in this paper, we observed numerous apparent KH billow interactions. One example is shown in Figure 8.11. The panels of this figure show the evolution of a 20 km by 20 km section of the sky at the PMC layer. The timestamps from up-down to left-to-right are 13:28:50, 13:29:20, 13:29:50, and 13:30:20 UTC.

In the top left panel, there are two KH billow cores that appear to be interacting strongly. The location of the billow interaction is highlighted with the cyan circle in each panel. The interacting billows advect across the FOV over the course of two minutes. Initially, the rightmost billow largely disappears, traced by the meeting of the surrounding billow edges in a chevron pattern. In the upper left (13:28:50) panel, we see evidence of interaction with the left billow: near the point

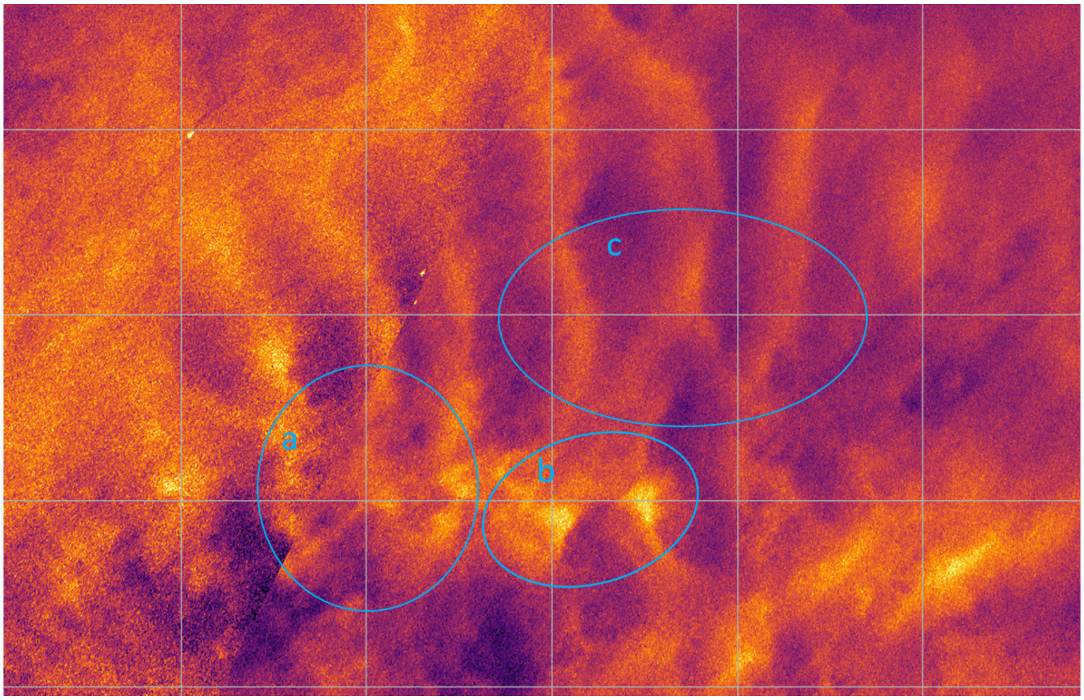

Figure 8.12: Characteristic "W" and "Z" patterns in billow interactions

where the two billows interact, there are complex features evolving into small-scale turbulence. Two brighter streaks connect the leftmost billow edge to the center edge and the right edge.

In the top right panel, at 13:29:20, the sharp edges of the billows on the left side of the right billow evolve from a firm boundary to become more diffuse. Both the left and right billow terminate, and the turbulence intensifies. While the turbulent features were initially localized to the region of billow interaction, by 13:29:20, turbulence features have extended several kilometers away from the merging point along the billow axes. In the lower right panel, at 13:30:20, the left billow develops along the right side, reminiscent of the terminating edge of the right billow at 13:28:50. The right billow core becomes more continuous, although a kink forms near the location of the original billow termination. At the end of the event shown in Figure 8.11, remnants of the turbulence exist throughout the merging billows but the turbulence is less intense and many of the remaining features are more ubiquitous convective instabilities.

Figure 8.12 contains multiple apparent interactions between billows along with knots and other instabilities at 13:29:10 UTC. “Z” and “W” patterns are apparent in regions “a” and “c” of Figure

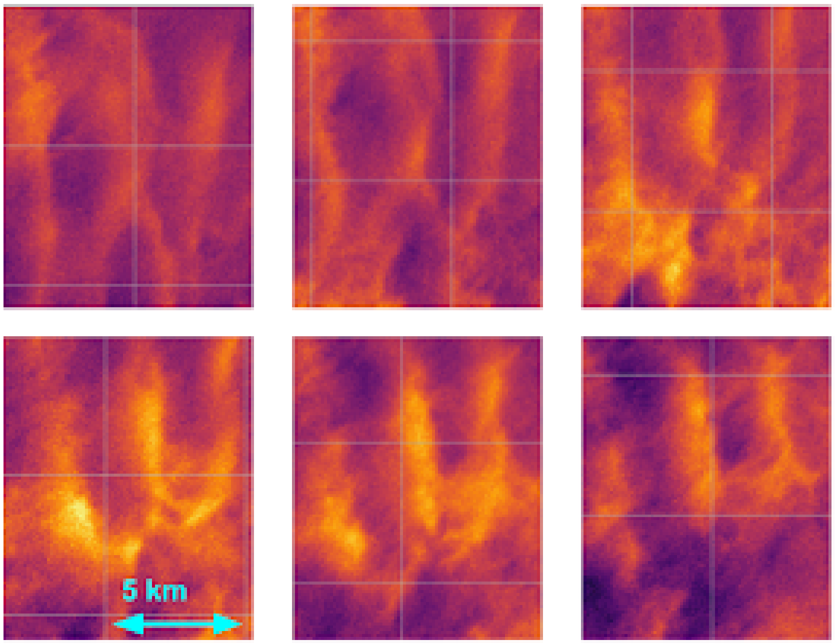

Figure 8.13: Evolution of "W" pattern of merging billows

8.12 in which billows are not parallel and instead converge. In region “b” we see several billows interacting and forming a region of strong turbulence.

A localized region of interest is examined over several minutes in Figure 8.13. Figure 8.13 shows the evolution of a “W” pattern similar to the billow interaction imaged in Figure 8.11. I track the evolution of one KH billow interaction from 13:28:40 - 13:31:40 UTC at a 30s cadence. However, while the billows in Figure 8.11 first terminate, but become more continuous, the interacting billows in Figure 8.13 become less cohesive. At 13:28:40 UTC, the billows are well-defined, but 30 seconds later turbulence has formed between them. At 13:29:40 UTC, turbulent structures continue to develop. Brighter regions of PMCs connect the fraying edges of the KH billows. There is more widespread turbulence present as well suggesting that knots are breaking down into smaller scale turbulence. The following 2 minutes continue the trend towards turbulence, and by the final set of billows shown at 13:31:40 UTC the billow cores are no longer coherent.

8.4 Evidence of Gravity Wave Background

As discussed in section 7.2, larger-scale GW signatures with periods from ~15 minutes to an hour or more are visible in the highly variable PMC layer. The larger excursions at lower and higher altitudes accompany GWs having observed periods of 2 hr and longer. Additional GWs having observed periods of ~10 minutes to 1 hr contributed smaller displacements throughout the PMC layer. This gives us context for our observations between 13:25 and 13:40 and suggests that a multiscale background due to the superposition of GWs modulates KH billow Re and Ri.

As noted in section 8.2.3 coherence is not uniform across the image, and the regions of increased and decreased coherence apparent in the KHI field have scales of ~15-45 km. GWs with corresponding wavelengths could have modulated the background shear layer that spawned the KHI, or modulated Re and Ri resulting in instabilities influencing the KHI coherence to different degrees. However, it is not obvious that GWs caused these modulations as thinning or stretching of the shear layer could also be the source of variations in Re and Ri.

Unfortunately, when we applied filters to our image to isolate the corresponding spatial scales, we found a complex background. We were able to find multiple motions, but we have not yet been able to distinguish individual GWs from the multi-scale background. One of our ongoing areas of study is the better identification and isolation of individual GWs within the multi-scale background and we have published a paper identifying and quantifying GW breaking observed at a different time during flight [32].

Our observations of convective instabilities support our assessment of the GW background. In Figure 8.10 the spatial scales and intensities of convective instabilities are not uniform along the length of the billow cores. We attribute this to inhomogeneities in the initial shear layer, and the multiscale background which caused variations in Ri and Re along the billow axes at the time of KHI initiation. Their timescales are likewise dependent on initial conditions and their intensities, but they appear to remain coherent for ~2-3 minutes prior to exhibiting a transition to smaller-scale turbulence.

8.5 Reynolds Number

8.5.1 Science Goals

The Reynolds number, denoted Re, represents a ratio between inertial to viscous forces for specific dynamical features (see appendix A.3). The mathematical expression depends on the geometry of the flow. For KHI Re is:

$$Re = \frac{U_0 h}{\nu} \tag{8.1}$$

where U_0 is half the horizontal velocity difference of the shear layer giving rise to the KHI, h is the half depth of the shear layer, and ν is the background kinematic viscosity. Viscosity tends to inhibit turbulent motion. Low Re represents dominant viscous forces and predicts laminar flow of fluid motion. High Re represents dominant inertial forces more likely to yield turbulent motion.

To achieve our science objectives we need to understand GW influences on local KHI evolutions. The scales, intensities and evolution of these dynamics depend on Re. Additionally, we employ direct numerical simulations based on observed dynamics. We need to use a realistic Re for these dynamics, so we obtain an estimated Re from our observations.

In this section I make a rough estimate of Re from the PMC images and complementary lidar data using two methods. First, I estimate the Re from imaging secondary instabilities. I check this estimate from the measured horizontal wavelength of the KHI and the billow depth.

8.5.2 Estimating Re with KHI wavelength and billow depth

We can make a rough estimate of the Re from our images and lidar profiles. We use the wavelength and billow depth in our observations to find U_0 and h and estimate ν from the altitude of the PMC layer.

From theory, observations, and modelling an approximate relationship between h and the horizontal wavelength of KHI λ_h is

$$\lambda_h \approx 4\pi h \tag{8.2}$$

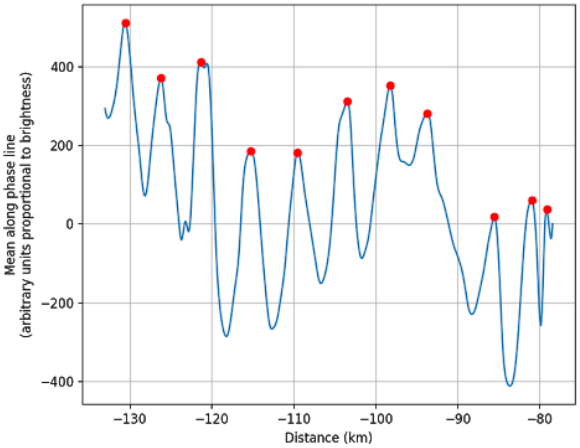

Figure 8.14: Mean pixel value across KHI phase lines

We can estimate U_0 from Ri and h. We can include the Richardson number Ri by using the definition given in Appendix A.2 equation A.41 and noting that in this case, the change in horizontal velocity with height $du/dz = U_0/h$. We find

$$Ri = \frac{N^2}{(U_0/h)^2} \tag{8.3}$$

At the surface of the earth, the kinematic viscosity $\nu_0 = 1.8x10^{-5}m^2/s$. Kinematic viscosity scales with the inverse of fluid density. Therefore, it increases $\sim 10^5$ from ν_0 at the altitude where we image PMCs and we assume $\nu_0 = 1.8m^2/s$. From previous observations we assume a maximum shear layer $N_{max} = 0.028s^{-1}$.

The KH billows merge and show secondary instabilities that evolve with time. These secondary instabilities perturb the billows horizontally and obfuscate the horizontal KHI wavelength. Several secondary instabilities are highly dependent on Re, and we use them to verify our estimates in section 8.5.3. However, despite uncertainties, we estimate Re from KHI wavelength. I defined the "most parallel" direction as the direction in which the brightness variance averaged along the KH billow phases is highest. To find this direction, I selected images showing bright KHI and I found the "spanwise average" as a function of direction. To find the spanwise average, I chose a direction, and found the average pixel value in binned lines perpendicular to that direction. For example, for the horizontal direction, the "spanwise average" would be the average value for each vertical column of pixels. For the direction with the highest variance, I found the wavelength by measuring the distance between peaks and taking the mean (and standard deviation) of those distances. Figure 8.14 shows the mean pixel value across the phase lines of one image. The peaks are highlighted with red dots, and their locations are used to measure the wavelength of the KHI. Across a selection of images from the duration of the KHI event, I found the wavelength to be 5.2 +/- 2.5 km. The measurement isn't precise. As discussed in 8.4, we expect Re to be modulated across the FOV. From equation 8.2, we find $h \sim 400m$.

As described in section 8.2.5, from our lidar traces in Figure 8.2, we find a billow depth of ~1.7km. We observe a ratio of depth to GW horizontal wavelength λ_h to be ~ 0.32. This implies $Ri \sim 0.1$ at the location of the lidar beam, based on laboratory studies [80] [81]. From Ri, we estimate the half the horizontal velocity difference of the shear layer U_0.

$$Ri = \frac{N^2}{(U_0/h)^2} \tag{8.4}$$

$$\frac{U_0}{h} = \sqrt{10}N \tag{8.5}$$

$$U_0 \sim 35m/s \tag{8.6}$$

From our estimates of U_0, h, and ν and equation 8.1 we find a rough estimate of

$$Re = \frac{U_0 h}{\nu} \sim 7900 \pm 3800 \tag{8.7}$$

However, referring to the PMC combined FOV image in Figure 8.1 at this time we see that the KHI were clearly less intense at the location of the lidar profiling than at the sites of strongest KHI dynamics $\sim\ 30 - 50$ km farther off-zenith to the lower left that are our analysis foci in this chapter. These apparent KHI intensity differences suggest significantly stronger KHI, deeper billows yielding larger brightness contrast across their phases, stronger shears, and smaller initial Ri by a factor of 2-3 times at our analysis sites [81]. This estimate is important since many of the dynamics discussed shortly in this analysis are located in the central region of the FOV, rather than where the lidar beam is located. For $Ri = 0.03$, we estimate $U \sim 61 m/s$ and $Re \sim 13600 \pm 6500$.

8.5.3 Estimating Re with Secondary Instabilities

As shown in section 8.3, we observed secondary KHI, convective instabilities, and twist waves. We would expect this - both billow interactions via tubes and knots and these other instabilities arise at the Re estimated above. The small-scale convective instabilities we observe within KH billows require $Re > 1000$. Secondary KHI in the braids between adjacent KH billows implies $Re \sim 4000$ or larger, based on the determination of the needed Re allowing secondary KHI for $Ri = 0.1$ by modelling results (Fritts et al., submitted 2021: Multi-Scale Kelvin-Helmholtz Instability Dynamics Observed by PMC Turbo on 12 July 2018: 2. Modeling KHI Dynamics and PMC Responses).

However, we observed convective instability scales of $\sim$ 500 meters or somewhat larger, suggesting a lower Re - a maximum of 5000. We can explain this discrepancy with a heightened kinematic viscosity due to turbulence. Turbulence within a fluid suppresses evolution of other dynamics and can be described with the turbulent kinematic viscosity ν_{turb}. From ν_{turb}, we define $Re_{turb} = \frac{Uh}{\nu_{turb}}$. Since the secondary KHI places a lower bound on Re, we estimate Re_{turb} to be $\sim 4000 - 5000$, and ν_{turb} to be $\sim 1.6 - 3.4$ times larger than ν (depending on our estimate of Ri), although $Re = 5000$ falls within the uncertainty for $Ri = 0.1$.

8.6 Energy Dissipation Rate

8.6.1 Science goals

Tubes and knots were seen in laboratory shear flow experiments in the 1970's and 1980's [83] and are expected to be widespread in the atmosphere as well [84]. While these secondary instabilities had been observed in laboratory experiments, theory, and modelling, they have only been observed in nature by one other contemporary experiment [38]. These dynamics result in elevated energy dissipation rate ϵ compared to ϵ due to KHI alone [30]. This elevated ϵ has important implications for our understanding of the roles of KHI within the MLT and other geophysical fluids. Previous analyses of KHI billows did not reveal billow interactions, but they did reveal misalignments and discontinuous billows [9] [40] [38] [28]. These observations suggest that billow interactions may be the norm in regions of KHI and our understanding of ϵ of KHI fields needs to account for the heightened levels associated with these instabilities. Other studies have found evidence for sustained KHI driving tube and knot dynamics in the lower atmosphere and ocean [45] [44] [49]. These billow dynamics could explain a discrepancy in the mixing predicted by models [31] [51] [84] and the mixing that has been observed.

8.6.2 Model details

In this study, we aimed to confirm our identification of billow interactions via tubes and knots, assess the magnitude of ϵ using simulations, and verify the simulation by comparing model results to observations. I am not an expert in the modelling, so I describe the modelling performed at a high level and summarize the results in the following section.

We do not have the experimental capability to directly measure the energy dissipation rate ϵ. The best methodology we have found to infer and interpret physical results is comparing our observations to direct numerical simulations (DNS), confirming that these models approximate our observations, and inferring ϵ in our observations from the model results.

Our modelling team used the Spectral Atmosphere Model (SAM) to simulate multiple interacting KH billows. This model allowed phases and wavelengths to vary along the billow axes and region of billow misalignment. At it's core, SAM solves the Boussinesq Navier-Stokes equations:

$$\frac{\partial u_j}{\partial x_j} = 0 \tag{8.8}$$

$$\frac{\partial u_i}{\partial t} + \frac{\partial (u_i u_j)}{\partial x_j} = -\frac{1}{\rho_0}\frac{\partial p'}{\partial x_i} + \frac{\theta'}{\theta_0} g \delta_{i3} + \nu \frac{\partial^2 u_i}{\partial x_i \partial x_j} \tag{8.9}$$

$$\frac{\partial \theta}{\partial t} + \frac{\partial (\theta u_j)}{\partial x_j} = \kappa \frac{\partial^2 \theta}{\partial x_i \partial x_j} \tag{8.10}$$

where u_i, u_j, and u_k are the x, y, and z components of velocity. p is the pressure, ρ is the density, and θ is the potential temperature. ν represents the kinematic viscosity and κ the thermal conductivity. Primes denote perturbation while "0" subscripts denote the mean quantities. Finally, successive indices imply summation.

The model uses a Patterson & Orszag [59] pseudo-spectral algorithm to compute the nonlinear products and a third-order Runge Kutta method [87] to perform time advancement. The model covers a domain of 15 x 15 x 45 km, allowing for 3-4 KH billows. SAM was seeded with KHI with wavelengths of 3.75 - 5 km as well as white noise consistent with an assumed elevated turbulence background from small-scale GWs that we observed in the PMC layer. The model describes all physical parameters and the energy dissipation rate ϵ throughout the domain and in time.

8.6.3 Results

The modelling team simulated billow interactions in KHI and assessed temperature perturbations, vorticity, and energy dissipation rates accompanying these events. They also introduced synthetic PMCs to trace the dynamics and verify our conclusions about how the modelled dynamics perturb PMCs and how those responses appear from below. While I contributed to this paper through analysis of the PMC Turbo data, I am not an expert in these models, so I refer to the paper itself for more detail into the modelling techniques and results (Fritts et al., submitted 2021: Multi-Scale Kelvin-Helmholtz Instability Dynamics Observed by PMC Turbo on 12 July 2018: 2. Modeling KHI Dynamics and PMC Responses).

Our observations confirm Thorpe's expectations for such dynamics in the atmosphere, and the parallel modeling reveals that the dynamics of tubes and knots are dramatically stronger than the secondary convective instabilities and KHI within individual KH billows. Specifically, the accompanying modeling shows that knots arising from initial vortex tubes yield mean $< \epsilon >$ 2-5 times higher than the mean values accompanying KH billows exhibiting secondary convective instabilities and KHI alone - around $0.5 - 1 m^2/s^3$.

Chapter 9: Piggyback

9.1 Background and Motivation

A "piggyback" is a small instrument mounted on the gondola but unassociated with the primary science instrument. We had the opportunity to fly a piggyback camera on the SuperTIGER (Trans-Iron Galactic Element Recorder) experiment in the 2019-2020 Antarctic balloon season. The payload circled Antarctica twice over 32 days while our piggyback continuously captured images. Figure 9.1 shows a map of its trajectory.

Antarctic balloon flights can stay afloat longer than those over the Arctic, so they give us more chances to collect good coincident data. In the Arctic, a balloon must be terminated if it is forecast to drift above the sea ice where it cannot be recovered. Furthermore, NASA needs to be mindful of population centers and national borders in the Arctic, neither of which pose logistical hurdles over Antarctica. In Antarctica drifting poleward does not result in early flight termination and balloons can circumnavigate the pole several times before the polar vortex breaks down and their trajectory becomes unpredictable. Furthermore, PMC occurrence frequency tends to increase at more polar latitudes [47] [8] and Antarctic flights circle at more polar latitudes because the launch site is closer to the pole.

We looked at coincident CIPS images during the PMC Turbo flight and found promising results described in section 7.5. While we were generally interested in additional PMC imaging from the piggyback, we specifically hoped for more coincident CIPS images due to the longer and more polar Antarctic flight. However, we only found a handful of coincident images during the 2018 Arctic flight. The AIM satellite containing the CIPS instrument orbits with a constant precession, we do not control the flight trajectory of PMC Turbo, and we cannot control when PMCs are present. To collect useful data, we need to hope for the instruments to coincidentally image the same location during a period of bright PMCs and interesting dynamics.

9.2 Measurement Details

Our piggyback consisted of one pressure vessel containing a single camera and computer system discussed at length in this thesis, so compared to the PMC Turbo science data, the piggyback had a much smaller composite FOV and had no narrow-field images inset within the FOV. The camera also recorded data at a lower image cadence since we needed to preserve disk space for the longer duration flight. Figure 9.2 shows our pressure vessel system mounted on the SuperTIGER gondola.

We set the off-zenith angle of the piggyback camera at 35 degrees - 9 degrees lower than the PMC Turbo wide-field cameras. This increased the size of the FOV at the expense of resolution. We prioritized FOV size over resolution since we had found during our analyses that we did not require resolution better than 10 meters per pixel. A misaligned baffle caused reflections in the piggyback images, and we digitally removed these regions as part of our image processing. We corrected the images and projected them onto the PMC plane using pointing from imaged star fields using our standard procedure outlined in section 6. Examples of reduced and projected images are shown in Figure 9.3 with a 5 km grid.

9.3 CIPS Overlaps

The AIM satellite hosting the CIPS instrument moves in low earth orbit, with a period of about 90 minutes. Roughly 15 minutes of each orbit, it passes over Antarctica and records PMC albedo. To find coincident images, I searched for periods of time in which piggyback FOV resided in the strip imaged by CIPS during these 15 minutes. I found between 85 and 90 orbits demonstrating such overlap and another 50 instances of near overlap, corresponding to 22 and 35 total hours of data respectively. We are currently analyzing events captured during this time. Figure 9.4 demonstrates one such instance of coincident CIPS overpass and piggyback location.

We hope to use the coincident data to further the same science objectives as PMC Turbo: to

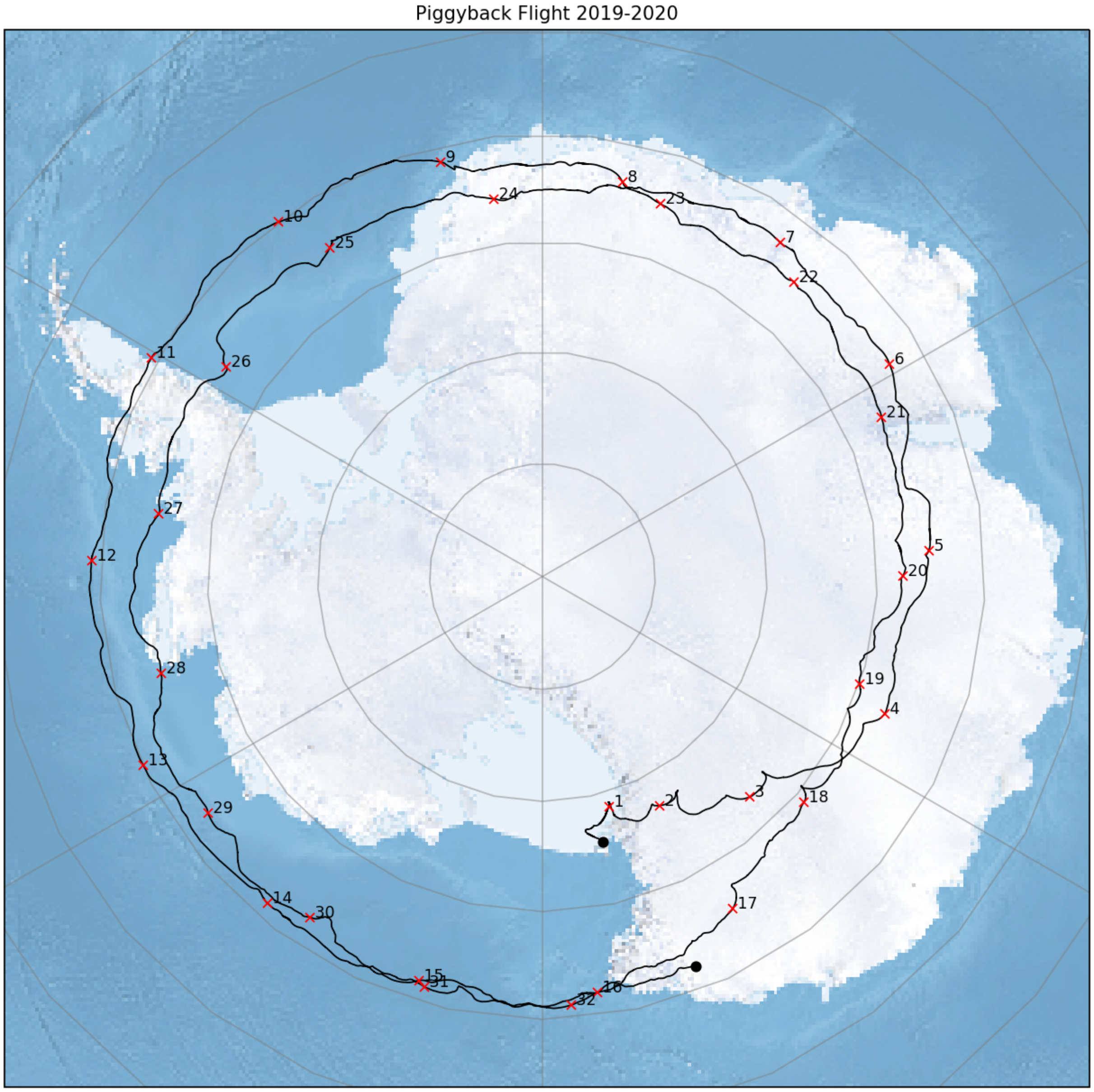

Figure 9.1: Piggyback flight trajectory with marked days of flight

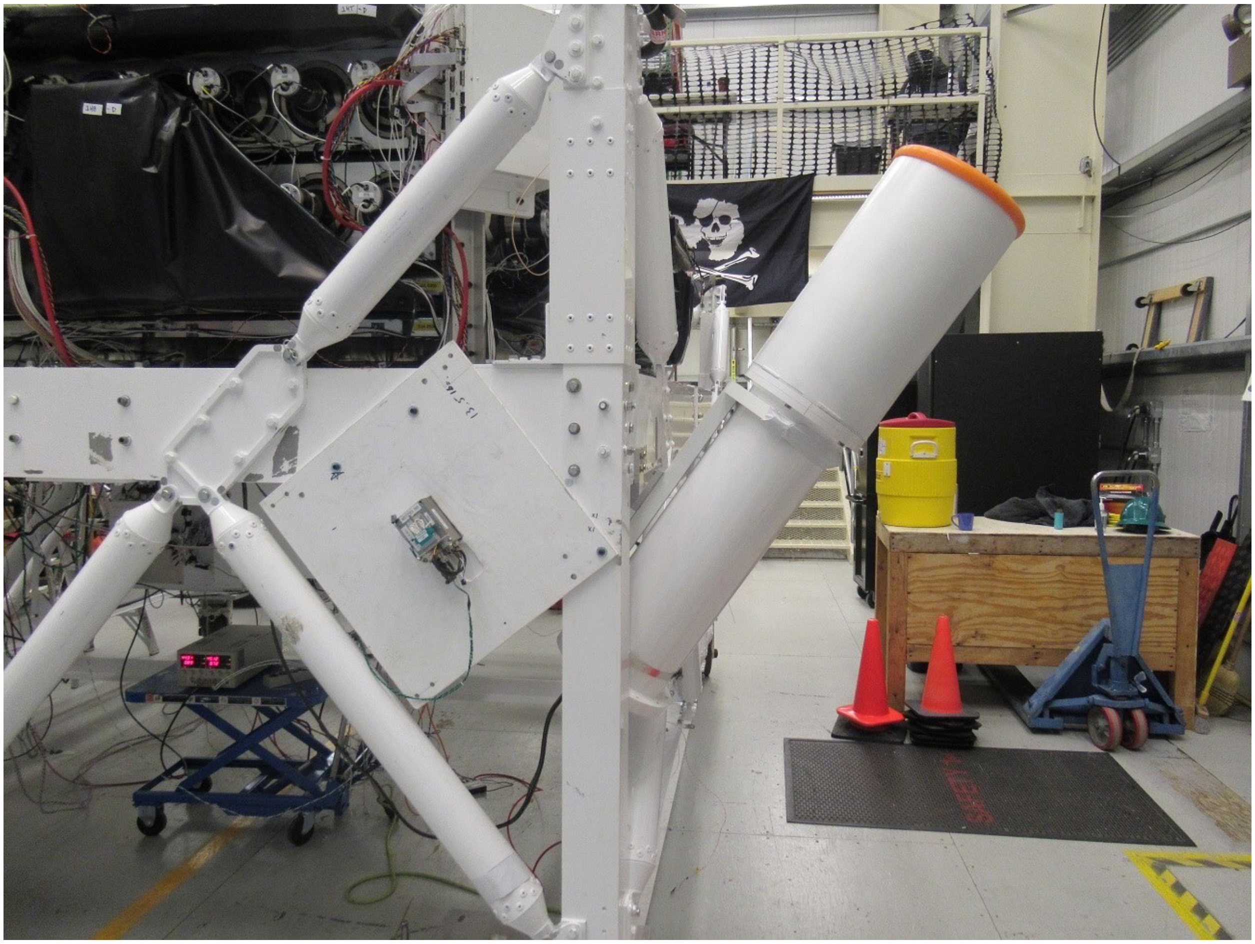

Figure 9.2: Piggyback mounted on the SuperTIGER gondola. Note that this image was taken prior to having updated the baffle design.

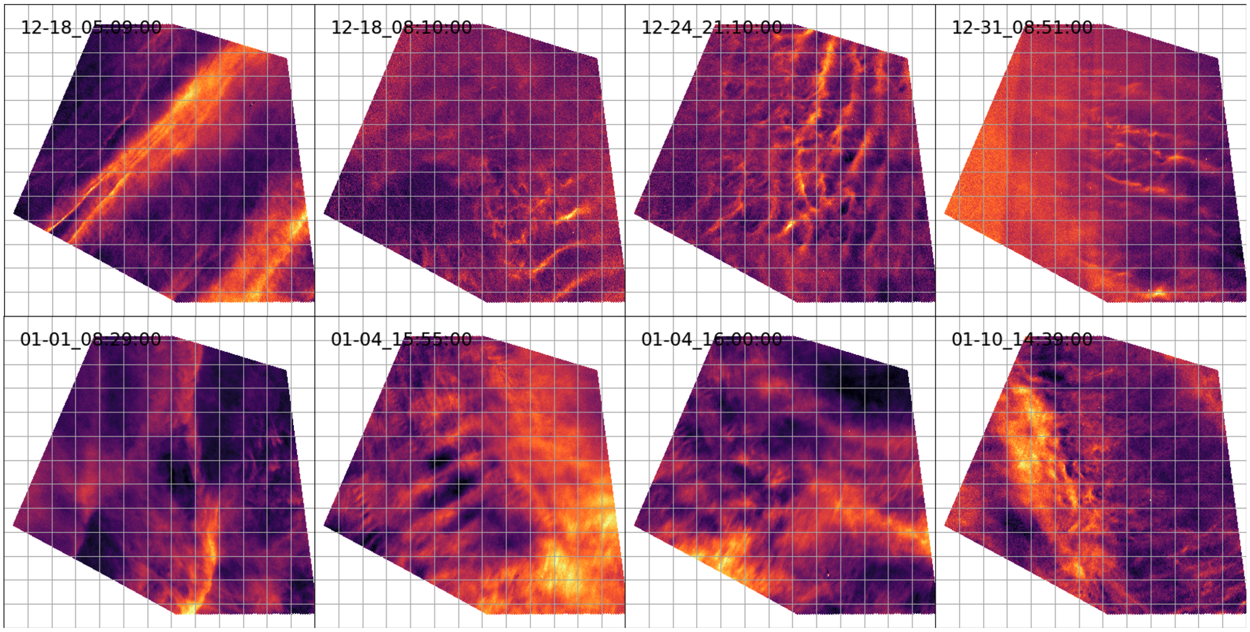

Figure 9.3: Several examples of interesting features captured by the piggyback camera aboard SuperTIGER.

identify the dynamics, scales, and intensities of GWs, instabilities, and turbulence that define the character of GW dissipation events. Understanding these dynamics requires studying atmosphere at many spatial scales. With coincident imaging we hope to extend the high end of the scales we study from 100-200 kilometers to thousands of kilometers.

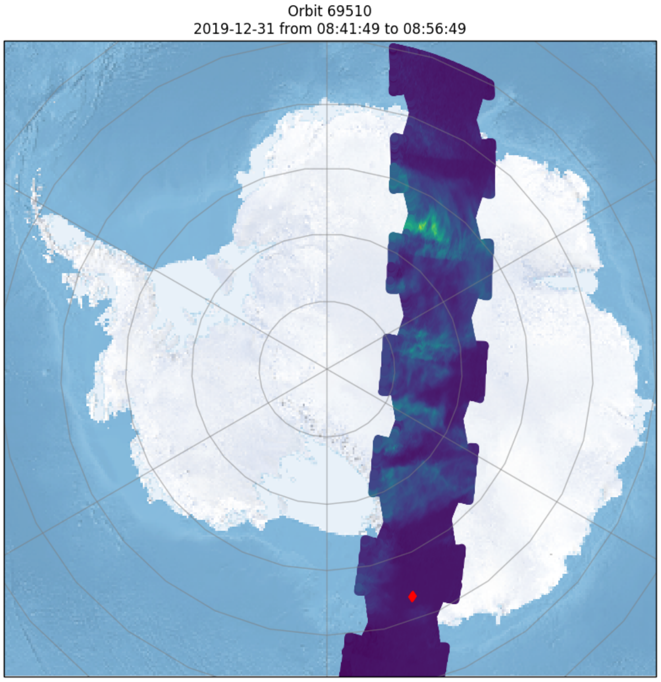

(a) CIPS Albedo measurement

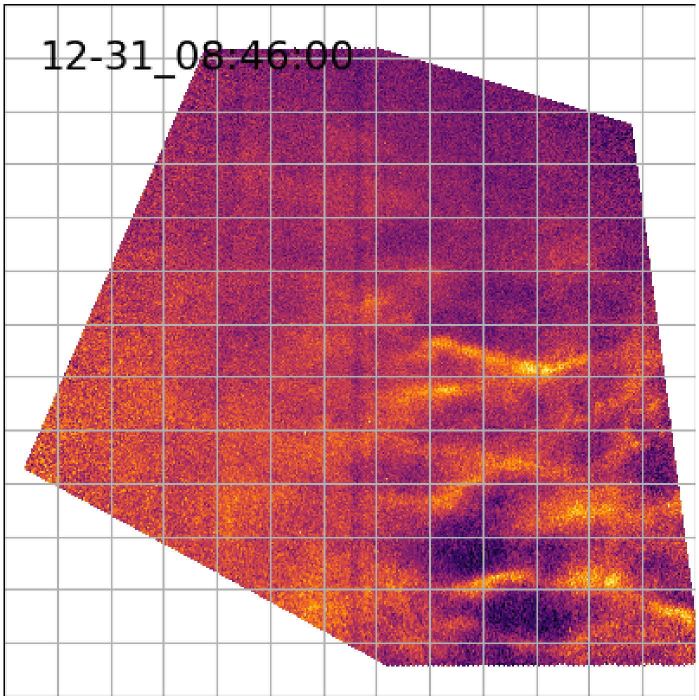

(b) Piggyback PMC brightness

Figure 9.4: Coincident data between the piggyback and CIPS - the piggyback image in panel b is located at the red diamond in panel a

References

[1] M. Abitbol, A. M. Aboobaker, P. Ade, D. Araujo, F. Aubin, C. Baccigalupi, C. Bao, D. Chapman, J. Didier, M. Dobbs, *et al.*, “The ebex balloon-borne experiment—detectors and readout,” *The Astrophysical Journal Supplement Series*, vol. 239, no. 1, p. 8, 2018.

[2] A. Aboobaker, P. Ade, D. Araujo, F. Aubin, C. Baccigalupi, C. Bao, D. Chapman, J. Didier, M. Dobbs, W. Grainger, *et al.*, “The ebex balloon-borne experiment—gondola, attitude control, and control software,” *The Astrophysical Journal Supplement Series*, vol. 239, no. 1, p. 9, 2018.

[3] A. M. Aboobaker, P. Ade, D. Araujo, F. Aubin, C. Baccigalupi, C. Bao, D. Chapman, J. Didier, M. Dobbs, C. Geach, *et al.*, “The ebex balloon-borne experiment—optics, receiver, and polarimetry,” *The Astrophysical Journal Supplement Series*, vol. 239, no. 1, p. 7, 2018.

[4] A. Alcacer, M. Iborra, O. Guiñón, and F. Alted, *Blosc main blog page*, Mar. 2021.

[5] Ø. Andreassen, P. Ø. HVIDSTEN, D. C. Fritts, and S. Arendt, “Vorticity dynamics in a breaking internal gravity wave. part 1. initial instability evolution,” *Journal of Fluid Mechanics*, vol. 367, pp. 27–46, 1998.

[6] S. Arendt, D. C. Fritts, and Ø. Andreassen, “The initial value problem for kelvin vortex waves,” *Journal of Fluid Mechanics*, vol. 344, pp. 181–212, 1997.

[7] I. Azeem, M. Stevens, R. Collins, M. Larsen, B. Williams, M. Taylor, and R. Varney, “Super soaker: A sounding rocket experiment to create and study polar mesospheric clouds,” *cosp*, vol. 42, pp. C2–1, 2018.

[8] S. M. Bailey, A. W. Merkel, G. E. Thomas, and J. N. Carstens, “Observations of polar mesospheric clouds by the student nitric oxide explorer,” *Journal of Geophysical Research: Atmospheres*, vol. 110, no. D13, 2005.

[9] G. Baumgarten and D. C. Fritts, “Quantifying kelvin-helmholtz instability dynamics observed in noctilucent clouds: 1. methods and observations,” *Journal of Geophysical Research: Atmospheres*, vol. 119, no. 15, pp. 9324–9337, 2014.

[10] K. Bossert, C. G. Kruse, C. J. Heale, D. C. Fritts, B. P. Williams, J. B. Snively, P.-D. Pautet, and M. J. Taylor, “Secondary gravity wave generation over new zealand during the deepwave campaign,” *Journal of Geophysical Research: Atmospheres*, vol. 122, no. 15, pp. 7834–7850, 2017.

[11] F. Browand and C. Winant, "Laboratory observations of shear-layer instability in a stratified fluid," *Boundary-Layer Meteorology*, vol. 5, no. 1, pp. 67–77, 1973.

[12] K. Browning and C. Watkins, "Observations of clear air turbulence by high power radar," *Nature*, vol. 227, no. 5255, pp. 260–263, 1970.

[13] C. Caulfield, S. Yoshida, and W. Peltier, "Secondary instability and three-dimensionalization in a laboratory accelerating shear layer with varying density differences," *Dynamics of atmospheres and oceans*, vol. 23, no. 1-4, pp. 125–138, 1996.

[14] A. Chandran, D. Rusch, S. Palo, G. Thomas, and M. J. Taylor, "Gravity wave observations in the summertime polar mesosphere from the cloud imaging and particle size (cips) experiment on the aim spacecraft," *Journal of atmospheric and solar-terrestrial physics*, vol. 71, no. 3-4, pp. 392–400, 2009.

[15] D. Chapman, "EBEX: A Balloon-Borne Telescope for Measuring Cosmic Microwave Background Polarization," Ph.D. dissertation, Columbia University, 2015.

[16] P. Dalin, S. Kirkwood, N. Pertsev, and V. Perminov, "Influence of solar and lunar tides on the mesopause region as observed in polar mesosphere summer echoes characteristics," *Journal of Geophysical Research: Atmospheres*, vol. 122, no. 19, pp. 10–369, 2017.

[17] P. Dalin, N. Pertsev, S. Frandsen, O. Hansen, H. Andersen, A. Dubietis, and R. Balciunas, "A case study of the evolution of a kelvin–helmholtz wave and turbulence in noctilucent clouds," *Journal of atmospheric and solar-terrestrial physics*, vol. 72, no. 14-15, pp. 1129–1138, 2010.

[18] P. Dalin, N. Pertsev, V. Perminov, D. Efremov, and V. Romejko, "Looking at "night-shining" clouds from the stratosphere," *Eos*, vol. 100, no. 4, 2019.

[19] M. T. DeLand, E. P. Shettle, G. E. Thomas, and J. J. Olivero, "Latitude-dependent long-term variations in polar mesospheric clouds from sbuv version 3 pmc data," *Journal of Geophysical Research: Atmospheres*, vol. 112, no. D10, 2007.

[20] N. Engler, R. Latteck, B. Strelnikov, W. Singer, and M. Rapp, "Turbulent energy dissipation rates observed by doppler mst radar and by rocket-borne instruments during the midas/macwave campaign 2002," in *Annales Geophysicae*, Copernicus GmbH, vol. 23, 2005, pp. 1147–1156.

[21] P. M. Franke and R. L. Collins, "Evidence of gravity wave breaking in lidar data from the mesopause region," *Geophysical research letters*, vol. 30, no. 4, 2003.

[22] D. C. Fritts and M. J. Alexander, "Gravity wave dynamics and effects in the middle atmosphere," *Reviews of geophysics*, vol. 41, no. 1, 2003.

[23] D. C. Fritts, S. Arendt, and Ø. Andreassen, “Vorticity dynamics in a breaking internal gravity wave. part 2. vortex interactions and transition to turbulence,” *Journal of Fluid Mechanics*, vol. 367, pp. 47–65, 1998.

[24] D. C. Fritts, G. Baumgarten, K. Wan, J. Werne, and T. Lund, “Quantifying kelvin-helmholtz instability dynamics observed in noctilucent clouds: 2. modeling and interpretation of observations,” *Journal of Geophysical Research: Atmospheres*, vol. 119, no. 15, pp. 9359–9375, 2014.

[25] D. C. Fritts, J. R. Isler, and Ø. Andreassen, “Gravity wave breaking in two and three dimensions: 2. three-dimensional evolution and instability structure,” *Journal of Geophysical Research: Atmospheres*, vol. 99, no. D4, pp. 8109–8123, 1994.

[26] D. C. Fritts, N. Kaifler, B. Kaifler, C. Geach, C. B. Kjellstrand, B. P. Williams, S. D. Eckermann, A. D. Miller, M. Rapp, G. Jones, *et al.*, “Mesospheric bore evolution and instability dynamics observed in pmc turbo imaging and rayleigh lidar profiling over northeastern canada on 13 july 2018,” *Journal of Geophysical Research: Atmospheres*, vol. 125, no. 14, e2019JD032037, 2020.

[27] D. C. Fritts, A. D. Miller, C. B. Kjellstrand, C. Geach, B. P. Williams, B. Kaifler, N. Kaifler, G. Jones, M. Rapp, M. Limon, *et al.*, “Pmc turbo: Studying gravity wave and instability dynamics in the summer mesosphere using polar mesospheric cloud imaging and profiling from a stratospheric balloon,” *Journal of Geophysical Research: Atmospheres*, vol. 124, no. 12, pp. 6423–6443, 2019.

[28] D. C. Fritts, K. Wan, J. Werne, T. Lund, and J. H. Hecht, “Modeling the implications of kelvin-helmholtz instability dynamics for airglow observations,” *Journal of Geophysical Research: Atmospheres*, vol. 119, no. 14, pp. 8858–8871, 2014.

[29] D. C. Fritts, L. Wang, G. Baumgarten, A. D. Miller, M. A. Geller, G. Jones, M. Limon, D. Chapman, J. Didier, C. B. Kjellstrand, *et al.*, “High-resolution observations and modeling of turbulence sources, structures, and intensities in the upper mesosphere,” *Journal of Atmospheric and Solar-Terrestrial Physics*, vol. 162, pp. 57–78, 2017.

[30] D. C. Fritts, S. A. Wieland, T. S. Lund, S. Thorpe, and J. H. Hecht, “Kelvin-helmholtz billow interactions and instabilities in the mesosphere over the andes lidar observatory: 2. modeling and interpretation,” *Journal of Geophysical Research: Atmospheres*, vol. 126, no. 1, e2020JD033412, 2021.

[31] R. R. Garcia, M. López-Puertas, B. Funke, D. R. Marsh, D. E. Kinnison, A. K. Smith, and F. González-Galindo, “On the distribution of co2 and co in the mesosphere and lower thermosphere,” *Journal of Geophysical Research: Atmospheres*, vol. 119, no. 9, pp. 5700–5718, 2014.

[32] C. Geach, S. Hanany, D. Fritts, B. Kaifler, N. Kaifler, C. Kjellstrand, B. P. Williams, S. D. Eckermann, A. Miller, G. Jones, *et al.*, "Gravity wave breaking and vortex ring formation observed by pmc turbo," *Journal of Geophysical Research: Atmospheres*, vol. 125, no. 23, e2020JD033038, 2020.

[33] A. Gettelman, M. Mills, D. Kinnison, R. Garcia, A. Smith, D. Marsh, S. Tilmes, F. Vitt, C. Bardeen, J. McInerny, *et al.*, "The whole atmosphere community climate model version 6 (waccm6)," *Journal of Geophysical Research: Atmospheres*, vol. 124, no. 23, pp. 12 380–12 403, 2019.

[34] R. Goldberg, D. Fritts, F. Schmidlin, B. Williams, C. Croskey, J. Mitchell, M. Friedrich, J. Russell III, U. Blum, and K. Fricke, "The macwave program to study gravity wave influences on the polar mesosphere," in *Annales Geophysicae*, Copernicus GmbH, vol. 24, 2006, pp. 1159–1173.

[35] A. Hauchecorne and M.-L. Chanin, "Density and temperature profiles obtained by lidar between 35 and 70 km," *Geophysical Research Letters*, vol. 7, no. 8, pp. 565–568, 1980.

[36] C. Heale, K. Bossert, J. Snively, D. Fritts, P.-D. Pautet, and M. J. Taylor, "Numerical modeling of a multiscale gravity wave event and its airglow signatures over mount cook, new zealand, during the deepwave campaign," *Journal of Geophysical Research: Atmospheres*, vol. 122, no. 2, pp. 846–860, 2017.

[37] J. Hecht, "Instability layers and airglow imaging," *Reviews of Geophysics*, vol. 42, no. 1, 2004.

[38] J. Hecht, D. Fritts, L. Gelinas, R. Rudy, R. Walterscheid, and A. Liu, "Kelvin-helmholtz billow interactions and instabilities in the mesosphere over the andes lidar observatory: 1. observations," *Journal of Geophysical Research: Atmospheres*, vol. 126, no. 1, e2020JD033414, 2021.

[39] J. Hecht, D. Fritts, L. Wang, L. Gelinas, R. Rudy, R. L. Walterscheid, M. J. Taylor, P.-D. Pautet, S. Smith, and S. Franke, "Observations of the breakdown of mountain waves over the andes lidar observatory at cerro pachon on 8/9 july 2012," *Journal of Geophysical Research: Atmospheres*, vol. 123, no. 1, pp. 276–299, 2018.

[40] J. Hecht, A. Z. Liu, R. Walterscheid, and R. Rudy, "Maui mesosphere and lower thermosphere (maui malt) observations of the evolution of kelvin-helmholtz billows formed near 86 km altitude," *Journal of Geophysical Research: Atmospheres*, vol. 110, no. D9, 2005.

[41] J. Hecht, K. Wan, L. Gelinas, D. C. Fritts, R. Walterscheid, R. Rudy, A. Liu, S. J. Franke, F. Vargas, P.-D. Pautet, *et al.*, "The life cycle of instability features measured from the andes lidar observatory over cerro pachon on 24 march 2012," *Journal of Geophysical Research: Atmospheres*, vol. 119, no. 14, pp. 8872–8898, 2014.

[42] M. Hervig and D. Siskind, “Decadal and inter-hemispheric variability in polar mesospheric clouds, water vapor, and temperature,” *Journal of atmospheric and solar-terrestrial physics*, vol. 68, no. 1, pp. 30–41, 2006.

[43] C. O. Hines, “Earlier days of gravity waves revisited,” *pure and applied geophysics*, vol. 130, no. 2, pp. 151–170, 1989.

[44] D. Hysell, M. Larsen, D. Fritts, B. Laughman, and M. Sulzer, “Major upwelling and overturning in the mid-latitude f region ionosphere,” *Nature communications*, vol. 9, no. 1, pp. 1–11, 2018.

[45] D. Hysell, E. Nossa, M. Larsen, J. Munro, S. Smith, M. Sulzer, and S. González, “Dynamic instability in the lower thermosphere inferred from irregular sporadic e layers,” *Journal of Geophysical Research: Space Physics*, vol. 117, no. A8, 2012.

[46] B. Kaifler, D. Rempel, P. Roßi, C. Büdenbender, N. Kaifler, and V. Baturkin, “A technical description of the balloon lidar experiment (bolide),” *Atmospheric Measurement Techniques*, vol. 13, no. 10, pp. 5681–5695, 2020.

[47] B. Karlsson, C. Randall, S. Benze, M. Mills, V. Harvey, S. Bailey, and J. Russell III, “Intraseasonal variability of polar mesospheric clouds due to inter-hemispheric coupling,” *Geophysical Research Letters*, vol. 36, no. 20, 2009.

[48] G. Klaassen and W. Peltier, “The onset of turbulence in finite-amplitude,” *J. Fluid Mech*, vol. 155, pp. 1–35, 1985.

[49] M. Larsen, “Winds and shears in the mesosphere and lower thermosphere: Results from four decades of chemical release wind measurements,” *Journal of Geophysical Research: Space Physics*, vol. 107, no. A8, SIA–28, 2002.

[50] G. Lehmacher, E. Kudeki, and J. Chau, “High-resolution observations of mesospheric layers with the jicamarca vhf radar,” *cosp*, vol. 36, p. 552, 2006.

[51] H.-L. Liu, “Effective vertical diffusion by atmospheric gravity waves,” *Geophysical Research Letters*, vol. 48, no. 1, e2020GL091474, 2021.

[52] F.-J. Lübken, “Seasonal variation of turbulent energy dissipation rates at high latitudes as determined by in situ measurements of neutral density fluctuations,” *Journal of Geophysical Research: Atmospheres*, vol. 102, no. D12, pp. 13 441–13 456, 1997.

[53] F.-J. Lübken, M. Rapp, and P. Hoffmann, “Neutral air turbulence and temperatures in the vicinity of polar mesosphere summer echoes,” *Journal of Geophysical Research: Atmospheres*, vol. 107, no. D15, ACL–9, 2002.

[54] A. Miller, D. Fritts, D. Chapman, G. Jones, M. Limon, D. Araujo, J. Didier, S. Hillbrand, C. Kjellstrand, A. Korotkov, *et al.*, "Stratospheric imaging of polar mesospheric clouds: A new window on small-scale atmospheric dynamics," *Geophysical Research Letters*, vol. 42, no. 14, pp. 6058–6065, 2015.

[55] B. J. Murray and E. J. Jensen, "Homogeneous nucleation of amorphous solid water particles in the upper mesosphere," *Journal of atmospheric and solar-terrestrial physics*, vol. 72, no. 1, pp. 51–61, 2010.

[56] C. J. Nappo, *An introduction to atmospheric gravity waves*. Academic press, 2013.

[57] T. L. Palmer, D. C. Fritts, and Ø. Andreassen, "Evolution and breakdown of kelvin–helmholtz billows in stratified compressible flows. part ii: Instability structure, evolution, and energetics," *Journal of Atmospheric Sciences*, vol. 53, no. 22, pp. 3192–3212, 1996.

[58] T. L. Palmer, D. C. Fritts, Ø. Andreassen, and I. Lie, "Three-dimensional evolution of kelvin-helmholtz billows in stratified compressible flow," *Geophysical research letters*, vol. 21, no. 21, pp. 2287–2290, 1994.

[59] G. Patterson Jr and S. A. Orszag, "Spectral calculations of isotropic turbulence: Efficient removal of aliasing interactions," *The Physics of Fluids*, vol. 14, no. 11, pp. 2538–2541, 1971.

[60] T. Pfrommer, P. Hickson, and C.-Y. She, "A large-aperture sodium fluorescence lidar with very high resolution for mesopause dynamics and adaptive optics studies," *Geophysical Research Letters*, vol. 36, no. 15, 2009.

[61] M. Rapp, B. Strelnikov, A. Müllemann, F.-J. Lübken, and D. Fritts, "Turbulence measurements and implications for gravity wave dissipation during the macwave/midas rocket program," *Geophysical research letters*, vol. 31, no. 24, 2004.

[62] M. Rapp and G. E. Thomas, "Modeling the microphysics of mesospheric ice particles: Assessment of current capabilities and basic sensitivities," *Journal of Atmospheric and Solar-Terrestrial Physics*, vol. 68, no. 7, pp. 715–744, 2006.

[63] B. Reichborn-Kjennerud, "Building and flying the E and B Experiment to measure the polarization of the cosmic microwave background," Ph.D. dissertation, Columbia University, Nov. 2010.

[64] N. Rosenberg and E. M. Dewan, *Stratospheric turbulence and vertical effective diffusion coefficients*, 519. Air Force Cambridge Research Laboratories, Air Force Systems Command, United . . ., 1975, vol. 75.

[65] L. Rosenhead, “The formation of vortices from a surface of discontinuity,” *Proceedings of the Royal Society of London. Series A, Containing Papers of a Mathematical and Physical Character*, vol. 134, no. 823, pp. 170–192, 1931.

[66] R. Russel, “Ucar learning-zone layers-earths-atmosphere,” *Layers of Earth’s Atmosphere*,

[67] T. Sato and R. F. Woodman, “Fine altitude resolution observations of stratospheric turbulent layers by the arecibo 430 mhz radar,” *Journal of Atmospheric Sciences*, vol. 39, no. 11, pp. 2546–2552, 1982.

[68] D. G. Schowalter, C. W. Van Van Atta, and J. C. Lasheras, “A study of streamwise vortex structure in a stratified shear layer,” *Journal of Fluid Mechanics*, vol. 281, pp. 247–291, 1994.

[69] R. Scorer, “Billow mechanics,” *Radio Science*, vol. 4, no. 12, pp. 1299–1307, 1969.

[70] W. Singer, R. Latteck, and W. Hocking, “Measurement of turbulent kinetic energy dissipation rates in the mesosphere by a 3 mhz doppler radar,” in *35th COSPAR Scientific Assembly*, vol. 35, 2004, p. 3922.

[71] M. H. Stevens, J. Gumbel, C. R. Englert, K. U. Grossmann, M. Rapp, and P. Hartogh, “Polar mesospheric clouds formed from space shuttle exhaust,” *Geophysical Research Letters*, vol. 30, no. 10, 2003.

[72] M. H. Stevens, R. Meier, X. Chu, M. T. DeLand, and J. M. Plane, “Antarctic mesospheric clouds formed from space shuttle exhaust,” *Geophysical research letters*, vol. 32, no. 13, 2005.

[73] G. R. Swenson and S. B. Mende, “Oh emission and gravity waves (including a breaking wave) in all-sky imagery from bear lake, ut,” *Geophysical research letters*, vol. 21, no. 20, pp. 2239–2242, 1994.

[74] M. J. Taylor, P.-D. Pautet, Y. Zhao, C. Randall, J. Lumpe, S. Bailey, J. Carstens, K. Nielsen, J. M. Russell, and J. Stegman, “High-latitude gravity wave measurements in noctilucent clouds and polar mesospheric clouds,” in *Aeronomy of the Earth’s Atmosphere and Ionosphere*, Springer, 2011, pp. 93–105.

[75] G. E. Thomas, J. J. Olivero, M. Deland, and E. P. E. P. Shettle, “Comment on “are noctilucent clouds truly a “miner’s canary” for global change?”,” *Eos, Transactions American Geophysical Union*, vol. 84, no. 36, pp. 352–353, 2003.

[76] G. E. Thomas, J. J. Olivero, E. J. Jensen, W. Schroeder, and O. B. Toon, “Relation between increasing methane and the presence of ice clouds at the mesopause,” *Nature*, vol. 338, no. 6215, pp. 490–492, 1989.

[77] W. Thomson, “Xxiv. vibrations of a columnar vortex,” *The London, Edinburgh, and Dublin Philosophical Magazine and Journal of Science*, vol. 10, no. 61, pp. 155–168, 1880.

[78] S. A. Thorpe, “Laboratory observations of secondary structures in kelvin-helmhoitz billows and consequences for ocean mixing,” *Geophysical & Astrophysical Fluid Dynamics*, vol. 34, no. 1-4, pp. 175–199, 1985.

[79] ——, “Experiments on the instability of stratified shear flows: Miscible fluids,” *Journal of Fluid Mechanics*, vol. 46, no. 2, pp. 299–319, 1971.

[80] ——, “Experiments on instability and turbulence in a stratified shear flow,” *Journal of Fluid Mechanics*, vol. 61, no. 4, pp. 731–751, 1973.

[81] ——, “Turbulence in stably stratified fluids: A review of laboratory experiments,” *Boundary-layer meteorology*, vol. 5, no. 1-2, pp. 95–119, 1973.

[82] ——, “Turbulence and mixing in a scottish loch,” *Philosophical Transactions of the Royal Society of London. Series A, Mathematical and Physical Sciences*, vol. 286, no. 1334, pp. 125–181, 1977.

[83] ——, “Transitional phenomena and the development of turbulence in stratified fluids: A review,” *Journal of Geophysical Research: Oceans*, vol. 92, no. C5, pp. 5231–5248, 1987.

[84] ——, “The axial coherence of kelvin–helmholtz billows,” *Quarterly Journal of the Royal Meteorological Society: A journal of the atmospheric sciences, applied meteorology and physical oceanography*, vol. 128, no. 583, pp. 1529–1542, 2002.

[85] J. Werne and D. C. Fritts, “Stratified shear turbulence: Evolution and statistics,” *Geophysical research letters*, vol. 26, no. 4, pp. 439–442, 1999.

[86] B. Williams, D. Fritts, C. She, and R. Goldberg, “Gravity wave propagation through a large semidiurnal tide and instabilities in the mesosphere and lower thermosphere during the winter 2003 macwave rocket campaign,” in *Annales Geophysicae*, Copernicus GmbH, vol. 24, 2006, pp. 1199–1208.

[87] J. Williamson, “Low-storage runge-kutta schemes,” *Journal of Computational Physics*, vol. 35, no. 1, pp. 48–56, 1980.

[88] G. Witt, “Height, structure and displacements of noctilucent clouds,” *Tellus*, vol. 14, no. 1, pp. 1–18, 1962.

[89] R. Woodman and P. Rastogi, “Evaluation of effective eddy diffusive coefficients using radar observations of turbulence in the stratosphere,” *Geophysical research letters*, vol. 11, no. 3, pp. 243–246, 1984.

[90] J. Woods, "Wave-induced shear instability in the summer thermocline," *Journal of Fluid Mechanics*, vol. 32, no. 4, pp. 791–800, 1968.

[91] ——, "On richardson's number as a criterion for laminar-turbulent-laminar transition in the ocean and atmosphere," *Radio Science*, vol. 4, no. 12, pp. 1289–1298, 1969.

[92] J. Woods and R. Wiley, "Billow turbulence and ocean microstructure," in *Deep Sea Research and Oceanographic Abstracts*, Elsevier, vol. 19, 1972, 87–IN1.

[93] Y. Yamada, H. Fukunishi, T. Nakamura, and T. Tsuda, "Breaking of small-scale gravity wave and transition to turbulence observed in oh airglow," *Geophysical research letters*, vol. 28, no. 11, pp. 2153–2156, 2001.

[94] U. von Zahn, "Are noctilucent clouds a "miner's canary" for global change?" *EOS, Transactions American Geophysical Union*, vol. 84, no. 28, pp. 261–264, 2003.

Appendix A: Gravity Wave Theory

I present basic GW theory here for the benefit of the reader. The work follows Nappo [56], and I do not claim the theory here as my own.

A.1 The Brunt-Väisälä frequency

In general, when analyzing atmospheric dynamics, we assume a stably stratified atmosphere, defined as one in which density increases with depth. Above the boundary layer, the Earth's atmosphere is almost always stably stratified.

In a stably stratified fluid, it is trivial to deduce that the buoyant force on a displaced parcel of air is

$$\vec{F_b} = -g(m_p - m_a)\hat{z} = m_p \frac{d^2(\delta z)}{dt^2}\hat{z} \tag{A.1}$$

where m_p is mass of the parcel and m_a is the mass of the air displaced by the parcel. The ideal gas law is

$$p = \rho RT \tag{A.2}$$

where p is pressure, ρ is density, T is temperature, and R is the universal gas constant. Recognizing that

$$m_p = \rho_p v_p \tag{A.3}$$

where ρ_p and v_p are the density and volume of the air parcel respectively. We assume that the volume of the air parcel and displaced air are equal, and we assume that the pressure of both is equal to the environmental air pressure. We can see that

$$\frac{d^2(\delta z)}{dt^2} = -g\frac{\rho_p - \rho_a}{\rho_p} = -g\frac{T_a - T_p}{T_a} \tag{A.4}$$

where the subscripts "p" and "a" refer to the air parcel and the displaced air (the environmental air) respectively. Expanding both temperatures to first order at some equilibrium height z_e we find

$$T_a(z_e + \delta z) = T_0 + \left.\frac{\partial T_a}{\partial z}\right|_{z_e} + \cdots \tag{A.5}$$

$$T_p(z_e + \delta z) = T_0 + \left.\frac{\partial T_p}{\partial z}\right|_{z_e} + \cdots \tag{A.6}$$

When we neglect higher order terms, since we assume the change in the environmental temperature is small compared to T_0 and we find

$$\frac{d^2(\delta z)}{dt^2} = \frac{-g}{T_a}\left(\frac{\partial T_a}{\partial z} - \frac{\partial T_p}{\partial z}\right)\delta z \tag{A.7}$$

which we recognize as an equation for simple harmonic motion. With a bit of massaging, we can express the frequency in a more friendly way.

When we study GWs, we typically use the hydrostatic approximation. We assume that the vertical motions tend to be small and there will typically be a balance between the weight of a unit parcel of air and the upward pressure of the atmosphere. We can write this assumption as

$$\delta p = -\rho g \delta z \tag{A.8}$$

where δp is the difference between the pressure on the top and bottom of the air parcel and ρ is the density of that air. For small δz we can rewrite this equation as

$$\frac{\partial p}{\partial z} = -\rho g \tag{A.9}$$

which is known as the hydrostatic equation. The processes we study are adiabatic. In this case, we know from the first law of thermodynamics

$$dq = c_p dT - \frac{1}{\rho} dp = 0 \tag{A.10}$$

where c_p is the specific heat capacity. When we substitute the hydrostatic equation A.9 into A.10 we see

$$c_p dT + g dz = 0 \tag{A.11}$$

and therefore

$$-\frac{dT}{dz} = \frac{g}{c_p} = \Gamma \tag{A.12}$$

Γ is the adiabatic lapse rate. For dry air, we have measured c_p and Γ. We can define

$$\frac{\partial T_a}{\partial z} = \gamma_a \tag{A.13}$$

as the atmospheric temperature gradient. With these definitions, we rewrite equation A.7 as

$$\frac{d^2(\delta z)}{dt^2} = -\frac{g}{T_a}(\Gamma - \gamma_a)\delta z \tag{A.14}$$

It is useful to use to express our dynamics in terms of a potential temperature θ defined as the temperature an air parcel would have if compressed or expanded adiabatically from its current temperature to a set pressure - taken as 1000 mb for the Earth's surface. From our adiabatic equation A.10 we see

$$\frac{c_p}{R}\frac{dT}{T} = \frac{dP}{P} \tag{A.15}$$

Integrating A.15 from pressure 1000 mb at temperature θ to pressure P at temperature T gives us

$$\frac{c_p}{R} \ln \frac{T}{\theta} = \ln \frac{P}{1000} \tag{A.16}$$

Therefore, we know the potential temperature θ is

$$\theta = T \left(\frac{1000}{P} \right)^{R/c_p} \tag{A.17}$$

where $R/c_p = 0.286$.

Now that we have defined the potential temperature θ, we can rewrite our wave equation A.14 in terms of it. When we take the logarithmic derivative of the potential temperature we find

$$\frac{d}{dz} \ln \theta = \frac{1}{\theta} \frac{d\theta}{dz} = \frac{1}{T_a} \frac{dT_a}{dz} - \frac{R}{c_p} \frac{1}{p} \frac{dp}{dz} \tag{A.18}$$

Substituting the hydrostatic equation A.9 and the ideal gas law A.2, and using our definitions A.12 and A.13, we simplify equation A.18 as

$$\frac{d}{dz} \ln \theta = \frac{1}{T_a} \left(\frac{dT_a}{dz} + \frac{g}{c_p} \right) = \frac{\Gamma - \gamma_a}{T_a} \tag{A.19}$$

Now we rewrite our wave equation in terms of potential temperature and find

$$\frac{d^2(\delta z)}{dt^2} = -\frac{g}{\theta} \frac{d\theta}{dz} \delta z \tag{A.20}$$

giving us the familiar wave equations

$$z(t) = Ae^{iNt} + Be^{-iNt} \tag{A.21}$$

where N is

$$N = \sqrt{\frac{g}{\theta} \frac{d\theta}{dz}} \tag{A.22}$$

It is plain to see that when $\frac{d\theta}{dz} > 0$ - what we have defined as a stably stratified fluid - wave motion is possible. However, when $\frac{d\theta}{dz} < 0$, the displacement will grow or attenuate. Such a situation is referred to as a convective instability.

To give the reader some intuition about actual atmospheric behavior - the Brunt-Väisälä frequency of average tropospheric conditions is $N \sim 0.012s^{-1}$, giving a buoyancy period of about 8 minutes. For boundary layer conditions, $N \sim 0.2s^{-1}$, corresponding to a buoyancy period around a minute.

Note that the Brunt-Väisälä frequency represents the maximum frequency can attain with air parcels only moving vertically. In fact, GWs typically propagate at an angle. While I will not go through the derivation with detail (I recommend interested readers to review Nappo), it is not difficult to see that the restoring force for some air parcel displaced with an angle β to vertical will experience a buoyancy force with magnitude

$$F_b = -g(m_p - m_a)\sin\beta \tag{A.23}$$

and that the angle term will carry through the derivation to give a frequency

$$N' = N\sin\beta \tag{A.24}$$

where N as usual is the Brunt-Väisälä frequency.

A.2 Richardson Number

Consider a boundary between two fluids A and B. The fluids each have a constant density ρ and a uniform speed u. Fluid A is above fluid B and both have heights labelled z.

We know from basic kinematics that the initial potential energy of the system is:

$$P_I = g(\rho_A z_A + \rho_B z_B) \tag{A.25}$$

and the initial kinetic energy of the system is

$$K_I = \frac{1}{2}(\rho_A u_A^2 + \rho_B u_B^2) \tag{A.26}$$

If we exchange the parcel positions adiabatically and conserve mass and momentum we require that

$$\rho_A + \rho_B = \rho'_A + \rho'_B \tag{A.27}$$

and if we require that both parcels move at some final speed u_f by conservation of momentum we know

$$\rho_A u_A + \rho_B u_B = (\rho'_A + \rho'_B)u_F = (\rho_A + \rho_B)u_F \tag{A.28}$$

and we find that

$$u_F = \frac{\rho_A u_A + \rho_B u_B}{\rho_A + \rho_B} \tag{A.29}$$

We know the final kinetic energy is

$$K_F = \frac{1}{2}(\rho_A + \rho_B)u_F^2 \tag{A.30}$$

or substituting equation A.29

$$K_F = \frac{1}{2}\frac{(\rho_A u_A + \rho_B u_B)^2}{\rho_A + \rho_B} \tag{A.31}$$

and from equation the change in kinetic energy is

$$\Delta K = -\frac{\rho_A \rho_B}{2(\rho_A + \rho_B)}(u_A - u_B)^2 \tag{A.32}$$

Assuming that the density of the parcels exchanging places remains the same, we know

$$P_F = g(\rho_A z_B + \rho_B z_A) \tag{A.33}$$

and

$$\Delta P = g(\rho_A - \rho_B)(z_B - z_A) \tag{A.34}$$

The work done on or by the system is trivially $\Delta K + \Delta P$. If the system does work ($W < 0$) it is unstable, and if work is done on the system ($W > 0$) it is stable.

When we assume a constant density ρ for all air, but still assume two velocities u_A and u_B. ΔP goes to zero and we find the system will always be unstable.

When we assume a constant velocity u but two densities ρ_A and ρ_B we see the system is stable if the denser fluid resides beneath the less dense fluid, and unstable otherwise.

For a system in which both velocity and density change with height, we expand the movement of a fluid parcel from location A to B in first order:

$$\rho_B = \rho_A + \left.\frac{\partial \rho}{\partial z}\right|_{z_A} (z_B - z_A) \tag{A.35}$$

$$u_B = u_A + \left.\frac{\partial u}{\partial z}\right|_{z_A} (z_B - z_A) \tag{A.36}$$

Substituting these first order expansions to find the work

$$W = \Delta K + \Delta P = g(\rho_A - \rho_B)(z_B - z_A) - \frac{\rho_A \rho_B}{2(\rho_A + \rho_B)}(u_A - u_B)^2 \tag{A.37}$$

$$W = g(\frac{\partial \rho}{\partial z}(z_B - z_A)^2 - \frac{\rho_A \rho_A + \frac{\partial \rho}{\partial z}(z_B - z_A)}{2(\rho_A + \rho_A + \frac{\partial \rho}{\partial z}(z_B - z_A))}\left(\frac{\partial u}{\partial z}(z_B - z_A)\right)^2 \tag{A.38}$$

The ρ_A^2 term can be approximated as $\rho_A/2$. Under the Boussinesq approximation, we can express the Brunt-Väisälä frequency N [56]

$$N^2 = \frac{-g}{\rho_0}\frac{\partial \rho_0}{\partial z} \tag{A.39}$$

We can then simplify equation A.38 as

$$W = \left(\rho_0 N^2 - \frac{\rho_0}{4}(\frac{\partial u}{\partial z})^2\right)(z_B - z_A)^2 \tag{A.40}$$

We note that if the $\left(\rho_0 N^2 - \frac{\rho_0}{4}(\frac{\partial u}{\partial z})^2\right)$ term is negative or positive we will have negative or positive work, implying stable and unstable conditions. As a result, it is convenient to define a term that we can use to quickly determine whether this system is stable or unstable. We call this term the Richardson number, written as Ri, and we define it as

$$Ri = \frac{N^2}{(\partial u/\partial z)^2} \tag{A.41}$$

and we rewrite equation A.40 as

$$W = \rho_0(z_B - z_A)^2(\frac{\partial u}{\partial z})^2(Ri - 0.25) \tag{A.42}$$

We can see that the system will be stable if $Ri > 0.25$.

A.3 Reynolds Number

The Reynolds number, typically abbreviated as Re, represents a ratio between inertial to viscous forces as different parts of a fluid move relative to each other. It is defined as

$$Re = \frac{\rho u L}{\mu} \tag{A.43}$$

where ρ is fluid density, u is the flow speed, μ is the viscosity of the liquid, and L is a characteristic dimension depending on the geometry of the flow.

In terms of kinematic viscosity $\nu = \frac{\mu}{\rho}$,

$$Re = \frac{uL}{\nu} \tag{A.44}$$

Viscosity tends to inhibit turbulent motion. Low *Re* represents dominant viscous forces and predicts laminar flow of constant fluid motion. High *Re* represents dominent inertial forces and predicts turbulent motion.

Appendix B: Instrument performance during flight

B.1 Thermal conditions

The pressure vessels experienced a wide range of temperatures from launch - about -20 C to 30 C. Figure B.1b shows the temperature recorded by sensor thermally coupled to the front (lens-side) of each pressure vessel while Figure B.1a shows the temperature recorded by the Labjack inside each pressure vessel. Due to fans circulating air inside each pressure vessel, the Labjack temperature is a good measurement of the ambient temperature within each pressure vessel. The Labjack recorded temperature 5-10 degrees higher than the front panel sensor, which recorded the coldest temperatures measured on each pressure vessels. The front sensor was embedded in the front flange, which is somewhat thermally conductive to the outside and therefore measures lower temperatures.

The thermal conditions were within the range we expected. Our hardware functioned nominally, with the exception of the focus of one of our lens. Camera 5, one of the wide-field camera, experienced the drop of focus from infinity to zero. While could not disassemble our lenses and perform thermal tests, our working hypothesis is that the cold temperatures caused malfunctions in the stepper motor responsible for adjusting focus steps. Figure B.2 shows the camera module temperature and focus step settings for the duration of the flight. Note that camera 5 focus step drops during cold periods of the day. A focus step setting of around 4700 was nominal for the wide-field cameras. We implemented a software correction live over the Iridium Pilot communication channel. We had seen occasional examples of this error in our thermal vacuum testing, and had prepared a function which restored focus to nominal in the even it dropped to zero. By default, we did not enable this fix since we were worried about damaging hardware by adjusting cold lenses every software loop (interval 2 seconds). We were especially worried about enabling this

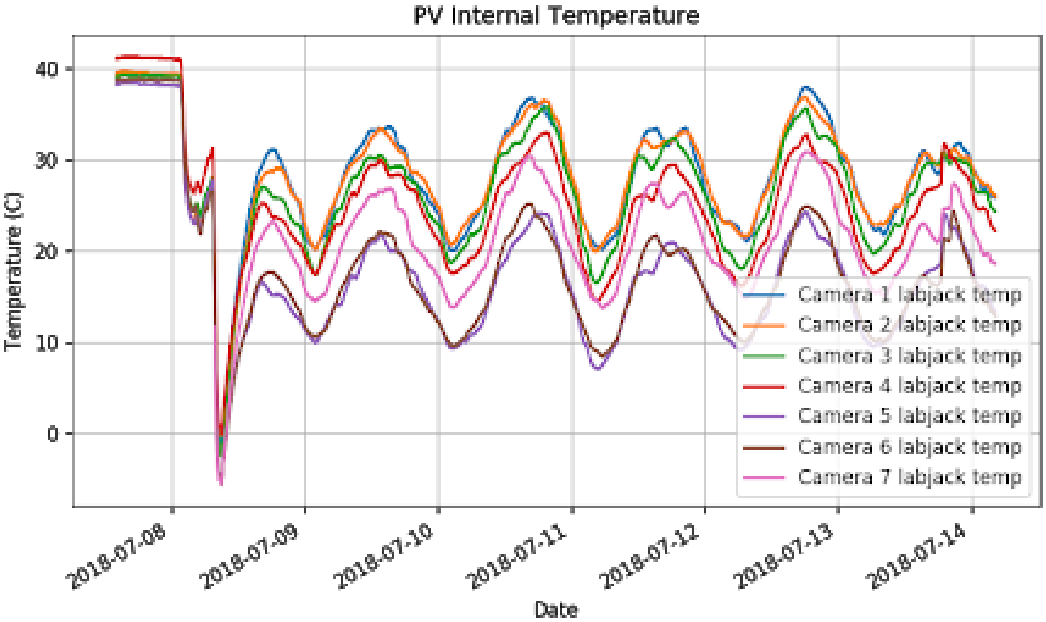

(a) Labjack (ambient air) temperature

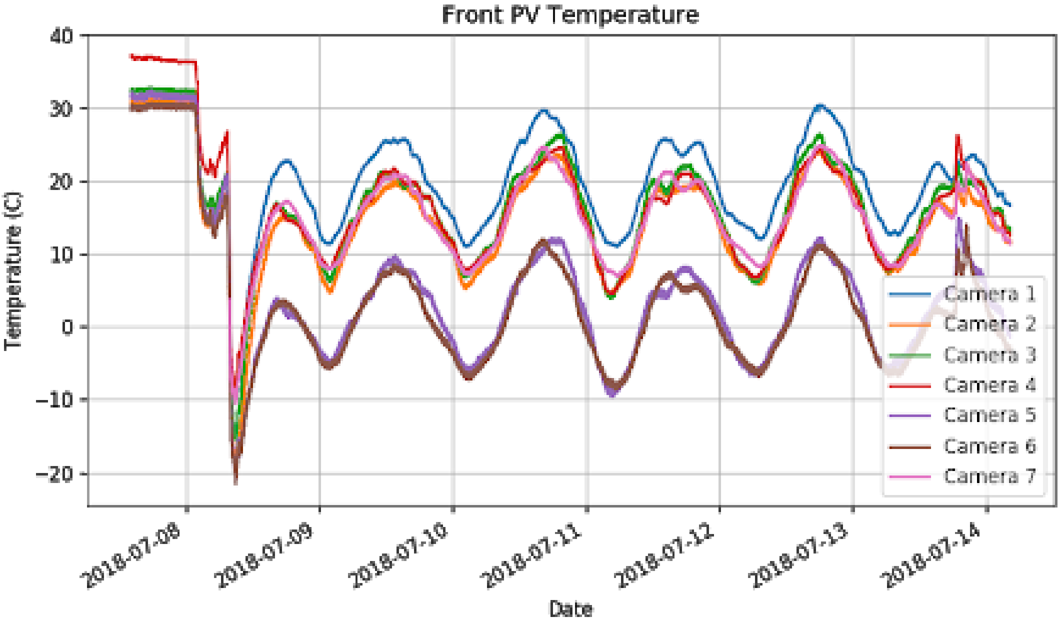

(b) Front flange temperature

Figure B.1: Pressure vessel internal temperature measurements during flight

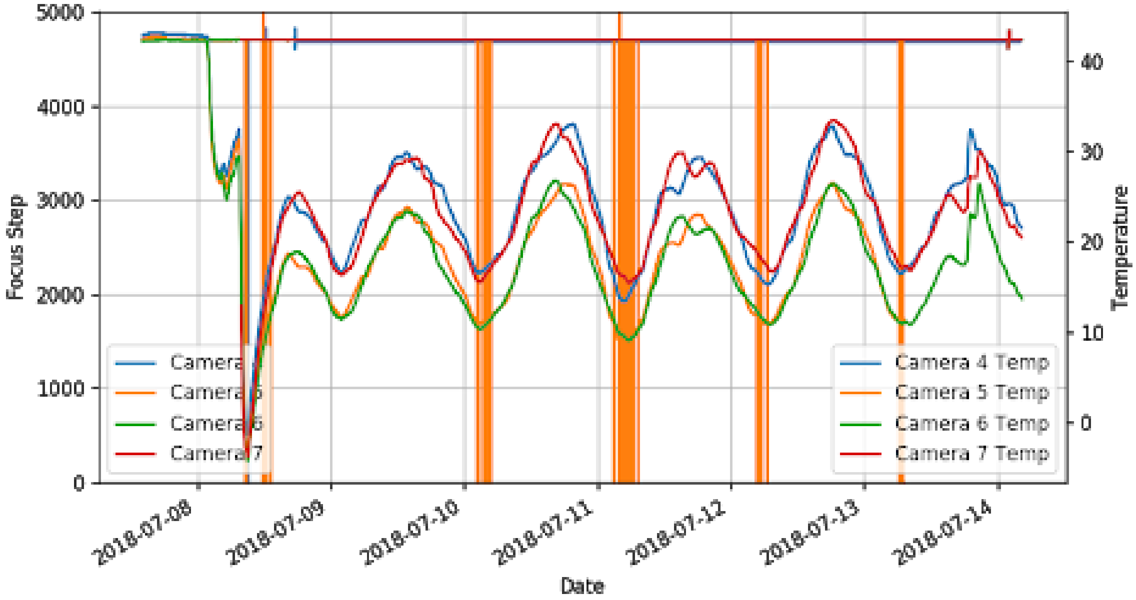

Figure B.2: Camera temperature and focus steps over flight

setting during the ascent through the cold tropopause. We did not have good models or measurements of convective cooling through this region as our experiment ascended. Once we observed the focus drops, we had reached float, so we felt comfortable implementing the fix. We logged into the camera using an SSH connection over the Iridium Pilot link, toggled the fix, and restarted the camera.

B.2 Exposure and Motion blur

During flight, we alternated the exposure mode between auto-exposures and static exposure lengths due to varying sky conditions. In the auto-exposure mode, we used our custom auto-exposure algorithm which automatically and periodically evaluated the statistics of a recently captured image and then adjusted the exposure to the CCD well depth to within an adjustable range. We adjusted the trigger interval and frame rate to match this exposure. The auto-exposure mode attempts to optimize the SNR for a single frame but takes no account of motion blur present in the image. We generally set narrow-field cameras to longer exposure durations, since the narrow-field

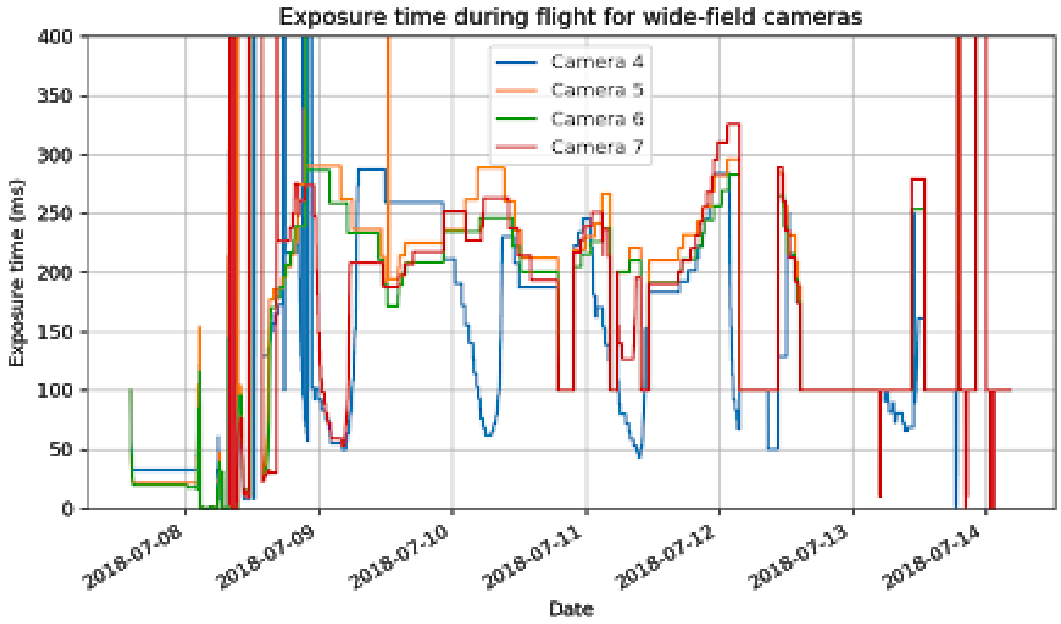

(a) Wide field camera exposure

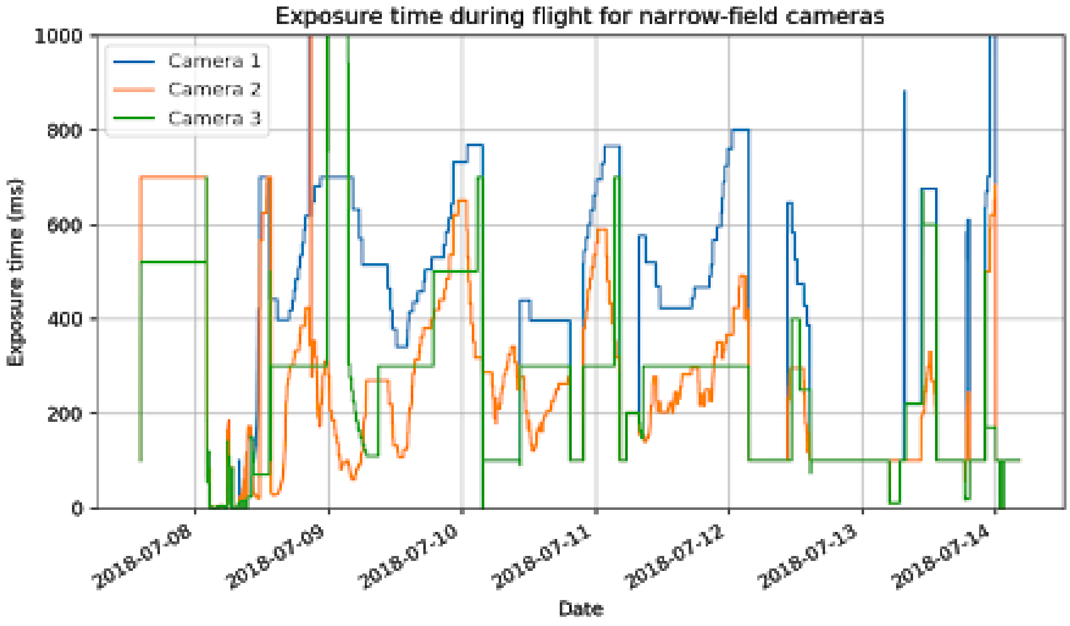

(b) Narrow field camera exposure

Figure B.3: Exposure times used for cameras throughout flight lenses had lower SNR due to the narrower apertures. In general, the auto-exposure algorithm found an optimal exposure of 200–300 ms for wide-field cameras.

We wanted to test both the auto-exposure and manual exposure methods during flight. Auto-exposure gave the best signal-to-noise of the sky without overexposing, so by default, we left the cameras in auto-exposure mode. After we confirmed the presence of PMCs in our images for several hours, we switched to shorter manual exposures, so we could analyze the utility of both modes with PMC images. This method prioritized auto-exposure, and by 12 July, we knew that we had captured many PMC images. To ensure we captured sufficient manual exposures to analyze, we manually set the exposure of the wide-field cameras to 100 ms for the duration of 12 July.

We observed light reflections into one narrow-field camera during flight. Auto-exposure did not handle this situation well, so we used the flexibility of our exposure control to manually set exposure for that camera and to avoid losing SNR in the entire image by allowing the section of the image with the reflection to over-expose. In the last days of flight, we set the narrow-field cameras to a short exposure time to test burst-mode capabilities for future flights.

The bulk velocity we observe by tracking features varied throughout flight and fell within the predicted range. The high-frequency oscillation varied in direction on short timescales and had a period several times longer than our image capture cadence. The effect of the motion blur on our image resolution therefore varies throughout individual events. The inner scale of turbulence at the PMC layer is about 20 m. Depending on the exposure settings used, the motion blur affected scales similar to the inner scale of turbulence. This has imposed challenges in measuring the power spectrum of turbulence in the PMC layer, but our larger scale dynamics analysis tends to study features with scales of hundreds to thousands of meters, so the motion blur did not prevent us from achieving our primary science goals. In these analyses, SNR is more useful than spatial resolution, so we bin adjacent pixels, reducing the effect of recorded motion blur.

In reality, we observed around an eighth of a degree of rotation every 50 seconds, introducing negligible motion blur. However, we observed a shorter higher frequency oscillation of unknown origin, which I investigate in Section B.3. This oscillation varied in direction on rapid timescales

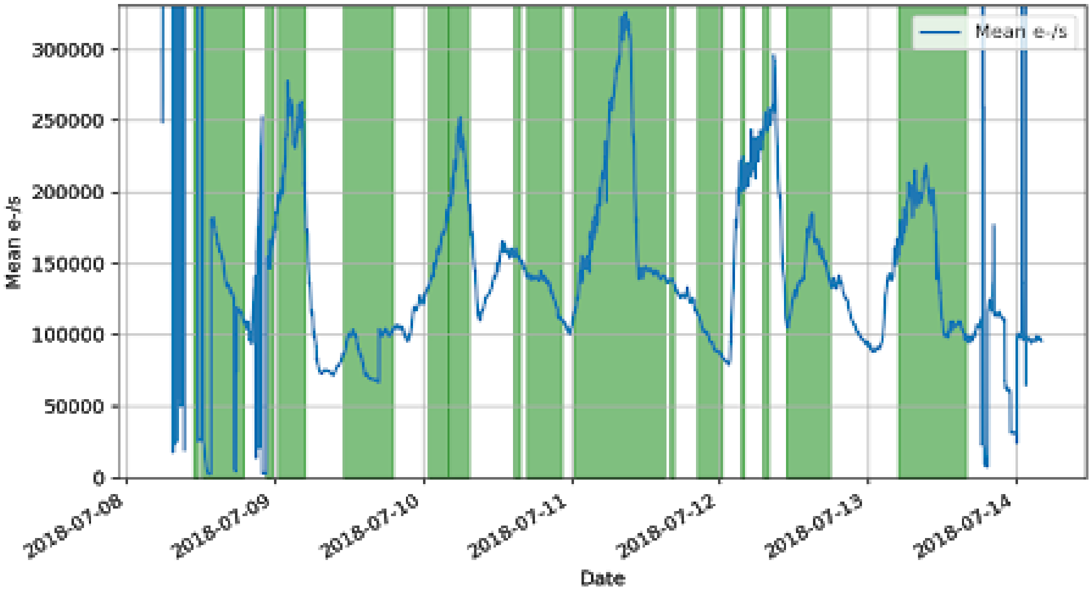

Figure B.4: The mean of images from camera 4, divided by the exposure and multiplied by the gain to find mean electrons/second across the CCD. Green highlighted sections are times when PMCs were observed in the lidar. The pre-flight expectation was about 330 ke-/s sky brightness.

and had a high frequency which made it difficult to track in the pointing solutions. Examining projected images, we found an oscillation of varying direction, about 110 m amplitude projected onto the PMC plane, and with a period of 10-12 seconds. This introduces at worst 70 m/s apparent motion, with a root mean square of 50 m/s. The observed bulk velocity varied throughout flight. The high-frequency oscillation varied in direction on short time scales, and had a period several times longer than our image capture cadence.

B.3 Jitter Analysis

Unexpectedly, we observed an oscillation in our images with a period of 10 s. The oscillation varied in direction on timescales of minutes. The oscillation is the largest contributor to our motion blur, as it has an amplitude of <0.1° or 110 m when the images are projected onto the PMC plane. With a 10-s period, this motion introduces 70 m/s of worst case apparent motion with a root mean square of 50 m/s. We examined the projected images and found that not only did the oscillation

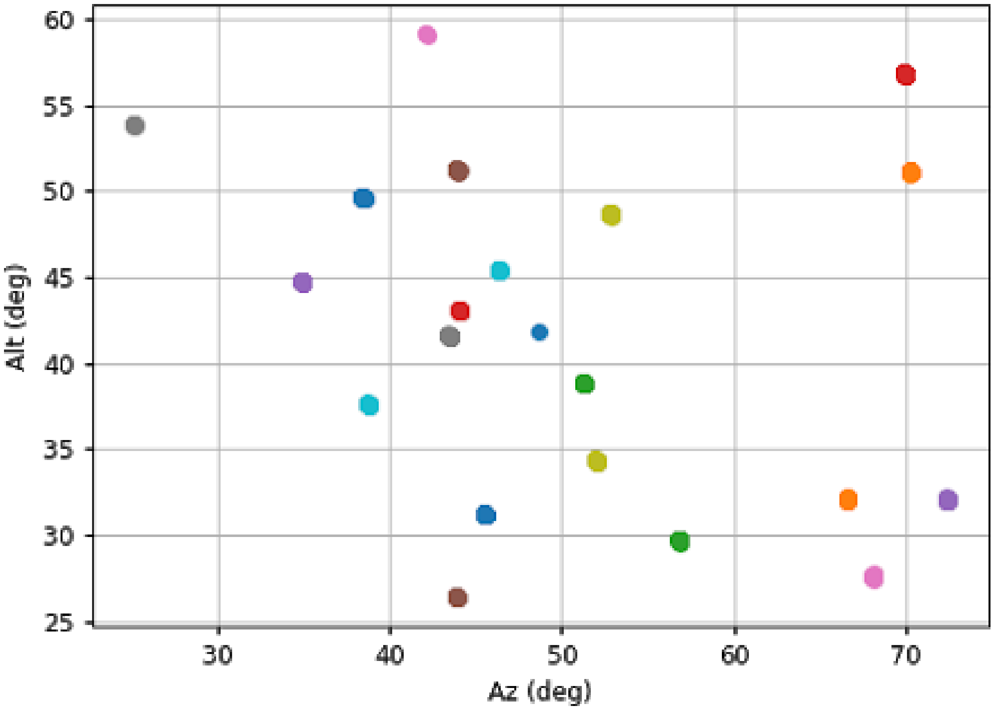

Figure B.5: Identified stars used to track the jitter over several minutes

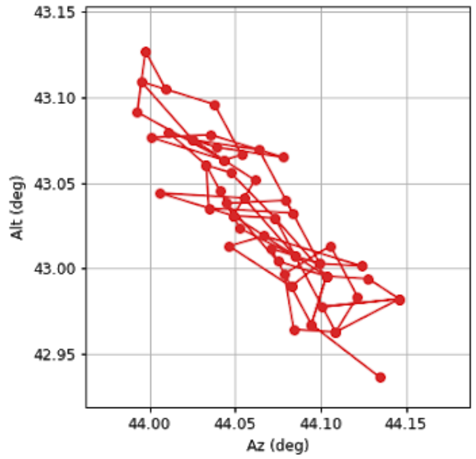

Figure B.6: The trajectory of a blob in azimuth and altitude over 120 seconds.

vary in direction but it also varied in frequency over time. We have not conclusively identified the source of the short timescale jitter.

I investigated this jitter by tracking many individual stars over the course of several minutes. I found stars using the analysis software described in Section 6.2.1. Figure B.5 shows stars identified in an image from one widefield camera. I tracked the movement of each identified star in azimuth and altitude over 120 seconds. The trajectory of one such "blob" has been plotted in Figure B.6.

For each star tracked in the image set, I performed a Lomb-Scargle analysis to find the frequency components in both azimuth and altitude. Panel a and b in Figure B.7 show examples of the results from this analysis. The top window of each panel shows the Lomb-Scargle power in Altitude, while the lower panel shows the Lomb-Scargle power in Azimuth. These analyses tracked 19 and 17 stars respectively. The blue line in each plot shows the mean Lomb-Scargle power versus frequency for the star set, while the black shading around the blue line shows the upper and lower standard deviation.

I ran the analysis described on many time series taken during our flight and I found no discernable pattern to the jitter. The examples in B.7 clearly bear no resemblance to each other, despite using data 24 hours apart with similar sun positions.

I have no reason to believe that our flight train's mechanical attributes changed for any reason

2018-07-10_13:00+120 seconds 19 stars followed

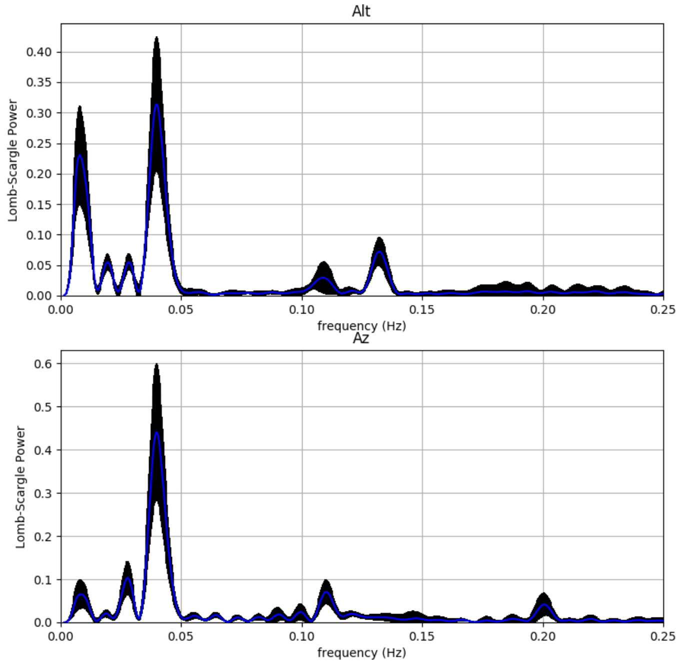

2018-07-11_13:00+120 seconds 17 stars followed

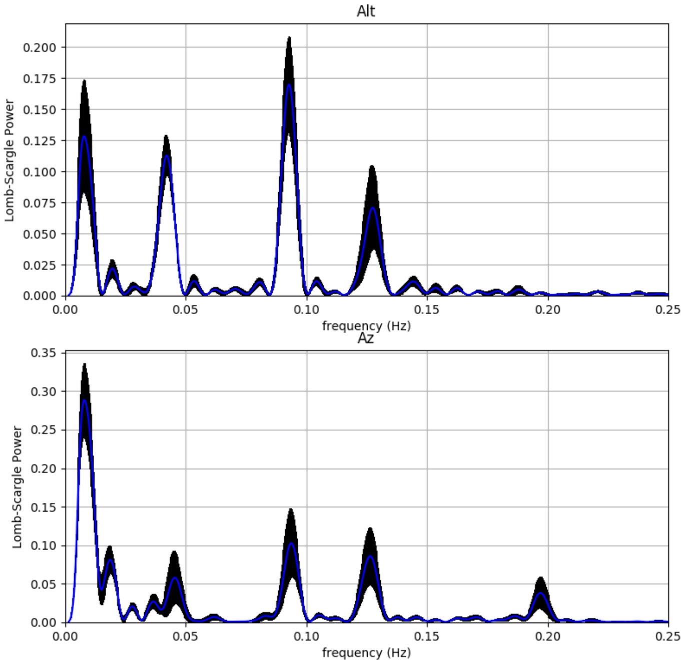

Figure B.7: Examples of Lomb-Scargle jitter analysis other than temperature, and I did not find a relationship between the jitter frequency and temperature. There is atmospheric turbulence at the altitude of the gondola, and we find it plausible that the winds buffeted the gondola around or had a shear between the gondola and balloon. While we find the study of turbulence at the gondola altitude intriguing, and I hoped to use the gondola jitter as an addition sensor of wind conditions at the gondola altitude, we did not design the experiment as a sensor of turbulence at 38 km and I have not found a method to extract any signal from the noise.

The balloon-gondola system resembles a pendulum, but with a flexible arm. Winds drive both the balloon and the gondola, but the incident force is not identical. The balloon has a huge surface area since the diameter is about 100 m, but a low density as it is filled with helium. The balloon is also nearly symmetric, so the direction of the wind does not matter for the driving force. The gondola, on the other hand, is fixed in direction by the rotator, which keeps the solar panels pointed towards the sun, and is much denser than the balloon. The train connecting the balloon and gondola is on the order of 100 m. A wind shear across this distance is plausible. Given this complicated system, I concluded we have little hope of using the gondola movement as a sensor of local turbulence. However, our observations of local turbulence inform the design of subsequent experiments. We plan to include further sensors on future missions to measure turbulence at the gondola altitude. We also will take the gondola jitter into account when calculating the motion blur we expect to encounter.